Current applications using key mineral phases in igneous and metamorphic geology: perspectives for the future

Silvia Volante[1,2,3]*, Eleanore Blereau[4], Martin Guitreau[5], Mahyra Tedeschi[6,7], Valby van Schijndel[8] and Kathryn Cutts[9]

[1]Structural Geology and Tectonics Group, Geological Institute, Department of Earth Sciences, ETH Zürich

[2]Institute of Geology, Mineralogy and Geophysics, Ruhr-Universität Bochum, Universitätsstraße 150, 44801 Bochum, Germany

[3]ISOTOPIA Lab., School of Earth, Atmosphere and Environment, Monash University, Wellington Rd, Clayton, VIC 3800, Australia

[4]Institute of Geophysics and Tectonics, School of Earth and Environment, University of Leeds, Woodhouse, Leeds LS2 9JT, UK

[5]Université Clermont Auvergne, CNRS-UMR 6524, IRD-UMR 163, OPGC, Laboratoire Magmas et Volcans, F-63178 Aubière, France

[6]Programa de Pós-Graduação em Geologia, Universidade Federal de Minais Gerais, Centro de Pesquisas Manoel Teixeira da Costa, Instituto de Geociênciais, Av. Antônio Carlos, 6627, Belo Horizonte 31270-901, Brazil

[7]Institute of Geological Sciences, University of Bern, 3012 Bern, Switzerland

[8]Institute of Geosciences, University of Potsdam, 14476 Potsdam, Germany

[9]Geological Survey of Finland, P.O. Box 96, FI-02151 Espoo, Finland

SV, 0000-0001-8807-4087; EB, 0000-0001-8850-397X
*Correspondence: svolante@ethz.ch/silvia.volante89@gmail.com

Abstract: The study of magmatic and metamorphic processes is challenged by geological complexities like geochemical variations, geochronological uncertainties and the presence/absence of fluids and/or melts. However, by integrating petrographic and microstructural studies with geochronology, geochemistry and phase equilibrium diagram investigations of different key mineral phases, it is possible to reconstruct insightful pressure–temperature–deformation–time histories. Using multiple geochronometers in a rock can provide a detailed temporal account of its evolution, as these geological clocks have different closure temperatures. Given the continuous improvement of existing and new *in situ* analytical techniques, this contribution provides an overview of frequently utilized petrochronometers such as garnet, zircon, titanite, allanite, rutile, monazite/xenotime and apatite, by describing the geological record that each mineral can retain and explaining how to retrieve this information. These key minerals were chosen as they provide reliable age information in a variety of rock types and, when coupled with their trace element (TE) composition, form powerful tools to investigate crustal processes at different scales. This review recommends best applications for each petrochronometer, highlights limitations to be aware of and discusses future perspectives. Finally, this contribution underscores the importance of integrating information retrieved by multi-petrochronometer studies to gain an in-depth understanding of complex thermal and deformation crustal processes.

Unravelling the composite tectono-magmatic and metamorphic evolution of terrains can be challenging because their multistage histories may have erased past information. One way to interrogate and address these complexities is to investigate geological processes throughout Earth's history that are encapsulated in key minerals such as garnet, zircon, titanite, allanite, rutile, monazite/xenotime and apatite. The mineral phases chosen for this contribution are the most used in petrochronological studies as they are reliable chronometers, and their chemical variability has been used to investigate metamorphic and magmatic crustal processes. As petrochronometers, they can retain information about the petrogenesis of their protoliths, (multiple) pressures (P), temperatures (T) and timing (t) at which they (re)crystallized in magmatic, metamorphic and/or hydrothermal events. Investigations employing these minerals

From: van Schijndel, V., Cutts, K., Pereira, I., Guitreau, M., Volante, S. and Tedeschi, M. (eds) 2024. *Minor Minerals, Major Implications: Using Key Mineral Phases to Unravel the Formation and Evolution of Earth's Crust*. Geological Society, London, Special Publications, **537**, 57–121.
First published online May 31, 2023, https://doi.org/10.1144/SP537-2022-254

have provided new breakthroughs in Earth Sciences. Scientific findings through petrochronological investigations include (but are not limited to) the study of the oldest minerals on Earth (Valley *et al.* 2014), the understanding of trace element (TE) partitioning processes between different key mineral phases (e.g. Rubatto 2002) and the study of fluid and magma sources during crust evolution (e.g. Valley 2003; Bouvier *et al.* 2012; Mulder *et al.* 2021). Magmatic and/or metamorphic overprinting stages are heterogeneously recorded by these petrochronometers, which preserve snapshots of a rock evolution. The timing, conditions of formation and distinct closure temperatures (i.e. *Tc* as the temperature of a geochronological system at the time corresponding to its apparent age; Dodson 1973) that characterize minerals and isotope systems (Fig. 1) allow, for example, the U–Pb system in garnet (Mezger *et al.* 1989*a*) to retain information at higher temperatures than in rutile, which resets its internal clock as a function of *T*, grain size and cooling rate. Thus, carrying out multi-mineral studies (Fig. 1) is an incredibly powerful tool to investigate complex magmatic and metamorphic histories (e.g. Cutts *et al.* 2014; Stearns *et al.* 2015; Manzotti *et al.* 2018; Volante *et al.* 2020*c*; Fumes *et al.* 2022; Odlum *et al.* 2022).

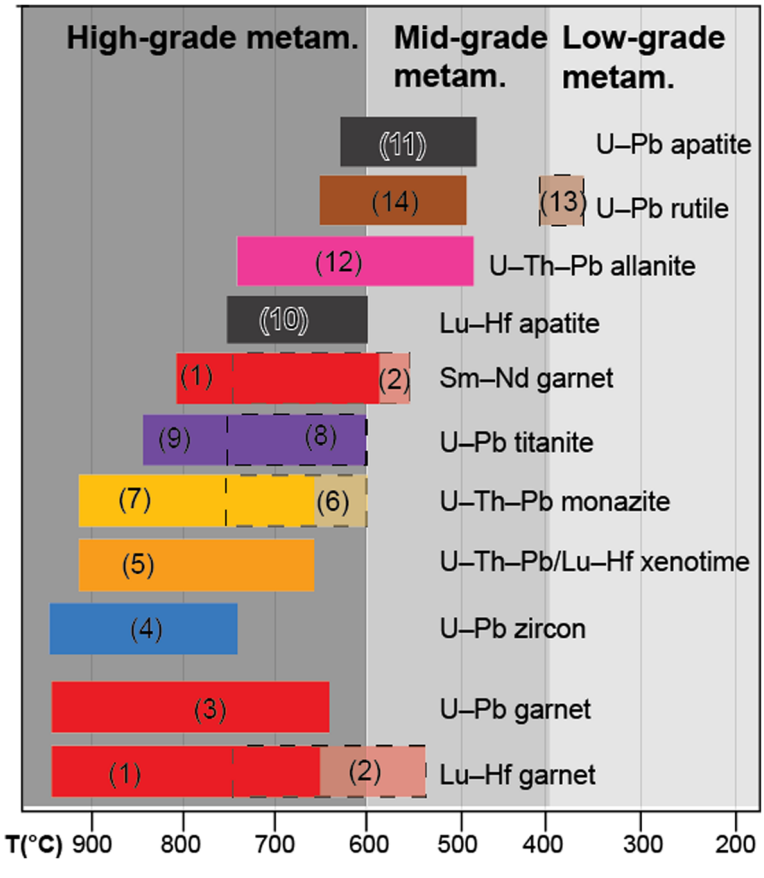

Fig. 1. Closure temperatures (Dodson 1973) for various commonly used geochronometers. References cited in this figure: (1) Smit *et al.* (2010, 2013); (2) Scherer *et al.* (2000); (3) Mezger *et al.* (1989*a*), Li *et al.* (2022); (4) Lee *et al.* (1997), Cherniak and Watson (2001); (5) Cherniak (2006); (6) Copeland *et al.* (1988), Kingsbury *et al.* (1993), Suzuki *et al.* (1994), Smith and Giletti (1997); (7) Spear and Parrish (1996), Vry *et al.* (1996), Braun *et al.* (1998), Kamber *et al.* (1998), Rubatto *et al.* (2001), Asami *et al.* (2002), Schmitz and Bowring (2003), Cherniak *et al.* (2004); (8) Mezger *et al.* (1991), Scott and St-Onge (1995), Cherniak (1995), Frost *et al.*(2001); (9) Schärer *et al.* (1994), Zhang and Schärer (1996), Kohn and Corrie (2011), Spencer *et al.* (2013), Stearns *et al.* (2015), Kohn (2017), Hartnady *et al.* (2019), Kirkland *et al.* (2020); (10) Cherniak (2000*a*), Barfod *et al.* (2005); (11) Cherniak *et al.* (1991), Krogstad and Walker (1994); (12) Oberli *et al.* (2004), Gregory *et al.* (2012); (13) Mezger *et al.* (1989*a*); (14) Cherniak (2000*a*), Vry and Baker (2006), Kooijman *et al.* (2010).

Over the past decades, our ability to interrogate the preserved rock record of crustal metamorphism and magmatism has significantly advanced thanks to continuously improving *in situ* analytical techniques, measurement methodologies and protocols, as well as availability of reference materials that have been calibrated through worldwide inter-laboratory collaborations. Most commonly used instruments include secondary ion mass spectrometry (SIMS) (e.g. Chamberlain *et al.* 2010; Ushikubo *et al.* 2014; Zhou *et al.* 2016; Chaussidon *et al.* 2017) and inductively coupled plasma mass spectrometers (single and multi-collector, sector-field, single and triple quadrupoles) associated with a laser ablation system (LA-ICP-MS, LA-MC-ICP-MS or LA-ICP-MS/MS) either used in tandem (split stream) or separately (e.g. Kylander-Clark *et al.* 2013; Hacker *et al.* 2015; Simpson *et al.* 2021). Additionally, improvements in microanalytical techniques, such as (but not limited to) electron backscatter diffraction (EBSD) mapping (e.g. Cavosie *et al.* 2015), TESCAN integrated mineral analyser (TIMA; e.g. Porter *et al.* 2020), field emission scanning electron microscope (FESEM; Tacchetto *et al.* 2022) for qualitative analysis acquisition and field emission gun (FEG) transmission electron microscope (TEM) for atomic lattice resolution imaging and nanoscale microanalysis (Reddy *et al.* 2020; Tacchetto *et al.* 2021), have significantly contributed in advancing the micro- to nanoscale petrographic, chemical, physical and structural characterization of sample material. The integration of continuously updated thermodynamic modelling studies of monazite (e.g. Janots *et al.* 2007; Kelsey *et al.* 2008; Spear and Pyle 2010; Hoschek 2016), allanite (Spear 2010), zircon (Kelsey *et al.* 2008; Kelsey and Powell 2011; Yakymchuk and Brown 2014) and apatite (Spear and Pyle 2010; Yakymchuk 2017) allows for the construction of a fundamental basis from which to overcome problems related to qualitative interpretations of accessory minerals within the *P–T* space, for which rutile (e.g. Fumes *et al.* 2022; Holtmann *et al.* 2022; Horton *et al.* 2022; Vanardois *et al.* 2022) and titanite (e.g. Kapp *et al.* 2009; Kirkland *et al.* 2016, 2020; Apen *et al.* 2020; Walters *et al.* 2022) already greatly contribute. The above-mentioned analytical advances combined with more traditional petro-structural (micro)analyses (Volante *et al.* 2020*b*) and continuously updated thermodynamic datasets used for modelling pressure (*P*), temperature (*T*) and composition (*X*) are continuously contributing to improve our understanding of crustal processes by allowing a more detailed characterization of mineral phases.

This review aims to showcase snapshots of recent analytical developments such as advancement in understanding the capabilities of LA-ICP-MS/MS and their applications, including new findings in the uptake of water in zircon crystal lattice and its influence on oxygen isotope composition, development and improvement in generating *in situ* quantitative elemental maps that can be directly linked with petrochronological and textural information using key mineral phases in igneous and metamorphic studies. In particular, we focus on the most employed minerals in the literature that can be used not only as chronometers in a great variety of rock lithologies but also as tracers of fluid–rock interactions at crustal conditions, and they include: garnet, zircon, titanite, rutile, allanite, monazite/xenotime and apatite (Fig. 2). In the following section, each mineral is described including its potential as chronometer, thermobarometer and chemical/isotopic tracer applied to crustal magmatic and metamorphic processes. Ultimately, the Discussion section provides examples of applications that use these petrochronometers in magmatic and metamorphic studies with a focus on the complementary set of information obtained when multi-mineral investigations are used to unravel different steps in the evolution of a volume of rock. Future perspectives on the use of these key mineral phases to investigate metamorphic and igneous processes are also included.

Mineral capsules

Garnet

Garnet (Fig. 2a-c; Fig. 3) is a major rock-forming mineral, occurring in metamorphic (felsic and mafic compositions) and felsic peraluminous magmatic rocks (Villaros *et al.* 2009; Bartoli *et al.* 2013; Liu *et al.* 2014; Volante *et al.* 2020*a*; R. Li *et al.* 2021). Garnet is a key metamorphic indicator mineral (Barrow 1893, 1912) and its composition directly relates to the *P–T* conditions it experienced during growth (the garnet stability field extends from greenschist-facies to high-pressure (*HP*) and high-temperature (*HT*) conditions, dependent on rock composition), making it extremely useful as a geothermobarometer. Garnet grains can shield mineral inclusions whose identity or composition can indicate earlier assemblages/conditions experienced by the rock (e.g. St-Onge 1987; Lü *et al.* 2008; Thomas and Davidson 2012; Pourteau *et al.* 2019; Schönig *et al.* 2019; Godet *et al.* 2022). These mineral inclusions can also preserve or trace earlier foliations, which can be used to infer older foliation trends (e.g. Sayab 2006; Aerden *et al.* 2013, 2021; Sayab *et al.* 2015, 2016; Volante *et al.* 2020*b*). Like other porphyroblasts, garnet can also infer kinematics via grain rotation (Fig. 3a; Passchier and Simpson 1986; Johnson 1999). Garnet can record a prolonged history, preserving a growth hiatus, where textural, chemical or chronological evidence shows that garnet grew during more than one

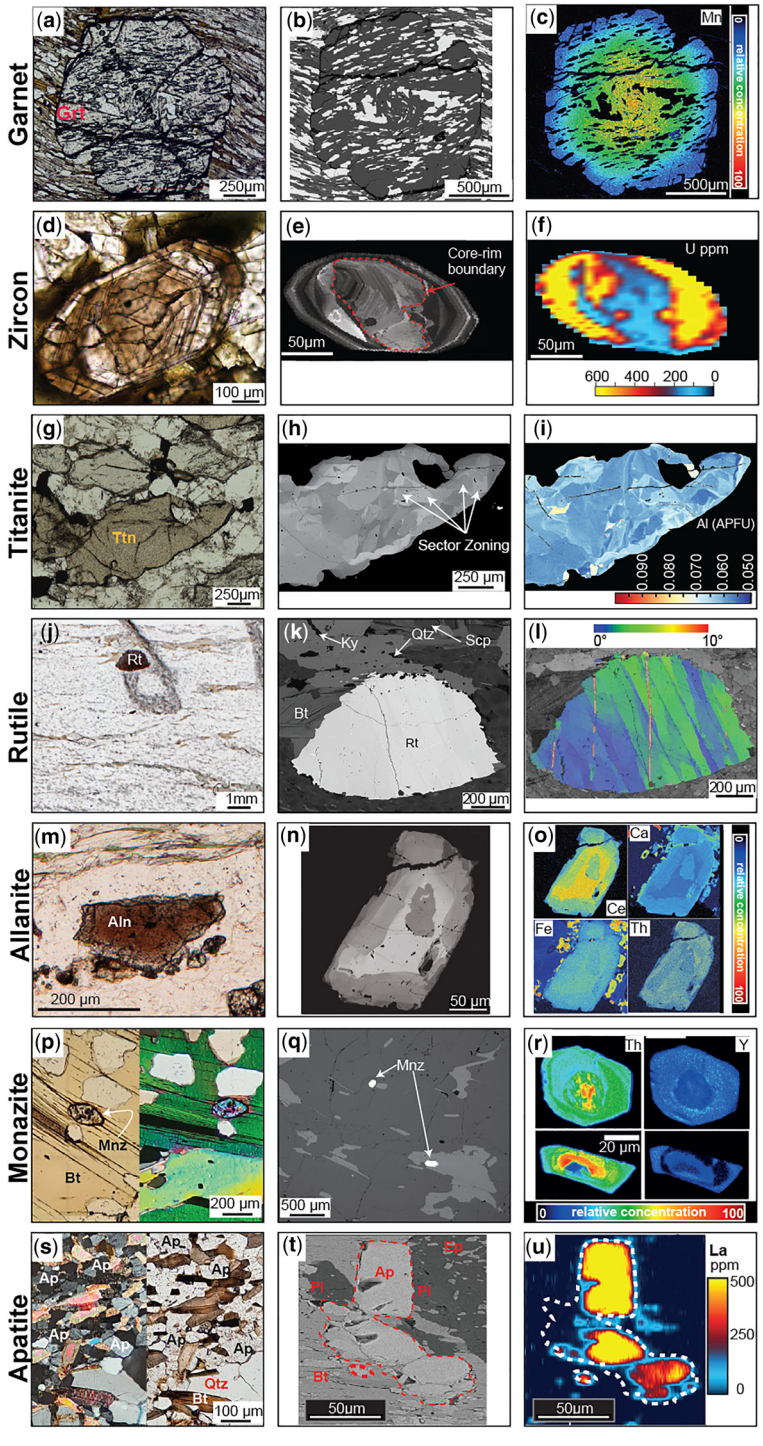

Fig. 2. Representative textures for the key mineral phases described in this contribution. (**a**) Plane polarized light. (**b**) Backscattered electron (BSE) and (**c**) electron microprobe Mn elemental map images showing the early and late stages of fabric development in core and rims, respectively, during garnet growth. (**d**) Plane polarized light,

metamorphic and/or magmatic event (Fig. 3b; e.g. Vance *et al.* 1998; Cutts *et al.* 2010; Ortolano *et al.* 2014; Kulhánek *et al.* 2021; Massonne and Li 2022).

Geochemical tools. Garnet is a powerful tool for linking accessory mineral geochronological and/or isotopic data to the evolution of the major mineral assemblage using trace elements. Linking these two data sources together is the cornerstone of petrochronology (Engi *et al.* 2017). Trace elements such as rare earth elements (REE) partition strongly into garnet (Bea *et al.* 1994; Hermann and Rubatto 2014), particularly the middle to heavy rare earth elements (M-HREE; Fig. 3c). Other minerals that also readily accommodate M-HREE, such as zircon and monazite, compete with garnet, resulting in modified trace element patterns when the accessory phase grows in the presence or absence of garnet. The use and effectiveness of these trace element partitioning relationships (D_{REE}) were first presented for zircon and garnet (Fig. 3d; Rubatto 2002). Zircon grown in the presence of garnet has a M-HREE slope of *c.* 1 effectively flat, and a slightly curved to near flat D_{REE} pattern (Whitehouse and Platt 2003; Hokada and Harley 2004; Kelly and Harley 2005; Harley and Kelly 2007; Wu *et al.* 2008*a*, *b*; Fornelli *et al.* 2014, 2018). Since these first studies, trace element partitioning has grown into a widely used tool in petrochronology (Whitehouse and Platt 2003; Hokada and Harley 2004; Baldwin and Brown 2008; Clark *et al.* 2009; Harley and Nandakumar 2014), and some studies conducted quantitative partitioning experiments to constrain temperature dependent patterns for D_{REE} (Zrc/Grt) (Rubatto and Hermann 2007; Taylor *et al.* 2015), building upon empirical studies (Rubatto 2002; Hermann and Rubatto 2003; Whitehouse and Platt 2003; Hokada and Harley 2004; Kelly and Harley 2005; Buick *et al.* 2006). To address the challenge of handling extensive datasets generated by LA-ICP-MS, Taylor *et al.* (2017) developed an array plot for trace element partitioning data that can also show additional trends compared to the standard D_{REE} plot (Fig. 3e). D_{REE} (Mnz/Grt) is also a useful partitioning system (see Monazite section for more details). Trace element mapping of garnet via LA-ICP-MS is an area that is currently undergoing significant advances (e.g. Chew *et al.* 2017, 2021; Raimondo *et al.* 2017; Rubatto *et al.* 2020). M-HREE, Y and Cr zoning in garnet provides additional information about the growth history and mineral relationships not apparent in major element zonation (Raimondo *et al.* 2017).

Geochronology. Since the late 1980s, U–Pb and Sm–Nd geochronology (Mearns 1986; Mezger *et al.* 1989*b*) used multiple mineral phases to determine the age of whole-rock. The application of these methods led to the discovery of a favourable spread in Sm–Nd ratios between garnet and whole rock (Humphries and Cliff 1982). U–Pb garnet dating was found to be affected by U-rich inclusions such as zircon, monazite and apatite. Thus, for the following 30 years, garnet geochronology has been conducted using Sm–Nd and, subsequently, once instrumentation advanced sufficiently to measure low Hf contents in garnet, the Lu–Hf system was used for garnet dating (Duchêne *et al.* 1997). Inclusions such as monazite and apatite for the Sm–Nd system were treated with a HCl leaching step method that would remove significant monazite Nd components (Scherer *et al.* 2000), whereas Lu–Hf garnet geochronology is greatly affected by inclusions such as zircon, with samples containing significant contents of zircon being avoided for garnet whole-rock dating (Scherer *et al.* 2000). The following studies have compared the two isotopic systems for garnet dating via dissolution (Vervoort 2013), and they have shown that the Lu–Hf system (*Tc c.* 650–900°C) has slightly higher *Tc* than Sm–Nd (*Tc c.* 600–800°C) (Fig. 1; Scherer *et al.* 2000; Smit *et al.* 2013; Johnson *et al.* 2018). Traditionally, both Sm–Nd and Lu–Hf systems via isotope dilution–thermal ionization mass spectrometry (ID-TIMS) or MC-ICP-MS dissolution methods require the separation and purification of garnet prior to dissolution, column separation and measurement that is commonly associated with loss of the textural context of the analysed grains (cf. Pollington and Baxter 2010). Prolonged (e.g. Baxter and Scherer 2013; Bollen *et al.* 2022) or incremental garnet growth makes a single age from garnet separate, potentially geologically meaningless (e.g. Pollington and Baxter 2010). To overcome these issues, garnet has often been separated based on colour (e.g. Vance *et al.* 1998) or by using a microdrill to target garnet growth rings in order to determine the growth rate of garnet crystals (Fig. 3f; see Pollington and Baxter

Fig. 2. *Continued.* (**e**) cathodoluminescence (CL) and (**f**) laser ablation ICP–MS U (ppm) elemental map images of zircon. (**g**) Plane polarized light, (**h**) BSE and (**i**) quantitative map of Al (a.p.f.u., atom per formula unit) images of titanite. (**j**) Plane polarized light, (**k**) BSE and (**l**) EBSD map images for rutile. (**m**) Plane and crossed polarized light, (**n**) BSE and (**o**) electron microprobe Th and Y elemental map images of monazite. (**p**) Plane and crossed polarized, (**q**) BSE and (**r**) LA–ICP–MS trace element map images of apatite. (**s**) Plane polarized light, (**t**) BSE and (**u**) X-ray elemental map images of allanite. Source: (c) Volante *et al.* (2020*c*); (f) Chew *et al.* (2017); (i) Walters *et al.* (2022); (l) Moore *et al.* (2020*a*, *b*); (n) Barrote *et al.* (2022*a*); (o) Volante *et al.* (2020*c*); (r) Henrichs *et al.* (2019); (u) Corti *et al.* (2020).

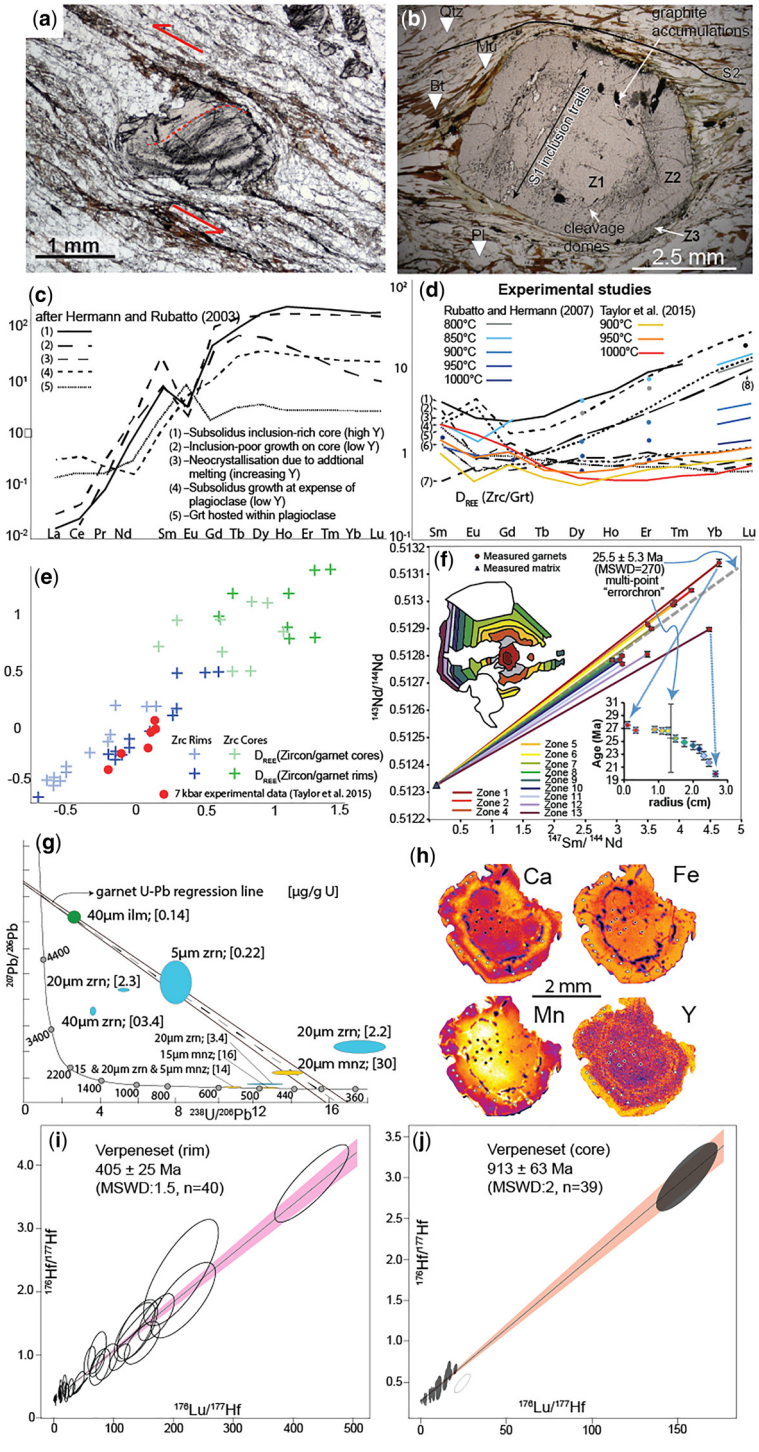

Fig. 3. (**a**) Garnet porphyroblast indicating the kinematics of deformation (arrows) as a sigma-clast and exhibiting inclusion trails of an internal foliation. (**b**) Polymetamorphic garnet grain from Polnish, Scotland (see Vance *et al.* 1998; Cutts *et al.* 2009). The core (Z1) and first rim (Z2) zones preserve the same early foliation (S1) but have

2010, 2011; Dragovic *et al.* 2012, 2015; Schmidt *et al.* 2015; Tual *et al.* 2022). Results of such studies have showcased how effectively garnet can be used for geochronology, the caveat being that these methods are expensive, time consuming (*c.* 2 months) and the presence of inclusions must be considered and evaluated.

The recent introduction of ICP-MS/MS, which eliminates isotopic interferences for Lu–Hf measurements (i.e. ^{176}Lu and ^{176}Yb on ^{176}Hf), coupled with an increase in machine sensitivity allowing to measure elements at very low concentrations (i.e. part per billion, ppb), has permitted significant advances in garnet geochronology. These analytical advances not only are at the foundation of the development of *in situ* Lu–Hf measurements in garnet (see Simpson *et al.* 2021; Brown *et al.* 2022; Ribeiro *et al.* 2022; Tamblyn *et al.* 2022; Simpson *et al.* 2023), but also resulted in revisiting of the U–Pb system in garnet with *in situ* analyses now possible using LA-ICP-MS or -SC (single collector) -MS (Seman *et al.* 2017; Gevedon *et al.* 2018; Millonig *et al.* 2020). Since garnet commonly has low U contents, the presence of U-rich inclusions remains an issue for *in situ* methods. Nonetheless, Uranium content in garnet can easily be tested via LA-ICP-MS spot analysis prior to U–Pb analysis and coupled with detailed textural imaging to identify potential U-rich inclusions. Grossular and andradite garnet tend to have enough U (>1 part per million, ppm), and many studies have used this method as a means of dating skarns related to mineralization (Seman *et al.* 2017; Gevedon *et al.* 2018; Wafforn *et al.* 2018; Duan *et al.* 2020). More recently, other works have also found almandine-pyrope-rich garnet with lower but enough U (>0.02 ppm) to produce reliable metamorphic ages (Millonig *et al.* 2020; Cerva-Alves *et al.* 2021; Schannor *et al.* 2021; O'Sullivan *et al.* 2023). Nonetheless, U-rich inclusions such as monazite, apatite and zircon shift data points on a Tera–Wasserburg (TW) diagram to the left, right or along the regression, reflecting older, younger or the same age as garnet, respectively (Fig. 3g; Millonig *et al.* 2020). Besides textural observations, to screen and filter out inclusion-dominated analyses it is crucial to monitor the masses on the ICP-MS such as Y and Zr for zircon, or light rare element (LREE) for monazite and allanite. The *in situ* U–Pb garnet dating method (*Tc c.* 650–900°C) has the advantage of minimal sample preparation, rapid analysis (2 hours) and the possibility of monitoring the signal. The Lu–Hf method is limited to garnet that contains sufficient Lu for measurement and relatively inclusion free, with zircon inclusions significantly affecting the age results (Simpson *et al.* 2021). This method has larger uncertainties than solution-based Lu–Hf analysis, but numerous advantages. Low Lu or high Hf (i.e. zircon) inclusions can be targeted to produce an isochron from a single garnet grain. The ablated spots (*c.* 40–120 μm) can target different chemical domains, including separate core and rim isochron ages (Fig. 3h–j; Tamblyn *et al.* 2022). The ability to produce an isochron from a single garnet grain means that this method can also be used to investigate detrital garnet (see Pereira *et al.* this volume, in press). An alternative to directly date garnet is targeting datable primary mineral inclusions such as monazite (e.g. Mahan *et al.* 2006; Cutts *et al.* 2010; Williams *et al.* 2017). However, possible preservation of detrital or older inclusions must be evaluated (Martin *et al.* 2007; Cutts *et al.* 2009, 2013; Peixoto *et al.* 2018).

Isotope geochemistry. Oxygen isotopes have been applied to whole-rock and mineral samples to trace the sources of metamorphic/metasomatic (e.g. Chamberlain and Conrad 1991; Crowe *et al.* 2001; Page *et al.* 2010; Martin *et al.* 2011, 2014; Vho *et al.* 2020) and magmatic/mantle fluids (e.g. King and Valley 2001; Lackey *et al.* 2006; Harris and Vogeli 2010). Initially, oxygen isotopes were applied to garnet to determine pressure estimates, based on the temperature dependent fractionation

Fig. 3. *Continued.* cleavage domes and graphite inclusions on their border. A thin, inclusion-rich rim (Z3) which has been poorly preserved is observed. (**c**) Representative chondrite-normalized REE patterns for different types of garnet (Blereau 2017). (**d**) Partitioning between zircon and garnet: (1) Buick *et al.* (2006); (2) Hokada and Harley (2004); (3) GL7 in Rubatto (2002); (4) GP7 in Rubatto (2002); (5) Harley *et al.* (2001); (6) Kelly and Harley (2005); (7) Whitehouse and Platt (2003); (8) Hermann and Rubatto (2003). (**e**) Partitioning array plot of zircon/garnet compared to the experimental data of Taylor *et al.* (2015). The axes of this plot are: x, $\log(D_{Yb})$; y, $\log(D_{slope}) = \log(D_{Yb/DGd})$ (Blereau 2017). (**f**) Sm–Nd dating of a large garnet porphyroblast by Pollington and Baxter (2010). The various garnet rims were obtained using a microdrill (the drill lines are marked in black on the garnet). Coloured zones correspond to the coloured isochrons and age points in the plots indicate that garnet grew over *c.* 8 myr, from 28 to 20 Ma. (**g**) TW diagram showing how the grain size and the amount of ablated U-rich inclusions affect garnet U–Pb dating. (**h**) Garnet compositional map of Ca, Fe, Mn and Y (from top left) of sample Verpeneset from Tamblyn *et al.* (2022). Black and white dots represent the position of core and rim analyses, respectively. (**i** and **j**) Lu/Hf isochrons obtained from garnet (i) core and (j) rim. Uncertainties consider overdispersion of the data and isochron ages are calculated with age offset (see Tamblyn *et al.* 2022 for full details). Source: (a) Photo courtesy of J. Pownall; (c–d) modified after Blereau (2017); (f) adapted from Pollington and Baxter (2010), Baxter *et al.* (2017); (g) modified after Millonig *et al.* (2020).

between co-existing mineral pairs (experimentally or empirically determined; Baxter *et al.* 2017 and references therein). This method utilizes slow diffusion of oxygen within garnet, thus peak temperature isotope fractionation is retained (Kohn and Valley 1998; Baxter *et al.* 2017). Improvements in analytical methods (analysis via SIMS) allowed for *in situ* analysis of oxygen isotopes in garnet to track the origin of metamorphic/metasomatic fluids (e.g. Raimondo *et al.* 2012, 2017; Russell *et al.* 2013). For example, garnet can preserve variation of fluid compositions as it grows, particularly in eclogites or skarns (D'Errico *et al.* 2012; Rubatto and Angiboust 2015). Oxygen in garnet is very similar to the bulk rock $\delta^{18}O$ value, but deviations can occur following temperature variations affecting equilibration factors between minerals (i.e. garnet–quartz), changes in modal proportions and mineral assemblage during metamorphism as well as the presence of externally sourced fluids. Nonetheless, experimentally determined oxygen diffusion rates in garnet show that original isotope compositions can be retained despite partial re-equilibration of major elements (Scicchitano *et al.* 2021). Other stable isotopes such as Fe or Li may be applied in garnet (Bebout *et al.* 2014, 2022; An *et al.* 2017; Gerrits *et al.* 2019; Penniston-Dorland *et al.* 2020; Hoover *et al.* 2021, 2022), with limitations of these largely depending on analytical ability.

Thermobarometry. Geothermometry in garnet (Ferry and Spear 1978; Baxter *et al.* 2017) was initially applied via Fe–Mg exchange between garnet and biotite (Ferry and Spear 1978; Perchuk and Lavrent'Eva 1983; Ganguly and Saxena 1984) and geobarometry via the 'GASP' (garnet–aluminosilicate–silicate–plagioclase) end-member reaction, which is pressure sensitive due to the large molar volume difference between reactants and products (e.g. Ghent 1976; Newton and Haselton 1981; Holdaway 2001; Caddick and Thompson 2008). Later, large thermodynamic datasets (e.g. Berman 1988; Holland and Powell 1990, 1998, 2011) allowed for *P–T* pseudosection calculation, which was combined with the use of garnet end-member compositions to constrain the growth path or max *P* and *T* conditions (e.g. Spear *et al.* 1984; Vance and Mahar 1998). A caveat in the use of this method is the isolation of grown garnet (i.e. core domain) from the whole-rock composition used for *P–T* pseudosection calculation (e.g. Marmo *et al.* 2002; Evans 2004; Tinkham and Ghent 2005; Cutts *et al.* 2009, 2010). This approach is particularly useful where garnet growth domains are the result of different orogenic events (e.g. Cutts *et al.* 2014). Software for modelling evolving bulk compositions during garnet growth along a *P–T* path was developed to produce more reliable *P–T* estimates (Theria_G, Gaidies *et al.* 2008; GRTMod, Lanari *et al.* 2017). For *P–T* modelling, garnet compositions (i) may record prograde growth, which is typically defined by bell-shaped Mn enrichment in the garnet core (e.g. Hollister 1966; Atherton 1968; Cygan and Lasaga 1985; Schwandt *et al.* 1996; Dziggel *et al.* 2009; Lanari and Engi 2017; Spear 2017; Dempster *et al.* 2020), or (ii) alternatively, at high temperatures, garnet chemistry may be used to determine the max *T* conditions experienced by the sample where the prograde growth major element zonation is partially or completely re-equilibrated (Caddick *et al.* 2010). Also, fluid and/or melt inclusions hosted in peritectic garnet from migmatites have been used to evaluate the starting composition of the anatectic melt and fluid regime during anatexis (e.g. Cesare *et al.* 2009, 2011; Ferrero *et al.* 2012, 2021; Carvalho *et al.* 2019; Borghini *et al.* 2020). Inclusions such as zircon and quartz in garnet can also be used to produce pressure estimates using Raman barometry (Zhong *et al.* 2019; Spear and Wolfe 2020). After being trapped in a host mineral during part of the cooling and exhumation history of a rock, inclusions may develop residual pressures due to the differences in thermal expansivity and compressibility between the host and the inclusions (Gonzalez *et al.* 2019; Zhong *et al.* 2019, 2020). Within both metamorphic and magmatic studies, however, garnet-based thermobarometry should always be applied with a thorough petrological and microstructural relationships characterization and an appropriate estimate of equilibrium volume of the rock sample. Results that are inconsistent with the observed mineral assemblage should be crosschecked with other comparable tools and should be interpreted with care. Additionally, taking a step back and carefully reanalysing field and textural context of the investigated rocks, as well as reassessing the documentation of sample preparation, analytical procedure and data processing, may also reveal missed information.

Zircon

The mineral zircon ($ZrSiO_4$) has traditionally been the most robust accessory phase and widely used geochronological and geochemical tool in petrochronology to investigate crustal formation and evolution, and to untangle complex rock histories that most minerals fail to retain (e.g. Froude *et al.* 1983; Scherer *et al.* 2007; Guitreau *et al.* 2019). For instance, in the Archean Lewisian Gneiss Complex, NW Scotland, zircon is the only accessory mineral that has recorded the several Archean magmatic phases (cores) and the multiple ultra-high temperature (UHT) to HT/medium (M)T overprinting events (rims) (e.g. Whitehouse and Kemp 2010; Taylor *et al.* 2020; Fischer *et al.* 2021), whereas others such as monazite and titanite record only parts of the metamorphic events (e.g. Zhu and O'Nions

1999; Goodenough *et al.* 2013). Its resistance to erosive processes makes zircon a prime choice when studying detrital crystals to unravel past formation of continental crust in deeply eroded areas, or simply ancient terranes (e.g. Iizuka *et al.* 2005; Dhuime *et al.* 2012; Næraa *et al.* 2012; Nordsvan *et al.* 2018; Gardiner *et al.* 2019; Kirkland *et al.* 2021; Tedeschi *et al.* 2023; Pereira *et al.* this volume, in press). Over the years, many techniques have been improved to study zircon and retrieve various types of information from it (Table 1).

When zircon crystallizes, it can develop various textures depending on the conditions at which it forms, such as sharp concentric growth zoning and/or marginal resorption if zircon grew in a magmatic environment or more irregular domains of homogeneous zoning cutting discordantly the growth domains in the post-magmatic environment (e.g. Corfu *et al.* 2003 and references therein). These textures are commonly revealed by routine imaging of cathodoluminescence (CL) or backscattered electrons (BSE) using a scanning electron microscope (SEM). Cathodoluminescence response is mostly due to interaction between the primary electron-beam and zircon lattice through a complex energy transfer reaction that ends with the emission of photons by tetravalent REE, especially Dy (e.g. Nasdala *et al.* 2003). Visible textures range from broad to fine oscillatory zoning in igneous zircon (Fig. 2d–f; Fig. 4a, b) to large homogeneous to patchy domains in metamorphic conditions (e.g. Corfu *et al.* 2003). Raman spectroscopy can be used to quantitatively map radiation damage zoning in single zircon crystals (i.e. metamictization; Balan *et al.* 2001) and, hence, evaluate the effects of radiation damage on the final U/Pb ratio (Anderson *et al.* 2020) or on any elemental and/or isotopic signature. Igneous zircon most commonly form when the

Table 1. *Synoptic table of most used tools for zircon investigations*

Tool*	Interest	Example of reference
Morphology	Nature of parental magma (alkaline, peraluminous or calc-alkaline)	Pupin (1980); Vavra (1993)
CL and BSE images	Pristineness of crystal lattice and crystallization conditions (igneous, metamorphic or weathered)	Vavra (1990); Hanchar and Miller (1993); Corfu *et al.* (2003); Guitreau *et al.* (2018)
Inclusions (mineral and melt)	Nature of parental magma and/or fluids (for primary inclusions either as melt or mineral)	Thomas *et al.* (2003); Hopkins *et al.* (2008); Bell *et al.* (2015)
EBSD	Orientation and deformation of crystals	Tolometti *et al.* (2022); Cox *et al.* (2022)
Trace element concentrations	Nature of parental magma, magmatic or metamorphic origin and pristineness	Grimes *et al.* (2007, 2015); Laurent *et al.* (2021); Guitreau *et al.* (2022)
(Ti)	Crystallization temperature	Watson *et al.* (2006); Fu *et al.* (2008)
(K) and (Ca)	Primitive v. altered zircon	Bouvier *et al.* (2012); McCubbin *et al.* (2016)
Th/U	Zircon crystallization conditions (e.g. magmatic v. metamorphic origin) and weathering	Vavra *et al.* (1999); Kirkland *et al.* (2015); Yakymchuk *et al.* (2018); Guitreau and Flahaut (2019)
Ce anomaly	Redox state of parental magma	Smythe and Brenan (2016); Trail *et al.* (2012)
U–Pb	Dating (absolute age determination)	Wetherill (1956, 1963); Davis *et al.* (2003 and reference therein); Schoene (2014)
Lu–Hf	Source tracing (e.g. mantle or crust)	Patchett (1983); Amelin *et al.* (2000); Gerdes and Zeh (2009); Guitreau *et al.* (2012)
O	Source tracing (e.g. involvement of clay-rich sediments)	Valley (2003); Iizuka *et al.* (2013)
Si isotopes	Source tracing, parental magma SiO_2 content and crystallization history	Trail *et al.* (2018); Guitreau *et al.* (2020, 2022)
Zr isotopes	Magma crystallization history	Ibañez-Mejia and Tissot (2019); Guo *et al.* (2020); Tompkins *et al.* (2020)

*BSE, Backscattered electron; CL, cathodoluminescence; EBSD, electron backscatter diffraction.

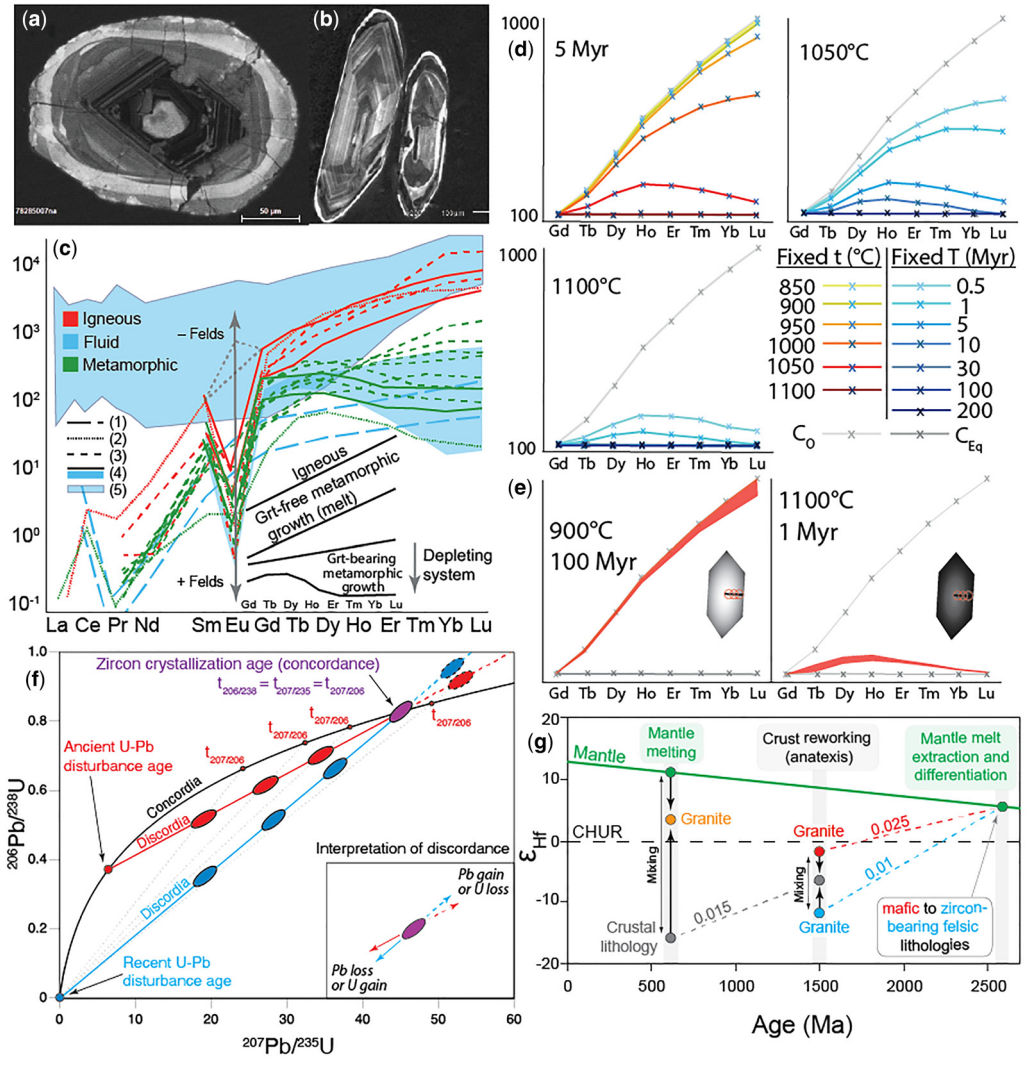

Fig. 4. (**a**) Cathodoluminescence image of a complexly zoned zircon crystal from the Napier Complex (Antarctica) showing a (recrystallized) bright metamorphic core surrounded by a fine-oscillatory zoned magmatic domain, itself resorbed and overgrown by three distinct metamorphic overgrowths. (**b**) Igneous zircon crystals exhibiting fine-oscillatory zoning from core to rim except for a thin metamorphic outer overgrowth. (**c**) Representative chondrite normalized REE patterns for different types of zircon. (1) Rubatto and Hermann (2007); (2) Hoskin and Schaltegger (2003); (3) Rubatto *et al.* (2013); (4) Taylor *et al.* (2014); (5) Li *et al.* (2018). (**d**) Modelled diffusion modified M-HREE compositions expected from *c.* 20 µm diameter SHRIMP spot analysis on the edge of a modelled theoretical zircon. C_0, original unmodified composition; C_{Eq}, equilibrated composition. (**e**) M-HREE spread generated by incomplete modification of a modelled zircon after different *T*–*t* conditions. (**f**) Concordia diagram illustrating the interpretation of zircon U–Pb data in terms of ages depending on whether the U–Pb system evolved in a closed or open system, and when disturbance occurred. (**g**) Graphical representation of Lu–Hf isotope evolution of distinct geological reservoirs. This graph provides a theoretical framework for the interpretation of zircon Hf isotope signatures. Source: (d) and (e) after Blereau *et al.* (2022).

activity of ZrO_2 and SiO_2 is optimal. This is the case in most magmas with SiO_2 concentrations over 57 wt%, although rare crystals in magmas with lower SiO_2 concentrations do exist (e.g. Aranovich *et al.* 2017; Fischer *et al.* 2021; Bea *et al.* 2022). Zircon precipitation from melts was investigated early on by Watson (1979) and Watson and Harrison (1984), and revisited by Boehnke *et al.* (2013).

The nature of mineral inclusions can provide a first order evidence of phases that co-precipitated with zircon and, thus, give information about the nature/composition of the melt in which it crystallized and the pressure and temperature conditions at which it grew (Delavault *et al.* 2016; Emo *et al.* 2018; Antoine *et al.* 2020). The same can be done with melt inclusions, but these can also be used to estimate partition coefficients for trace elements if they represent bulk-melt composition and their chemistry remained unmodified since entrapment (Thomas *et al.* 2003; Gudelius *et al.* 2020).

Geochemical tools. Zircon incorporates large quantities of trace elements from ppm to thousands of ppm level (e.g. Belousova *et al.* 2001; Hoskin and Schaltegger 2003), making it an easy target for analysis using electron microprobe (EPMA), ICP-MS, LA-(MC-)ICP-MS (Košler *et al.* 2005; Chew *et al.* 2017; Petrus *et al.* 2017) and secondary ionization mass spectrometers or sensitive high-resolution ion microprobe (SIMS/SHRIMP). The rapid technological improvements using LA-(MC-)ICP-MS allow now the acquisition and extraction of quantitative data from a mapped area, including chemical and isotopic information of accessory phases such as zircon (Petrus *et al.* 2017; Chew *et al.* 2021). Experiments and natural observations indicate very slow diffusion for most elements within the zircon lattice (see Lee *et al.* 1997; Cherniak and Watson 2003 for values). Pristine igneous zircon elemental variability is usually relatively small, making this mineral a poorly sensitive tracer of melt composition, except for sharp variations (i.e. strongly alkaline, felsic and mafic; e.g. Belousova *et al.* 2002; Grimes *et al.* 2007; Guitreau *et al.* 2022). However, when zircon undergoes significant radiation damage, it can be sensitive to thermal events that result in incorporation of measurable quantities of light REEs (e.g. Hoskin and Schaltegger 2003; Bouvier *et al.* 2012; Pidgeon *et al.* 2017). This modification of zircon composition is a good proxy for secondary alteration and/or weathering. Along the same line, non-formula elements, such as Ca, K and Al, can enter zircon easily once it becomes porous due to significant radiation damage accumulation (e.g. Holland and Gottfried 1955; Ewing *et al.* 2003; McCubbin *et al.* 2016; Pidgeon *et al.* 2019). Monitoring LREEs and non-formula elements allows for filtering of pristine zircon crystals or domains from altered and weathered ones. In contrast, rare earth element patterns in metamorphic zircon are more useful because equilibrium with other phases has a forcing effect on partition coefficients such that zircon cannot incorporate as much HREE as it would normally do (Fig. 4c). This is well illustrated when zircon forms in equilibrium with garnet (e.g. Kelly and Harley 2005; Blereau 2017), resulting in flattened to steepened heavy REE patterns (Fig. 4c). Whilst extremely sluggish under most conditions of metamorphism (Cherniak and Watson 2003), under extreme metamorphic conditions (>1000°C), the REE content in zircon may also be modified as a function of temperature and time (Watson 1996; Blereau *et al.* 2022), although others have suggested decoupling of REE from U–Pb above 850°C (Kunz *et al.* 2018; Jiao *et al.* 2020*b*; Durgalakshmi *et al.* 2021). REEs within zircon are impurities that are expelled at high-T resulting in the removal of internal zoning (Hoskin and Black 2000), with garnet acting as a sink for the released REEs (see Discussion). Diffusional modelling of REE-in-zircon shows that an initially igneous zircon (i.e. an inherited grain with steep M-HREE patterns) within a garnet-bearing metapelite is in disequilibrium with the garnet, and when exposed to metamorphic temperatures, the zircon attempts to reach equilibrium with garnet (i.e. a *c.* 1:1 D_{REE} pattern) (Blereau *et al.* 2022; Fig. 4d). Zircon with a 50 μm radius can be re-equilibrated with the host metamorphic assemblage during both short (1100°C for 1–5 Ma) and extended periods (1050°C for 10–30 Ma or 1000°C for 200 Ma) of UHT metamorphism (Blereau *et al.* 2022; Fig. 4e). Conversely, unless diffusion is enhanced by fluids or other processes, below 900°C, zircon will largely preserve its pre-metamorphic REE signature, even when metamorphism is prolonged (>100 Ma) (Blereau *et al.* 2022; Fig. 4e). The change of valence of Ce and Eu to 4+ and 2+, respectively, in igneous zircon can be used to estimate redox conditions through Ce and Eu anomalies (e.g. Trail *et al.* 2012; Smythe and Brenan 2016; W.T. Li *et al.* 2021). However, some authors suggest using these proxies with caution because of melt cooling and chemical evolution (e.g. Loader *et al.* 2022). Europium anomalies can also be used to track feldspar fractionation and to estimate whether zircon crystallized in equilibrium with feldspar in igneous and metamorphic zircon, respectively (Rubatto 2002).

The ratio of Th over U is often used in zircon because it provides information about co-precipitating phases (e.g. Kunz *et al.* 2018). It can help discriminate igneous (Th/U *c.* 0.2–0.8) from metamorphic (Th/U < 0.1 or >1) zircon domains/crystals, distinguish between zircon formed under amphibolite-facies and granulite-facies and can trace low-temperature weathering of radiation-damaged zircon (e.g. Vavra *et al.* 1999; Hoskin and Black 2000; Kirkland *et al.* 2015; Yakymchuk *et al.* 2018; Guitreau *et al.* 2019; Guitreau and Flahaut 2019; Barrote *et al.* 2020). However, Th/U in zircon is not always a faithful recorder of metamorphic processes (Möller *et al.* 2003; Harley and Kelly 2007), and it should be used with caution on a case-by-case basis. Typically, U–Pb LA-ICP-MS

geochronology routines do not include appropriate internal standard elements, therefore, the U, Th and Pb concentrations are semi-quantitative only.

Geochronology. Zircon is most commonly dated using the U–Pb isotope system (e.g. Schoene 2014) as, for this systematics, it has several advantages compared to other minerals. Zircon U–Pb isotope measurements are done using a great variety of techniques from solution-based such as TIMS for the most precise ages and MC-ICP-MS/ICP-MS to *in situ* microbeam techniques (i.e. SIMS, SHRIMP, LA-ICP-MS, LA-MC-ICP-MS). One of the main advantages is that Pb is essentially excluded from the zircon lattice because of its size and valence, resulting in virtually all measurable Pb in zircon being radiogenic – produced by the radioactive decay of U and Th isotopes. This means that the parent/daughter ratio measured in pristine zircon combined with U decay constants can be directly converted into an age (Schoene 2014). However, zircon lattice can become damaged by radioactive decay over time, which results in metamictization. This process makes zircon porous to external agents that may incorporate Pb, and other non-formula elements, into the crystal lattice, thus compromising the determined age. Another major benefit of the U–Pb isotope system compared to others is the fact that it contains two isotope systems (i.e. ^{238}U–^{206}Pb and ^{235}U–^{207}Pb) with distinct decay constants (e.g. Le Roux and Glendenin 1963; Jaffey *et al.* 1971), allowing open- v. closed-system evolution to be assessed. For easy visualization, U–Pb data are commonly plotted in ^{238}U–^{206}Pb and ^{235}U–^{207}Pb Wetherill concordia diagram (Fig. 4f; Wetherill 1956). When both dates lie on the concordia curve, the date is called concordant and is geologically meaningful since it likely reflects a closed U–Pb system evolution. By contrast, when both dates are different, the measured date is discordant and evaluation on the geological meaning will vary case by case. A third date can also be derived directly from the $^{207}Pb/^{206}Pb$ ratio that inherently assumes closed-system evolution. This date is the oldest of the three in the case of 'normally' discordant data (i.e. datapoint is located below the concordia curve). Unless information regarding the validity of intercepts in concordia diagram is available (e.g. multiple analyses from the same crystal or growth zones), $^{207}Pb/^{206}Pb$ ages are commonly more precise for zircons >1.5 Ga, whereas ^{238}U–^{206}Pb ages are used for crystals <1.5 Ga (Spencer *et al.* 2016).

Depending on when the U–Pb isotope system disturbance occurred, the memory of primary crystallization may or may not be preserved. If U–Pb disturbance is recent, U–Pb data are discordant and distribute along a discordia line that passes through zero (blue points). Since Pb isotopes are not fractionated in detectable proportions in such disturbance, $^{207}Pb/^{206}Pb$ ratios still provide the primary crystallization age, which corresponds to the discordia upper-intercept (Fig. 4f) and is identical to the purple-filled ellipse which represents a concordant analysis from either the same zircon or the same population that remained unmodified. In contrast, for an old U–Pb disturbance, the datapoints would align along a discordia line that connects a lower-intercept corresponding to the age of U–Pb disturbance and an upper-intercept representing the actual crystallization age of zircon (red-filled ellipses in Fig. 4f). Most cases of discordance correspond to Pb-loss, which graphically corresponds to a migration of datapoints towards the lower end of a discordia line, and less common cases are associated with reverse discordance which reflects Pb accumulation (e.g. Williams *et al.* 1984; Kusiak *et al.* 2013). The case in which zircon contains measurable amounts of common-Pb (Pb_c) has not been presented here because, in most cases, it is a sign of zircon post-crystallization modification and/or advanced alteration. Consequently, data are generally discarded when ^{204}Pb is detected, since the Pb_c correction relies on knowledge of the isotopic composition of Pb when it entered the crystal, which is difficult to know in zircon.

Isotope geochemistry. The source of zircon parental magma can be assessed using multiple isotope systems, with the most common being Lu–Hf and O isotopes (e.g. Patchett 1983; Valley 2003). Lu–Hf isotopes in zircon are normally measured using MC-ICP-MS, either in solution or laser-ablation mode (e.g. Fisher *et al.* 2014*a*, *b*). The Lu–Hf isotope system is radiogenic and based on the decay of radioactive ^{176}Lu into ^{176}Hf with a half-life of *c.* 36 Ga (Scherer *et al.* 2001; Söderlund *et al.* 2004). The measured $^{176}Hf/^{177}Hf$ tracks the time-integrated fractionation of Lu from Hf in a reservoir (Fig. 4g). The principle of this technique is that during partial melting of most mantle and crustal lithologies, Hf and Lu are fractionated from each other, which results in magmas having Lu/Hf lower than that of the melting residue. Over time, melting residues (refractory mantle) develop very radiogenic (elevated) $^{176}Hf/^{177}Hf$ ratios (positive ε_{Hf}), and crustal lithologies (former magmas) comparatively low radiogenic ratios (negative ε_{Hf}) (Fig. 4g). For global interpretation, Hf isotope compositions are normalized to the Chondritic Uniform Reservoir (CHUR; Blichert-Toft and Albarède 1997; Bouvier *et al.* 2008; Iizuka *et al.* 2015) and transformed into epsilon Hf notation (ε_{Hf}), with CHUR approximating the bulk silicate Earth composition. For instance, Figure 4g illustrates a magma source produced by partial melting of the mantle at 2600 Ma (green spot in Fig. 4g) and that differentiates into mafic

and felsic lithologies, which are both characterized by specific $^{176}Lu/^{177}Hf$ content. These lithologies evolve after crystallization until 1500 Ma, when they are reworked by partial melting forming different granites (blue and red spots in Fig. 4g). Some of the generated melts mix with each other forming hybrid granites (grey spot in Fig. 4g). At 600 Ma, magmas extracted from the mantle (green spot in Fig. 4g) mix with crustal melts forming new hybrid granites (orange spot in Fig. 4g). Note that all crustal lithologies contain zircon, which allows the evolution of these reservoirs to be followed through time. Newly formed zircon domains (grains or overgrowths) within a single rock sample mostly have higher initial $^{176}Hf/^{177}Hf$ than older domains due to incomplete dissolution of detrital or magmatic zircon grains (hosting most of the non-radiogenic Hf). Also, metamorphic zircon incorporates additional radiogenic ^{176}Hf formed by ^{176}Lu decay in the rock's matrix between successive zircon growth events (Gerdes and Zeh 2009).

Oxygen isotopes are stable isotopes and the measured $^{18}O/^{16}O$, and possibly $^{17}O/^{16}O$ when the triple-isotope system is used, tracks isotope fractionations due to magmatic processes and/or sources. These light isotopes do not fractionate much during magmatic processes (i.e. partial melting and fractional crystallization), but differences can be measured (e.g. Valley 2003; Bindeman 2008). Most O isotope studies in zircon use the source-tracing potential of O isotopes, taking advantage of large O isotope fractionation caused by low-temperature alteration of crustal lithologies inducing clay formation and resulting in enrichment of ^{18}O relative to ^{16}O. Much like the Lu–Hf isotope system, O isotope ratios are difficult to interpret as numerical values. Therefore, O isotope ratios are normalized relative to the international Vienna standard mean ocean water (VSMOW) and reported in the standard delta ($\delta^{18}O$) notation. Zircon formed from a reworked clay-rich crustal lithology may have $\delta^{18}O$ up to +12‰ (Valley *et al.* 2005; Kemp *et al.* 2007), and mantle zircons have consistent $\delta^{18}O$ of $+5.3 \pm 0.6$‰ (Valley 2003). Zircon $\delta^{18}O$ values below that of the mantle indicate that zircon parental melt interacted with meteoric fluids and/or was altered at high temperatures (Valley 2003 and references therein). Most studies using O isotopes in zircon interpret O isotope variations as evidence for mixtures between mantle- and crustal-derived melts and/or fluids or crustal contaminants (e.g. Kemp *et al.* 2007; Smithies *et al.* 2021). Recent studies have demonstrated that the uptake of water into the zircon crystal lattice can significantly modify its oxygen isotopic composition (Pidgeon *et al.* 2017; Liebmann *et al.* 2021). Therefore, monitoring of the $^{16}O^{1}H/^{16}O$ ratio during SIMS oxygen isotope measurements to assess secondary modification of O isotope composition by water addition is recommended (Liebmann *et al.* 2021).

Recently, new stable isotope systems such as Si and Zr have been applied to zircon. Different techniques such as SIMS, MC-ICP-MS and LA-MC-ICP-MS have been employed to measure Si isotopes in zircon, which have resulted in good precision and closely mimic the natural variability of high-temperature processes (Trail *et al.* 2018, 2019; Guitreau *et al.* 2020, 2022). Si isotopes can be used to trace the origin of zircon parental magma due to the various silicon isotope signatures found in different types of igneous rocks (e.g. I, A, S, tonalite–trondhjemite–granodiorite (TTG); Savage *et al.* 2014; Deng *et al.* 2019). Si isotope compositions, expressed as permil deviations from a quartz standard ($\delta^{29}Si$ and $\delta^{30}Si$), are sensitive to the SiO_2 content, which reflects the degree of polymerization and crystallization temperature (Qin *et al.* 2016; Trail *et al.* 2019; Guitreau *et al.* 2022). This allows for reconstructions of the magma evolution. Changes in Si isotope compositions can occur due to metamorphic alteration and/or zircon recrystallization, which are dependent on the metamorphic grade (Guitreau *et al.* 2022).

Zr isotopes can be measured using conventional MC-ICP-MS instruments in solution or laser mode and applied to track fractional crystallization processes (Ibañez-Mejia and Tissot 2019; Zhang *et al.* 2019; Guo *et al.* 2020; Tian *et al.* 2020). Recent studies attributed measurable Zr isotope variations to kinetic fractionation in response to chemical gradients rather than equilibrium processes (Chen *et al.* 2020; Méheut *et al.* 2021). Zirconium isotope compositions of metamorphic zircon compared to igneous zircon may also result from chemical gradient effects (Zhang *et al.* 2019). This technique can hence provide insights into magmatic crystallization dynamics.

Thermometry. Zircon is used as a mineral pair thermometer based on incorporation of Ti into zircon at *HT* coupled with Zr substitution in rutile (Zack *et al.* 2004*a*; Watson and Harrison 2005; Watson *et al.* 2006; Ferry and Watson 2007). This technique requires the presence of both zircon and rutile within the mineral paragenesis, otherwise all temperatures are minimum estimates (Watson and Harrison 2005). Magmatic and metamorphic temperatures can also be overestimated at low pressures (<5 kbar) (Rubatto 2017). Temperature variations within an investigated sample have been interpreted to reflect waves of magmatic pulses within a magma chamber generating thermal and compositional heterogeneities (e.g. Collins *et al.* 2016; Volante *et al.* 2020*a*). Low diffusivity of Ti within zircon was previously measured perpendicular to the crystallographic c-axis (Cherniak and Watson 2007), making

this thermometry a widely used tool. In contrast, recent experiments conducted parallel to the c-axis found significant anisotropy in the diffusivity of Ti (Bloch *et al.* 2022). When extrapolated, the resulting diffusivities are *c.* 7.5–11 times faster at 950–650°C than the original experiments, indicating that this thermometer can be modified under elevated crustal temperatures, slow cooling and/or small grain sizes (Bloch *et al.* 2022). Moreover, since this thermometer is dependent upon alpha-quartz and t-TiO_2 activities, software such as Rhyolite-MELTS Gualda *et al.* (2012) have been proposed to improve temperature estimates' precision (e.g. Schiller and Finger 2019). The latter tool is useful and intuitive to use, however its caveats (Volante *et al.* 2020*a*) and its relatively low precision of about 50°C (Guitreau *et al.* (2022)) should be considered.

Titanite

Titanite ($Ca[Ti,Al,Fe^{3+}]SiO_4[O,OH,F,Cl]$) (Fig. 2g-i; Fig. 5) can occur as minor or accessory mineral and it is a particularly efficient chemical reactant with other major mineral phases that contain Ca and Ti, commonly leading to re-crystallization (Frost *et al.* 2001). Titanite commonly grows during magmatic (e.g. Ca-rich granitic rocks), metamorphic (e.g. calc-silicate, amphibolite) and hydrothermal events (Fig. 5a-c), with each different setting resulting in different titanite REE compositions that can be tracked by trace element fingerprinting (see reviews by Frost *et al.* 2001; Kohn 2017). Titanite commonly forms in mafic and calc-silicate rocks, and its growth can provide valuable time constraints in cases where other accessory minerals do not develop. Titanite crystallizes over a broad *P–T* range, including growth after breakdown of rutile, which is commonly stable at higher pressures (>1.4 GPa), ilmenite, Fe–Ti oxide stable at higher temperatures (>650/700°C), magnetite and/or clinozoisite (Frost *et al.* 2001; Kohn 2017). The combined acquisition of geochronological and geochemical data in texturally controlled titanite has robustly discriminated between distinct metamorphic, hydrothermal and magmatic events, and provided the opportunity to evaluate physical and chemical processes at the micro-scale in titanite-bearing rocks (e.g. Stearns *et al.* 2015; Garber *et al.* 2017; Olierook *et al.* 2019; Cavosie *et al.* 2022; Walters *et al.* 2022). However, petrological and chemical complexities can challenge U–Pb and *P–T* data interpretation. For instance, overgrowths of multiple metamorphic and hydrothermal titanite generations can significantly affect and modify the U–Pb system (e.g. Storey *et al.* 2006; Marsh and Smye 2017; Kirkland *et al.* 2018) and trace element compositions (e.g. Gordon *et al.* 2021), inducing decoupling of titanite U–Pb dates and trace element compositions (e.g. Romer and Rötzler 2001, 2011; Castelli and Rubatto 2002; Bonamici and Blum 2020; Walters *et al.* 2022).

Geochemical tools. Texturally, both magmatic and metamorphic (or hydrothermally altered) titanite can exhibit complex compositional zoning (Fig. 5a–c) and associated trace element (TE) patterns related to fluid–rock interaction (e.g. Smith *et al.* 2009; Garber *et al.* 2017; Olierook *et al.* 2019; Walter *et al.* 2021; Walters *et al.* 2022). Titanite preferentially incorporates minor and TE including U, high field-strength elements (HFSEs) such as Zr and REEs (e.g. Tiepolo *et al.* 2002; Lucassen *et al.* 2012), compared to other accessories (e.g. zircon, monazite). Trace element in titanite can provide information about crystallization pressure and temperature estimates (Hayden *et al.* 2008), oxygen fugacity (e.g. King *et al.* 2013; Cao *et al.* 2015) and fractionation processes (e.g. Piccoli *et al.* 2000; John *et al.* 2011). Geochemical and experimental studies on titanite suggest that it preferentially incorporates the medium rare earth element (MREE) in its crystal structure when in equilibrium with melt (e.g. Tiepolo *et al.* 2002; Prowatke and Klemme 2005; Olin and Wolff 2012), whereas recent petrochronological works show that melt-present and melt-absent metamorphic titanite have different REE patterns strongly depending on the presence and/or abundance of other phases in equilibrium with them (e.g. Garber *et al.* 2017; Walter *et al.* 2021; Walters *et al.* 2022). For instance, different TE uptake in titanite allowed Garber *et al.* (2017) to discriminate between (i) LREE-enriched (Precambrian) igneous cores, (ii) LREE-depleted and HREE-rich (Caledonian) recrystallized metamorphic rims likely associated with fluid or melt and (iii) (Caledonian) neocrystallized metamorphic titanite reflecting a negative or more positive REE slope based on whether titanite grew in equilibrium with hornblende and garnet or with allanite, apatite, plagioclase and biotite, respectively, during prograde and/or retrograde amphibolite-facies metamorphism (Fig. 5d, e; see also Cioffi *et al.* 2019; Walter *et al.* 2021).

Recent studies have highlighted the potential of TE in titanite as petrogenetic discriminator/indicator in magmatic, metamorphic and detrital studies (e.g. Ma *et al.* 2019; Olierook *et al.* 2019; Scibiorski and Cawood 2022). For example, Olierook *et al.* (2019) show that Fe concentrations and Th/U and Th/Pb ratios are systematically higher in magmatic than metamorphic titanite, reflecting useful petrogenetic discriminators when plotted against Al and Zr-in-titanite temperature (*T*°C), respectively (Fig. 5f–h). Also, normalized LREE/MREE, LREE/HREE and Eu anomalies reflect negative and/or positive REE slope correlations, which are useful to complement the characterization of titanite

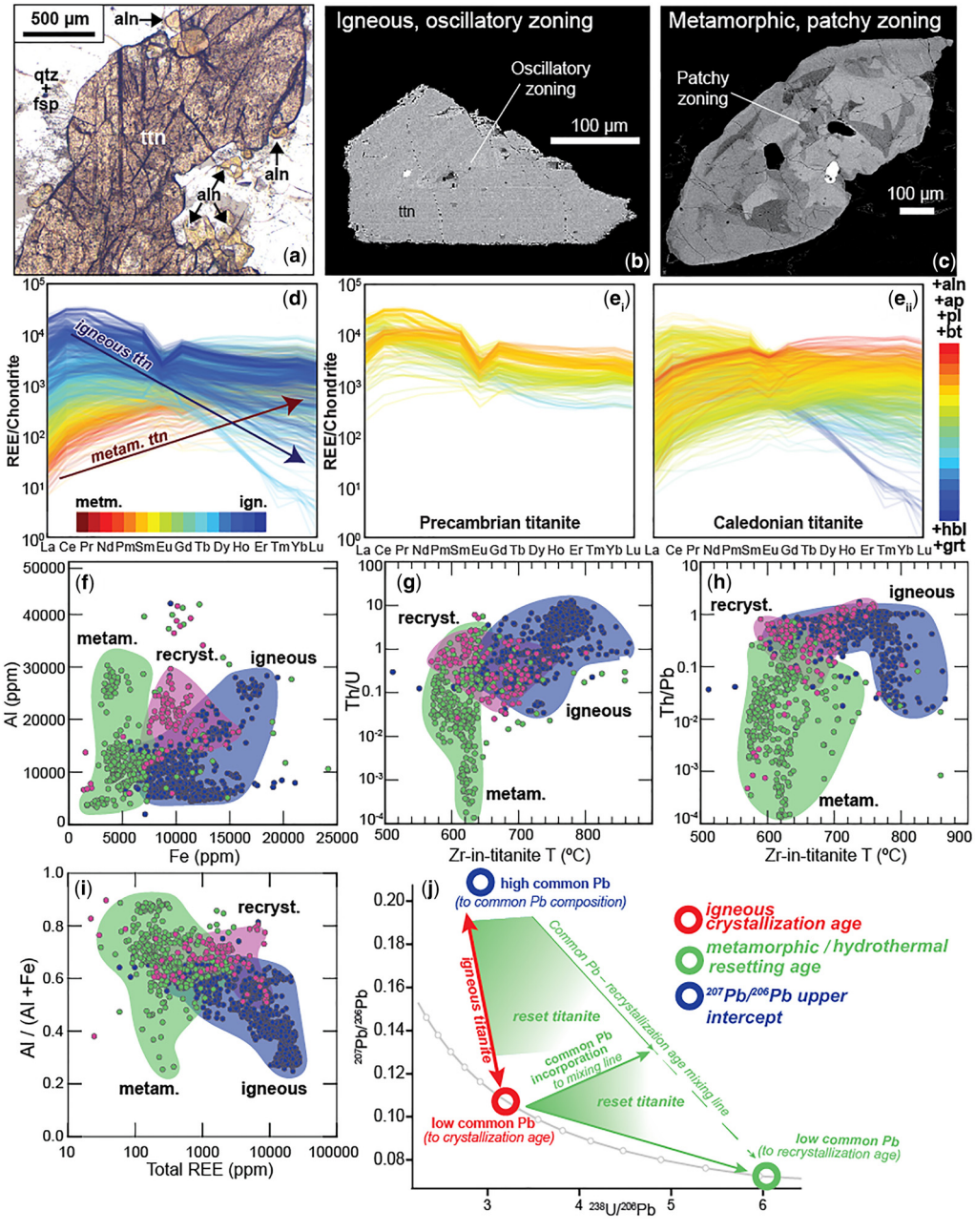

Fig. 5. Titanite. (**a**) titanite in orthogneisses. (**b**) Oscillatory zoning in igneous titanite. (**c**) Patchy zoning in metamorphic titanite. (**d**) REE patterns in magmatic and metamorphic titanite. (**e**) Slopes of REE patterns are affected by other mineral phases growing in equilibrium with (i) igneous Precambrian and (ii) metamorphic Caledonian titanite grains. (**f**) Al v. Fe. (**g**) Th/U v. Zr-in-titanite. (**h**) Th/Pb v. Zr-in-titanite. (**i**) Al/(Al + Fe) v. total REE discrimination diagrams to distinguish between igneous (in red), recrystallized (in purple) and metamorphic (in green) titanite. (**j**) Schematic Tera–Wasserburg concordia diagram for interpreting U–Pb titanite data. Source: (a), (c), (d) and (e) modified after Garber *et al.* (2017); (b), (i) and (j) modified after Olierook *et al.* (2019).

origin (Olierook *et al.* 2019). TE-based discrimination can be corroborated with detailed textural investigation of titanite grains, which are commonly characterized by oscillatory or sector zoning when magmatic in origin, with patchy and/or homogeneous zoning in metamorphic grains (e.g. Smith *et al.* 2009; Garber *et al.* 2017; Walters and Kohn 2017; Cioffi *et al.* 2019; Holder and Hacker 2019). Scibiorski and Cawood (2022) show that different titanite host-rock lithologies are reflected in the variation of TE chemistry, with low Zr/Y and high Fe in titanite from felsic host-rocks. This complements Al/Fe v. ΣLREE and U v. Th contents (ppm) used to discriminate magmatic v. metamorphic titanite (Olierook *et al.* 2019; Scibiorski and Cawood 2022; Fig. 5i) and between metamorphic, recrystallized and inherited igneous titanite (fig. 2 in Scibiorski and Cawood 2022), respectively. Also, systematic integration of titanite microstructural investigations by electron backscatter diffraction (EBSD) with *in situ* U–Pb petrochronology was proved to be a powerful tool not only to untangle and reconstruct complex deformation histories within crustal-scale high-strain zones but also to constrain deformation mechanism associated with shock and thermal metamorphism (Papapavlou *et al.* (2017); McGregor *et al.* 2021).

Geochronology. Titanite is a powerful U–Pb petrochronometer recording different primary and secondary geological processes (Spandler *et al.* 2016; Ma *et al.* 2019; Fisher *et al.* 2020; Barla 2021). However, titanite and other accessories including rutile, apatite and allanite tend to incorporate significant Pb_c (e.g. Kirkland *et al.* 2017, 2018; Bonamici and Blum 2020), which is reflected in discordant U–Pb ratios (e.g. Marsh and Smye 2017), making U–Pb dates interpretation of these accessory phases challenging (e.g. Olierook *et al.* 2019; Walters *et al.* 2022). Figure 5j (modified after Olierook *et al.* 2019) represents a schematic TW diagram (Tera and Wasserburg 1972) illustrating how titanite U–Pb data (and the other phases that commonly have Pb_c), including Pb_c (see Storey *et al.* 2006; Kirkland *et al.* 2017), crystallization and recrystallization mixing lines can be interpreted (e.g. Spencer *et al.* 2013; Bonamici *et al.* 2015; Garber *et al.* 2017; Papapavlou *et al.* 2017; Holder and Hacker 2019; Mottram *et al.* 2019; Timms *et al.* 2020; Gordon *et al.* 2021). As a result of Pb_c incorporation in the crystals, geochronological data typically form an intercept line (red line in Fig. 5j, 'igneous titanite ages') characterized by a $^{207}Pb/^{206}Pb$ upper intercept and lower concordia intercept (e.g. Spencer *et al.* 2013; Chew *et al.* 2014; Garber *et al.* 2017; Kirkland *et al.* 2017, 2018, 2020), with the igneous age being calculated using the lower one. However, when such intercept line is not statistically robust, then (i) a weighted mean of uncorrected dates can be calculated, if they are within 2SD uncertainty (e.g. Spencer *et al.* 2016; Olierook *et al.* 2019; Barrote *et al.* 2022*b*), or (ii) the upper intercept can be used to calculate concordant analyses with negligible Pb_c (Olierook *et al.* 2019). U–Pb dates of samples affected by overprinting events would fall in a space in the TW diagram defined by a $^{207}Pb/^{206}Pb$ upper intercept, a first lower concordia intercept recording the first magmatic/metamorphic event and a second lower concordia intercept recording the subsequent event (green triangular shape in Fig. 5j). Titanite is also found to yield non-typical Pb_c values, possibly due to inheritance of radiogenic Pb into the crystal structure (Kirkland *et al.* 2018; Mottram *et al.* 2019; Walters *et al.* 2022).

Additionally, an important factor to consider when dealing with titanite geochronology is *Tc* (Fig. 1; Dodson 1973). In the past two decades, it has been shown that titanite is much more retentive than previously envisaged (with *Tc* of *c.* 600–650° C, Mezger *et al.* 1991; 600–650°C, Scott and St-Onge 1995, Frost *et al.* 2001; 650 and 750°C, Cherniak 1993), increasing the temperature threshold for Pb and Zr volume diffusion in titanite as high as *c.* 750–840°C (*c.* 740°C, e.g. Schärer *et al.* 1994, Zhang and Schärer 1996; >750°C, e.g. Kylander-Clark *et al.* 2008, Kohn and Corrie 2011, Gao *et al.* 2012, Spencer *et al.* 2013, Stearns *et al.* 2015, Kohn 2017; >830°C, e.g. Hartnady *et al.* 2019, Holder *et al.* 2019, Kirkland *et al.* 2020) and challenging the assumption that titanite U–Pb dates commonly reflect cooling ages (Hartnady *et al.* 2019; Kirkland *et al.* 2020).

Isotope geochemistry. While less explored compared to other accessory minerals such as monazite, Sm–Nd isotope systematics in titanite (e.g. Yang *et al.* 2008; Amelin 2009; Fisher *et al.* 2011, 2020; Hammerli *et al.* 2014; Spandler *et al.* 2016; Ma *et al.* 2019; Zhang *et al.* 2021) has potential as a source tracer for understanding the formation and evolution of the crust (Amelin 2009; Fisher *et al.* 2020; Zhang *et al.* 2021). This isotopic system has been demonstrated to have high *Tc* (850–950°C; Cherniak 1995), surviving HT magmatic, metamorphic and hydrothermal conditions. *In situ* Sm–Nd isotopic systematics of titanite can be used to trace fluid, melt or crustal/juvenile rock sources (e.g. Lucassen *et al.* 2011; Hammerli *et al.* 2014; Spandler *et al.* 2016; Zhang *et al.* 2021).

Experimental studies have demonstrated that oxygen diffusion in accessory minerals is slower than in rock-forming minerals (e.g. Fortier and Giletti 1989), but oxygen diffusion in apatite is faster than in titanite, which is in turn faster than in zircon (Bruand *et al.* 2019). Oxygen isotopes in magmatic and metamorphic titanite have been used as a

geochemical indicator to investigate magma petrogenesis as well as metamorphic and hydrothermal overprinting events (e.g. King *et al.* 2001; Bonamici *et al.* 2011, 2014, 2015; Bruand *et al.* 2019). For example, Bonamici *et al.* (2014) differentiated four generations of titanite with distinct $\delta^{18}O$ values and internal textural zoning. Also, consistent results between $\delta^{18}O$ in titanite and zircon indicate that titanite is a robust accessory mineral preserving the original magmatic $\delta^{18}O$ composition (Bruand *et al.* 2019).

Thermometry. A thermometer using the Zr content in titanite (Zr-in-titanite) was developed by Hayden *et al.* (2008), relying on the direct substitution of Zr^{4+} for Ti^{4+}, whereas pressures can be estimated from the net transfer reaction $_2Ca_2\ Al_3Si_3O_{12}(OH) + TiO_2 + SiO_2 = 3CaAl_2Si_2O_8 + CaTiSiO_5 + H_2O$ (referred to as TZARS; Kapp *et al.* 2009), using automated calculations in THERMOCALC (Holland and Powell 2011). The Zr-in-titanite thermometer covers a wide temperature range and is pressure dependent, resulting in large pressure uncertainties and rutile activity in rutile-absent rocks, limiting the reliability of temperature estimates. Therefore, modelling titanite within a mineral paragenesis using software such as THERMOCALC allows for pressure estimates with errors less than *c.* 0.1 GPa (Kohn *et al.* 2017).

Rutile

Rutile (Fig. 2j-l; Fig. 6) is the high-temperature TiO_2 polymorph (Dachille *et al.* 1968) and a common accessory mineral that occurs in metamorphic (U) high-pressure (UHP) mafic rocks (Fig. 6a; e.g. Zack *et al.* 2004*b*; Triebold *et al.* 2012; Zack and Kooijman 2017; Böhnke *et al.* 2019), in moderate-pressures and moderate-temepratures to *HP* and *HT* metapelitic rocks (Fig. 6b; e.g. Hart *et al.* 2018; Gonçalves *et al.* 2019) and in low-temperature/hydrothermal metapelitic rocks (Fig. 6c; e.g. Plavsa *et al.* 2018; Salama *et al.* 2018; Agangi *et al.* 2019; Porter *et al.* 2020; Schirra and Laurent 2021). In contrast, rutile occurrence in magmatic rocks is limited to *HT* and dry alkaline, kimberlite or pegmatitic rocks (e.g. Carruzzo *et al.* 2006; Cerny *et al.* 2007). At low-*T* (LT) and low-*P* (LP) conditions, rutile is no longer stable, and it is replaced by polymorphs anatase (tetragonal) and brookite (orthorhombic), respectively, whereas rutile *HP* polymorph is TiO_2(II) (Dachille *et al.* 1968; Jamieson and Olinger 1969). During prograde metamorphism, rutile growth is attributed to breakdown of ilmenite, titanite and biotite (Zack and Kooijman 2017). Rutile popularity as a petrochronometer has exponentially increased due to its multifaceted potential to investigate tectonic processes as single-mineral thermometer (e.g. Zack *et al.* 2004*a*; Watson *et al.* 2006; Tomkins *et al.* 2007; Luvizotto and Zack 2009), geochronometer (e.g. Mezger *et al.* 1989*a*), geospeedometer (Cruz-Uribe *et al.* 2014; Kohn *et al.* 2016), as a provenance indicator (e.g. Triebold *et al.* 2012; Pereira and Storey 2023) and as an isotopic tracer (e.g. Ewing *et al.* 2011). Additionally, the increasing sensitivity of analytical equipment has enabled dating of low-U phases such as rutile (Luvizotto *et al.* 2009; Axelsson *et al.* 2018; Verberne *et al.* 2019; Moore *et al.* 2020*b*).

Geochemical tools. Rutile primarily incorporates high field strength elements (HFSE; i.e. Nb, Ta, Zr, Hf and Cr; Rudnick *et al.* 2000; Zack *et al.* 2002; Schmidt *et al.* 2009). These can be used (i) to characterize micro-scale processes associated with growth of rutile crystals (e.g. Hart *et al.* 2018; Verberne *et al.* 2022*a*); (ii) as a pressure-proxy, such that trace element budget (i.e. Na and Ta) in the melt rutile crystallized in reflects the depth at which partial melting of the source rock occurred (e.g. Foley *et al.* 2002; Moyen and Stevens 2006; Meyer *et al.* 2011; Kooijman *et al.* 2012); or (iii) as geochemical pathfinders for mineralized rocks (Clark and Williams-Jones 2004; Smythe *et al.* 2008; Pochon *et al.* 2017; Plavsa *et al.* 2018; Agangi *et al.* 2019; Ballouard *et al.* 2020; Porter *et al.* 2020; Sciuba and Beaudoin 2021). While HFSE are compatible in rutile, other trace elements including Sr, Th and REEs are incompatible (Klemme *et al.* 2005; Meyer *et al.* 2011). Trace element concentrations between the three TiO_2 polymorphs (rutile, anatase and brookite) systematically differ, leading to erroneous results when applying the Zr-in-rutile thermometer or Cr and Nb discrimination diagrams (see below) to phases other than rutile (Triebold *et al.* 2012).

Lithology discrimination schemes from Triebold *et al.* (2012) and Meinhold *et al.* (2008) using Cr and Nb (ppm) content in rutile as well as Zr/Hf and Nb/Ta ratios are useful to identify the protolith composition (metapelitic v. metabasic). However, care must be taken when applying this technique for source discrimination in provenance studies due to documented unsystematic Nb/Cr ratios for rutile from amphibolite-facies rocks potentially reflecting TE disturbance during retrogression or prolonged HT metamorphism (Meyer *et al.* 2011; Kooijman *et al.* 2012). Additionally, the application of principal component analysis (PCA) on rutile from Precambrian UHT and Phanerozoic HP terranes (Hart *et al.* 2018), as well as on ore-bearing and barren metamorphic and magmatic rocks (Plavsa *et al.* 2018; Pereira *et al.* 2019; Porter *et al.* 2020) indicates that several TE can be used for lithological discrimination (van Schijndel *et al.* 2021) and to distinguish rutile from mineralized v. barren rocks. For example,

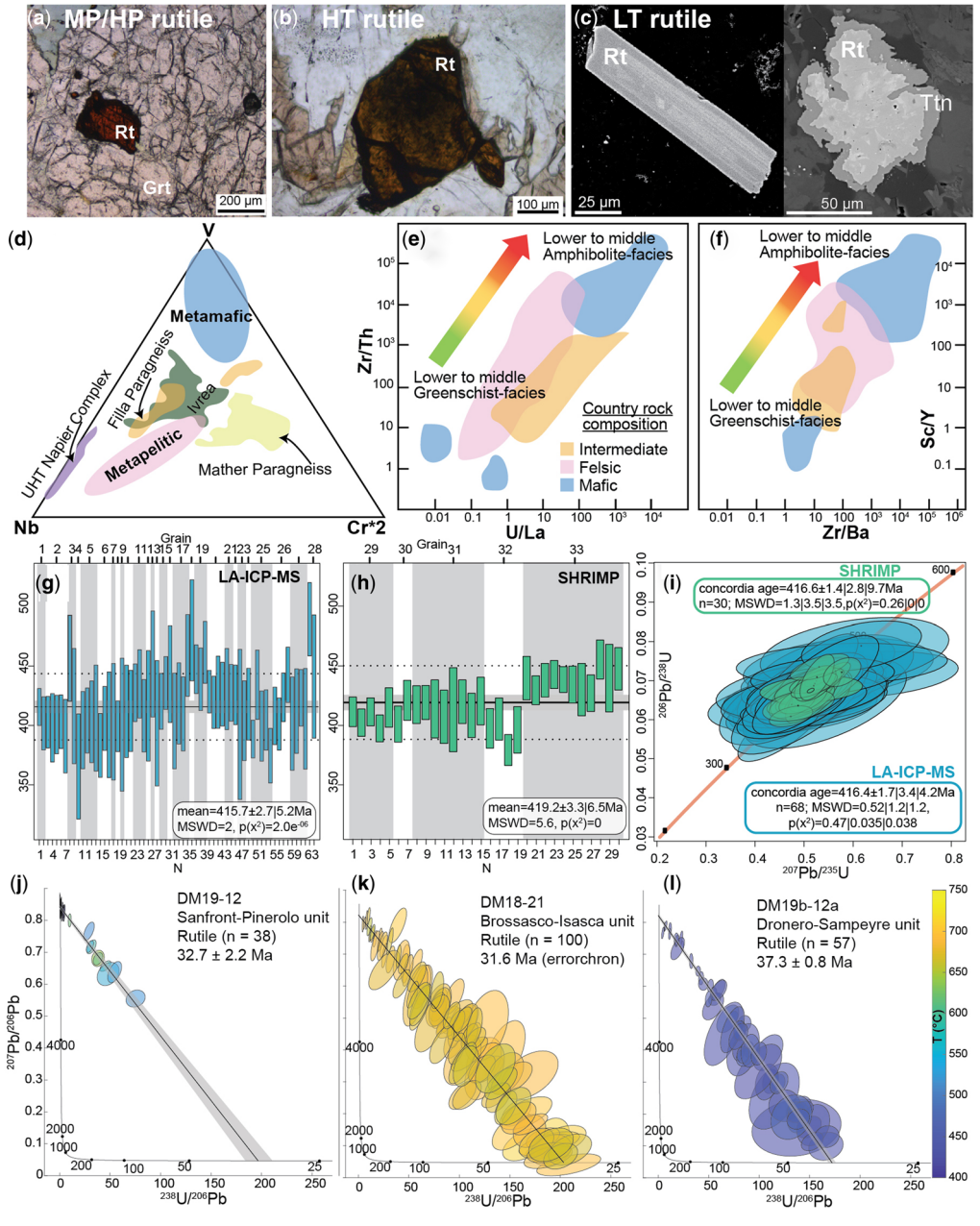

Fig. 6. Rutile textures in (**a**) rutile inclusion in garnet from a HP mafic eclogite from the Sanbagawa belt, SW Japan. (**b**) HT rutile from an orthopyroxene–cordierite granulite from Madagascar. (**c**) LT rutile. Left: a BSE image of tabular rutile with a high W core (W-rt) from the Speewah carbonatite, Australia. Right: rutile grain from the Boddington Au–Cu deposit with patchy W zonation and coronitic titanite. (**d**) Nb–V–Cr ternary discrimination diagram for rutile. Binary plots of rutile (**e**) U/La v. Zr/Th and (**f**) Zr/Ba v. Sc/Y trace element ratios from orogenic gold deposits; (**g–i**) U–Pb data for LA-ICP-MS and SHRIMP analyses for porphyroblastic rutile. Weighted mean age of individual analyses for (g) LA-ICP-MS and (h) SHRIMP data. (i) U–Pb concordia diagram, ellipses representing the 2σ uncertainty; (**j–l**) TW plots and isochrons/errorchrons combined with Zr-in-rutile thermometry. Source: (a and b) photo courtesy of Pereira; (c) modified after Porter *et al.* (2020); (d) modified after Hart *et al.* (2018); (e) and (f) modified after Sciuba and Beaudoin (2021); (g–i) modified after Moore *et al.* (2020*b*); (j–l) modified after Bonnet *et al.* (2022).

the Nb–V–Cr ternary diagram shows that rutile from HP metamafic rocks is commonly V-rich, whereas in metapelites is more Nb-rich (Fig. 6d; Hart *et al.* 2018). When associated with mineralized systems, rutile contains anomalous concentrations of V, Sn, Sb, W, Ni, Cu, Cr, Ta, Nb and Fe (e.g. Scott and Radford 2007; Plavsa *et al.* 2018; Porter *et al.* 2020), where W and Cr variability is used to discriminate its origin from mineralized or barren rocks (Porter *et al.* 2020). It is also possible to identify rutile deriving from pegmatitic rocks (high Nb, Ta, Sn) and Au-ore, which are enriched in Sb. This can also be done by combining multi-element clustering of PCA analysis (Porter *et al.* 2020; Sciuba and Beaudoin 2021). However, due to the systematic differences in trace element contents between the three TiO_2 polymorphs, a detailed characterization of the analysed grains is recommended using either EBSD or Raman spectroscopy (Plavsa *et al.* 2018; Porter *et al.* 2020; Sciuba and Beaudoin 2021). Multi-variant statistical analysis of rutile TE composition, particularly variations in Sc, REE, Y, Ca, Ba, Th, Zr, U and V, can reflect different metamorphic grades experienced by the country rock (Sciuba and Beaudoin 2021). For example, mafic and ultramafic, lower to middle greenschist-facies country rocks have lower Zr/Th and U/La ratios than intermediate and sedimentary greenschist facies one (Fig. 6e; Sciuba and Beaudoin 2021). A similar trend is observed for relative concentrations of Sc/Y and Zr/Ba, where lower and higher contents reflect lower and higher metamorphic grade, respectively (Fig. 6f; Sciuba and Beaudoin 2021). Also, the identification of localized TE enrichment along twin interface in rutile grains using atom probe tomography is interpreted to occur via volume diffusion during *HT* metamorphism (Verberne *et al.* 2022*a*).

Geochronology. Vry and Baker (2006) calculated the *Tc* of Pb diffusion in rutile to be between 500 and 540°C, based on natural samples (Fig. 1). For a spherical rutile of 200 µm, experimental data from Cherniak (2000*a*) predict whole-grain *Tc* of *c.* 600°C at an average cooling rate of 2–3°C/Ma, and above *c.* 640°C for Zr in rutile (2°C/Ma cooling rate; Cherniak *et al.* 2007; Dohmen *et al.* 2019). This moderate *Tc* for rutile implies that it is possible to find crystallization ages in cores of larger rutile crystals, especially if cooling is very fast. The preservation of a crystallization/growth age depends on several factors including max metamorphic temperatures, cooling rates and grain size (Kylander-Clark *et al.* 2008; Zack and Kooijman 2017; Moore *et al.* 2020*b*), and a multi-proxy approach may be needed to distinguish between different metamorphic and deformation stages. For example, Moore *et al.* (2020*b*) used rutile Zr thermometry, SHRIMP U–Pb age determination and electron backscatter diffraction (EBSD) microstructural analyses to identified two-stage rutile age populations which were not distinguishable using LA-ICP-MS data alone (Fig. 6g–i). Due to low-U content in rutile (<0.1 ppm; see Zack *et al.* 2011), it is important to first determine the U content to obtain meaningful metamorphic and/or magmatic ages (Zack *et al.* 2002, 2004*b*, 2011). Low-U content can lead to a high common v. radiogenic Pb ratio; therefore, monitoring the $^{206}Pb/^{208}Pb$ ratio and application of the ^{208}Pb correction method is recommended (Zack *et al.* 2011). An application of this method allows the investigation of age variations within a single rutile grain, where transects from core to rim give younger ages towards the rim as a result of Pb diffusion during cooling and provide a temperature–time trajectory (Kooijman *et al.* 2010). In contrast to rutile geochronology obtained with LASS-ICP-MS, recent atom probe investigations indicate evidence for heterogeneous Pb and trace element distribution at the nanoscale (Verberne *et al.* 2020). Nonetheless, at the microscale (>20 µm), TE variations in a rutile single grain are negligible and concordant U–Pb dating is obtained, indicating that nanoscale defects do not significantly impact the micro-scale analysis (Verberne *et al.* 2020).

Isotope geochemistry. In situ analysis of Hf isotopes in rutile (Sláma *et al.* 2007; Ewing *et al.* 2011, 2014) has been applied to trace metasomatic processes in the lithospheric mantle (Choukroun *et al.* 2005; Aulbach *et al.* 2008) and recycling of continental material in the mantle (Ewing and Müntener 2018). Despite the relatively low Hf content (<300 ppm Hf), the $^{176}Hf/^{177}Hf$ of rutile can be accurately measured *in situ* by LA-MC-ICP-MS, provided care is taken with the analytical protocol and data reduction process (Ewing *et al.* 2011; Ewing and Müntener 2018). Matrix matched standards and a ^{176}Hf signal intensity above 10 mV are necessary, requiring a large spot size of >160 µm (Yang *et al.* 2015; Ewing and Müntener 2018). This technique is particularly interesting for rocks that lack zircon but contain rutile, such as mafic lithologies, with low Hf concentrations (Ewing *et al.* 2011). In contrast, rutile from (U)HT felsic granulites can contain much higher Hf contents, ranging from 20 to 400 ppm (Ewing *et al.* 2013).

Thermometry. The solubility of ZrO_2 in rutile is strongly temperature-dependent, and Zr-in-rutile has been identified as a useful thermometer (ZiR) when the rutile coexists with the appropriate buffer assemblage, i.e. zircon + quartz (Zack *et al.* 2004*a*; Watson *et al.* 2006; Tomkins *et al.* 2007; Hofmann *et al.* 2013). Underestimation of the calculated temperatures occurs when the rutile grows in the absence of zircon and/or in partially reset

mineral assemblages (Zack *et al.* 2004*a*; Harley 2008). Possible biases include micro-inclusions of zircon (Zack *et al.* 2004*a*), prograde relict grains or incomplete equilibration with quartz (high Zr-rutile) or zircon (low-Zr rutile) due to slow diffusion along grain boundaries (see discussions in Taylor-Jones and Powell 2015; Kohn *et al.* 2016; Kohn 2020). Decoupling between Ti-in-zircon and Zr-in-rutile thermometry during UHT metamorphism is recorded in rutile that occurs as inclusions in zircon (Lei *et al.* 2020). Diffusion of Zr within rutile and Zr loss are closely related to the distribution of Zr, duration of UHT metamorphism and rutile grain size (Dohmen *et al.* 2019; Lei *et al.* 2020). The Zr concentration in rutile (Zr-in-rutile) is temperature-sensitive over a large range of geologically significant temperatures (e.g. Zack *et al.* 2004*a*; Ewing *et al.* 2013; Wawrzenitz *et al.* 2015; Pape *et al.* 2016; Böhnke *et al.* 2019; Clark *et al.* 2019; Moore *et al.* 2020*b*; Adlakha and Hattori 2021; Campomenosi *et al.* 2021; Bonnet *et al.* 2022). This relationship has been experimentally calibrated by Watson *et al.* (2006) and Ferry and Watson (2007), and a significant pressure effect has been calibrated by Tomkins *et al.* (2007). The Zr-in-rutile thermometer was recently refined and now predicts temperatures up to 40°C lower for $T \leq 550$°C, and systematically higher temperatures for $T > 800$°C (Kohn 2020). With the new calibrations, precisions of ± 5°C and accuracy of *c.* ± 15°C may be possible, although a variable rutile composition may lead to larger uncertainties (Kohn 2020). Taylor-Jones and Powell (2015) showed that Zr can leave rutile and move along grain boundaries towards existing distal zircon.

Zr-in-rutile temperatures can record HT events, whereas U–Pb in rutile records cooling ages due to low *Tc* (Fig. 1). Rutile U–Pb ages likely postdate Zr temperatures following high-grade metamorphism and subsequent simple cooling, although a more complex history of episodic cooling and reheating may lead to more significant decoupling between Zr temperatures and U–Pb ages (e.g. Ewing *et al.* 2015). Bonnet *et al.* (2022) show the combined use of Zr-in-rutile and U–Pb ages for rutile occurrence in subduction complexes that may be interpreted as crystallization ages for the units that experienced high-pressure, low-temperature metamorphism, but not for the high-grade units (Fig. 6j–l).

Allanite

The term 'allanite' has been used to designate minerals from the allanite subgroup of the epidote group (Armbruster *et al.* 2006; Mills *et al.* 2009), which occurs in magmatic (Fig. 2m-o; Fig. 7a), metamorphic (from greenschist- to granulite-facies) and hydrothermal rocks (Janots *et al.* 2006, 2009; Rubatto *et al.* 2011; Airaghi *et al.* 2019). The allanite subgroup comprises a series of REE minerals with an ideal structural formula of $Ca(LREE^{3+})(Al)_2(Fe^{2+}, Fe^{3+})(SiO_4)(Si_2O_7)O(OH)$. The presence of LREEs as major constituents, the various element substitutions, the broad *P* and *T* stability field and the preservation of growth stages, make allanite one of the burgeoning protagonists in petrochronology (e.g. Rubatto *et al.* 2011; Manzotti *et al.* 2018; Airaghi *et al.* 2019). Compositionally, two main factors are crucial for its use in petrochronology: (i) REEs' sites can be occupied by Th^{4+} and U^{4+}, pivotal elements for geochronology (Gieré and Sorensen 2004), and (ii) REEs are exceptional tracers of geological processes (Hermann 2002; Engi 2017). Allanite often exhibits complex chemical zoning (Fig. 7a; Romer and Xiao 2005; Rubatto *et al.* 2011; Airaghi *et al.* 2019), requiring investigation via *in situ* methods (e.g. Burn 2016; Zhang *et al.* 2022).

Geochemical tools. Trace element composition of allanite depends on the interplay between the bulk rock composition and fractionation of these elements during mineral reactions. For instance, a decrease in the LREE in magmatic allanite can be observed in Ca-rich rocks → diorite and granodiorite → granite → syenite (Smye *et al.* 2014; Engi 2017). The Th/U ratios can be often used as a complementary tool (together with initial Pb_c lead values) to distinguish between magmatic (>100) and metamorphic (<50) grains or domains (Fig. 7b; Gregory *et al.* 2007, 2012; Di Rosa *et al.* 2020). REEs have also been used to discriminate distinct allanite growth stages in metamorphic and magmatic rocks (Fig. 7c; Manzotti *et al.* 2018; Corti *et al.* 2020). Corti *et al.* (2020) compared composition and internal structure of allanite crystals from metagranitoids recording different strain rates during HP and LT metamorphism, concluding that the matrix and allanite crystals accommodated plastic and brittle deformation, respectively. Allanite resistance to plastic deformation is a noteworthy characteristic, as evidenced by relicts preserved in the sheared eclogites from Monte Mucrone (Stünitz and Tullis 2001; Cenki-Tok *et al.* 2011). However, fracturing during brittle deformation can disturb its isotopic system (Burn 2016).

Despite the degree of deformation, the allanite grains exhibit the same sequence of chemical zoning pattern (evident for Ca and Ce), but with different textures and LREE contents, suggesting that deformation facilitates the release of LREEs (Fig. 7a, d and e; Corti *et al.* 2020). Gregory *et al.* (2012) used Th/U v. La/Sm and Eu/Eu* v. La/Sm discrimination diagrams to distinguish low- from high-temperature magmatic allanite, revealing useful information about the amount of melt present during allanite growth. However, no geochemical ratios

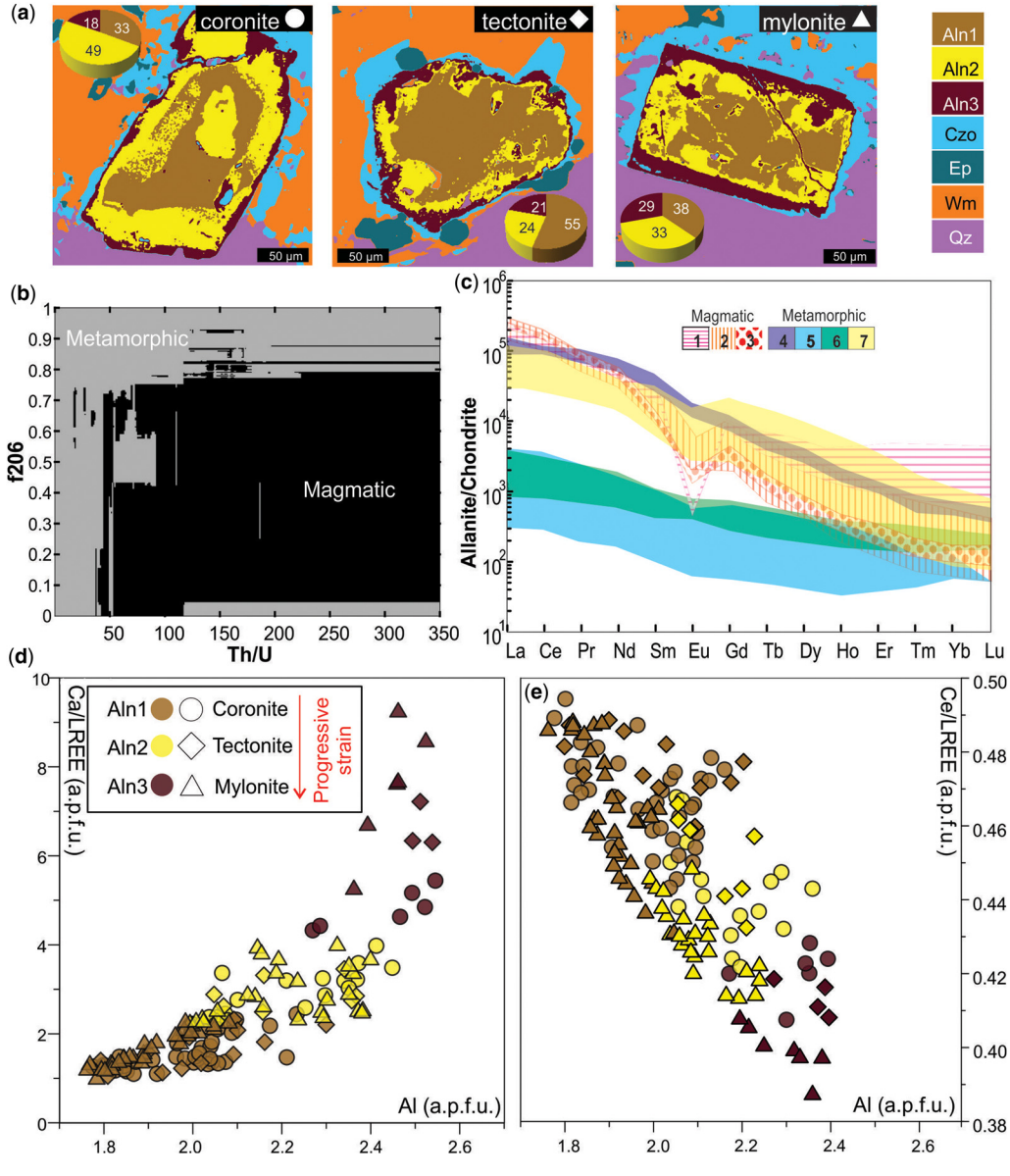

Fig. 7. (**a**) Quantitative X-ray Map Analyser images (Q–XRMA; Ortolano *et al.* 2018) used to distinguish generations of metaigneous allanite grains recording different strain rates. (**b**) Classification diagram to distinguish magmatic from metamorphic allanite based on their Th/U ratio and the fraction of initial ^{206}Pb (f206) values produced using machine learning (Random Forest algorithm). (**c**) Chondrite-normalized REE patterns of magmatic (pattern) v. metamorphic (filled) allanite: (1) Renna *et al.* (2007); (2) Gregory *et al.* (2012); (3) Zhang *et al.* (2022); (4) Regis *et al.* (2014); (5) Boston *et al.* (2017); (6) Vho *et al.* (2020); (7) Di Rosa *et al.* (2020). Use of geochemical data to distinguish magmatic and metamorphic allanite. Despite the degree of deformation of allanite crystals presented in (a) the same sequence of chemical zoning can be observed, with progressively deformed allanite crystals exhibiting variations of (**d**) Ca and (**e**) Ce contents in relation to LREE contents. Source: (a) from Corti *et al.* (2020); (b) modified after Di Rosa *et al.* (2020); (c) modified after Di Rosa *et al.* (2020).

have yet been found to systematically discriminate metamorphic from magmatic allanite (Di Rosa *et al.* 2020). In migmatitic rocks, allanite incorporates significant amounts of Th relative to melt (e.g. Hermann and Rubatto 2009), and it may exhibit intermediate Pb_c values, between those for

magmatic and metamorphic allanite (Gregory *et al.* 2012).

Geochronology. The favourable composition of allanite allows dating using the $^{232}Th/^{208}Pb$, $^{238}U/^{206}Pb$ and $^{235}U/^{207}Pb$ systems. Allanite dating techniques range from single and multi-grain ID-TIMS (e.g. von Blackenburg 1992; Oberli *et al.* 2004; Smye *et al.* 2014; López-Moro *et al.* 2017) to *in situ* analysis using SHRIMP, SIMS or LA-ICP-MS (e.g. Catlos *et al.* 2000; Janots *et al.* 2009; Darling *et al.* 2012; Regis *et al.* 2014; Burn *et al.* 2017; Giuntoli *et al.* 2018; Liao *et al.* 2020; Vho *et al.* 2020). Challenges in the use of allanite reference material for LA-ICP-MS and SHRIMP methods (Burn 2016) include: (i) chemical and isotopic heterogeneities (e.g. Gregory *et al.* 2007; Boston *et al.* 2017; Giuntoli *et al.* 2018); (ii) excess ^{206}Pb in magmatic allanite, which is the most widely used reference material (e.g. BONA, CAP and TARA allanite; Gregory *et al.* 2007; Burn *et al.* 2017; Yang *et al.* 2022); and (iii) use of non-matrix-matched reference materials (e.g. NIST610 glass by McFarlane 2016; Plešovice zircon in Burn *et al.* 2017). Nonetheless, robust LA-ICP-MS results have been obtained also by using zircon as primary reference material (Darling *et al.* 2012; Burn *et al.* 2017; Vho *et al.* 2020), which has a similar structure to allanite. Rastering (Darling *et al.* 2012) or a spot analyses routine (Burn 2016) can also be used to minimize matrix sensitivity in LA-ICP-MS analysis. As other accessory minerals, allanite may also incorporate non-radiogenic (^{204}Pb) as well as radiogenic Pb (intermediate nuclei from ^{238}U decay) affecting dates and uncertainties (Romer and Siegesmund 2003; Darling *et al.* 2012; Engi 2017). Furthermore, the structure of allanite can complicate geochronological procedures, as matrix matching reference materials is needed and the decay from ^{232}Th, ^{235}U and ^{238}U causes structural damage to the crystal lattice (Burn 2016; McFarlane 2016). The destruction of the crystalline structure promotes Pb-loss and/or actinide remobilization with the formation of Th- and U-rich mineral phases (e.g. Barth *et al.* 1994; Smye *et al.* 2014). Additionally, deformation and interaction with fluids may open isotopic systems and play an important role in mineral re-equilibration, resorption and precipitation (Radulescu *et al.* 2009; Airaghi *et al.* 2019; Corti *et al.* 2020). Thus, syn-kinematic allanite has been used to date deformation processes at upper to middle crustal levels (Cenki-Tok *et al.* 2011). Investigations of magmatic allanite from an intensely deformed Mesoproterozoic granite in southern Norway indicate that higher mobility of Th than Pb during deformation processes results in the U–Pb system being more reliable than the Th–Pb system (Burn 2016). Nevertheless, allanite crystal structure may protractedly recover by annealing (Karioris *et al.* 1981), forming preserved (non-metamict) crystals that may yield younger dates (Catlos *et al.* 2000). More recently, allanite has been used as primary and secondary reference material for epidote dating (Peverelli *et al.* 2022).

When dating allanite, one of the three approaches discussed by Burn (2016) and Engi (2017) should be utilized to deal with initial or Pb_c correction. (i) Consider Pb_c evolution models. This approach is more often used for magmatic (Barth *et al.* 1994) than metamorphic (e.g. Radulescu *et al.* 2009; Rubatto *et al.* 2011) rocks due to the main issue of using global (silicate Earth or mantle) evolution models. Th, U and Pb contents differ from rock to rock, and their distribution within minerals is heterogeneous. These factors depend on several variables such as local effective bulk composition and fluids availability (Lanari and Engi 2017). (ii) Measuring Pb_c in phases that coexist with allanite (e.g. Cenki-Tok *et al.* 2014), which can be hampered by the difficulty in interpreting coexisting phases. Finally, (iii) the 'intercept approach', in which intercepts from uncorrected TW and $^{206}Pb_c$ normalized Th–Pb isochron diagrams are used to estimate the initial Pb_c (e.g. Janots and Rubatto 2014; Airaghi *et al.* 2019). Gregory *et al.* (2012) indicate that igneous allanite tends to have smaller amounts of non-radiogenic ^{208}Pb than high-grade metamorphic rocks, whereas allanite crystals formed at subsolidus conditions exhibit the highest non-radiogenic ^{208}Pb values.

Isotope geochemistry. Allanite enrichment in LREE and Sr allows for both *in situ* Nd and Sr isotopic-based petrogenetic information to be combined with U–Th–Pb dating, making allanite an important petrogenetic tool (Hoshino *et al.* 2007). Heterogeneous Pb and Sr isotopic concentrations in allanite are demonstrated to be inherited from precursor minerals involved in allanite-producing metamorphic reactions (Romer and Xiao 2005). Zhang *et al.* (2022) combined U–Th–Pb dating and Nd isotopes of allanite with U–Pb–Hf analyses of zircon, demonstrating good correlations between the two systems to investigate crustal formation and evolution. Nd isotopes in allanite analysis were used by Su *et al.* (2021) to unravel the hydrothermal history of an iron oxide copper–gold deposit from ore formation (multi-source) to the post-ore overprinting tectonothermal events.

Monazite/xenotime

Monazite (LREE,Y,Th,Ca,Si)PO_4 is a REE-rich phosphate mineral (Fig. 2p-r) that occurs in a variety of rock compositions and from diagenetic (Evans and Zalasiewicz 1996; Pereira *et al.* this volume, in press) to granulite-facies conditions (Black *et al.*

1984). Monazite is common in peraluminous granites (e.g. Montel 1993; Förster 1998), syenite, granitic and quartz veins (e.g. Piechocka *et al.* 2017) and carbonatitic plutons (e.g. Anenburg *et al.* 2021; Kamenetsky *et al.* 2021), and can exhibit various textures (from sector, firtree, oscillatory to lobate; Fig. 8a). However, under certain fluid conditions, in particular alkali-bearing fluids, monazite undergoes coupled dissolution–reprecipitation (CDR) (Vavra and Schaltegger 1999; Harlov and Hetherington 2010; Harlov *et al.* 2011; Kelly *et al.* 2012; Taylor *et al.* 2014, 2016; Bosse and Villa 2019; Weinberg *et al.* 2020; Salminen *et al.* 2022). CDR of monazite leaves very distinctive, lobate textures but can also modify U–Pb systematics (Fig. 8b; e.g. Vavra and Schaltegger 1999; Taylor *et al.* 2014; Blereau *et al.* 2016; Prent *et al.* 2020), cause U and Th loss (Williams *et al.* 2011) or Th gain (Harlov *et al.* 2011). Monazite is a common accessory mineral in metapelitic rocks experiencing low-amphibolite facies metamorphism (e.g. Rubatto 2002) to high-grade granulites, migmatites and charnockites (Fig. 8b; e.g. Laurent *et al.* 2018; Dev *et al.* 2021; Williams *et al.* 2022), whereas it is less common in *HP* rocks (Finger and Krenn 2007). Whilst geochronological disruption causes resetting of the oldest growth of the mineral, the reactivity of monazite is useful for tracing or determining the timing of fluid activity, reactivation of metamorphic processes and/or ore genesis. On the other hand, xenotime (Y, HREE)PO_4 is a HREE carrier, which also makes it a critical source of HREEs (Strzelecki *et al.* 2022). Xenotime occurs in metapelitic, granitic and carbonatitic rocks, and is less abundant in mafic and calc-silicate rocks (Spear and Pyle 2002). Recent phase equilibria modelling studies have demonstrated that xenotime usually occurs at pressures lower than 8 kbar and temperatures lower than 750°C (e.g. Shrestha *et al.* 2019). In contrast, monazite is found to be stable at higher pressures and temperatures, where water availability strongly controls the monazite *P–T* stability field and its preservation

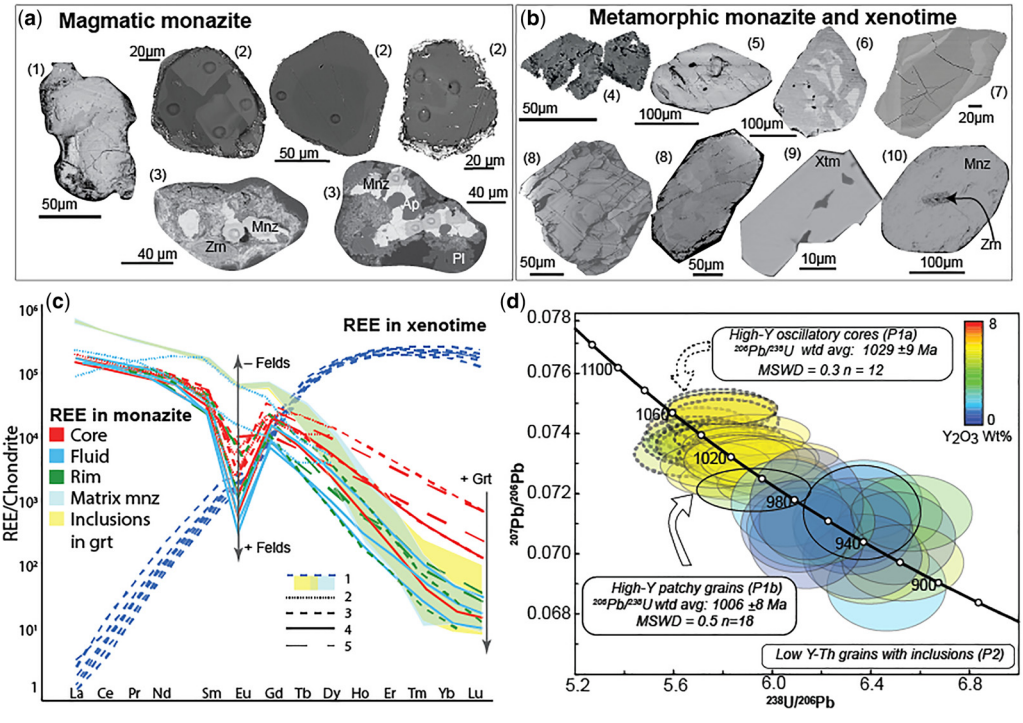

Fig. 8. (**a**) Magmatic textures of monazite crystals from (1) Barrote *et al.* (2020); (2) Volante *et al.* (2020*a*); (3) Piechocka *et al.* (2017). (**b**) Metamorphic textures of monazite and xenotime crystals: (4) Volante *et al.* (2020*c*); (5) Photo courtesy of Cutts; (6) Cutts *et al.* (2018); (7) Blereau *et al.* (2016); (8) Laurent *et al.* (2018); (9) Manzotti *et al.* (2018); (10) Barrote *et al.* (2020). (**c**) Representative chondrite normalized REE patterns for different types of monazite and xenotime: (1) Manzotti *et al.* (2018); (2) Rasmussen and Muhling (2007); (3) Rubatto *et al.* (2013); (4) Taylor *et al.* (2014); (5) Buick *et al.* (2010). (**d**) U–Pb data for monazite grains from sapphirine–cordierite UHT gneisses in Norway. Monazite ages are colour-coded based on Y_2O_3 content. Source: (d) after Laurent *et al.* (2018).

along the prograde path at much higher *P–T* conditions than previously envisaged (Larson *et al.* 2022).

Geochemical tools. Both monazite and xenotime are REE-rich mineral phases, containing a critical amount of REEs in addition to Y (Schulz 2021 and references therein). Monazite REE patterns are usually characterized by a negative slope, whereas xenotime commonly exhibits a positive REE pattern more like zircon (Fig. 8c). Sr-enrichment in monazite has been interpreted to reflect *HP* monazite growing in the absence of feldspars (Finger and Krenn 2007). Additionally, a REE signature like *HP* zircon, with low HREE and absence of a negative Eu anomaly, has been identified in monazite grains from the Kokchetav UHP rocks in Kazakhstan, and UHP rocks in Norway, suggesting this as a geochemical signature for HP monazite (Hermann and Rubatto 2014; Hacker *et al.* 2015). Furthermore, REEs in monazite have been utilized as geochemical discriminators with U–Pb geochronology to distinguish between magmatic and metamorphic monazite in complex deformed and metamorphosed terranes (e.g. Pe-Piper *et al.* 2014; Prent *et al.* 2019; Itano *et al.* 2020).

Like zircon, monazite has a number of partitioning relationships that can be useful in integrating various data sources to the evolution of a sample's mineral paragenesis, including monazite/melt (Yurimoto *et al.* 1990; Ward *et al.* 1992; Bea *et al.* 1994; Stepanov *et al.* 2012), monazite/xenotime (Andrehs and Heinrich 1998), monazite/K-feldspar (Villaseca *et al.* 2003) and monazite/garnet (Hermann and Rubatto 2003). The most applied technique is the partitioning of REEs between monazite and garnet since these minerals frequently occur together (e.g. Buick *et al.* 2006; Rubatto *et al.* 2006; Kylander-Clark *et al.* 2013; Mottram *et al.* 2014; Taylor *et al.* 2014; Blereau *et al.* 2016; Hagen-Peter *et al.* 2016; Hacker *et al.* 2019; Warren *et al.* 2019). Despite monazite being relatively poor in HREEs compared to zircon and garnet, the presence of garnet still impacts the relative concentration of HREEs in monazite. Monazite growing syn- to post-garnet or modified in the presence of garnet (see also Discussion) typically shows a reduction in HREEs and Y compared to monazite grown in the absence of garnet (Hermann and Rubatto 2003; Rubatto *et al.* 2006). Recent studies have demonstrated more complicated processes associated with HREE partitioning in monazite, where partitioning coefficients between monazite and garnet within investigated metapelitic rocks did not reproduce the expected values (e.g. Larson *et al.* 2019, 2022; Shrestha *et al.* 2019). Their temperature dependence is also found to be more relevant than initially envisaged (Hacker *et al.* 2019; Warren *et al.* 2019; Jiao *et al.* 2021). Also, recent work has highlighted by modelling Sm–Eu–Gd partitioning in suprasolidus systems that even though fractionation of Eu by feldspar growth can dominantly control the Eu budget, at equilibrium, other factors such as oxygen fugacity were shown to play an important role (Holder *et al.* 2020).

Geochronology. Monazite has proved a reliable geochronometer using the U–Pb system (Parrish 1990; Williams *et al.* 2007). Generally, monazite does not incorporate Pb into its crystal structure but has high Th (often several wt%) and U (several thousand ppm), meaning that it has low Pb_c and high radiogenic Pb. Monazite is also inferred to have a high *Tc* of up to 900°C (Fig. 1; Cherniak *et al.* 2004). However, monazite can be quite reactive (via CDR, see above), resulting in resetting of ages in fluid-dominated systems (Seydoux-Guillaume *et al.* 2002), whereas monazite in dry rocks (i.e. granulites) has been found to preserve detrital ages (e.g. Suzuki and Adachi 1994; Cutts *et al.* 2013; Guo *et al.* 2020). The high U and Th contents of monazite allow dating via chemical U–Th–Pb dating using EPMA (e.g. Suzuki and Adachi 1994; Montel *et al.* 1996, 2018). The advantages of this approach include *in situ*, non-destructive analysis and a small spot size allowing monazite grains <20 μm to be targeted (Ning *et al.* 2019; Williams and Jercinovic 2002). The main pitfall is that Pb_c correction is not possible (Williams *et al.* 2017), involving the assumption that the analysed grain is concordant and contains no Pb_c. The CHIME (chemical Th–U-total Pb isochron method) dating method is like chemical dating but targets multiple spots in an age domain to produce a 'pseudo-isochron'. This method also uses compositional criteria to determine if the monazite age is concordant, resulting in a more robust method than traditional chemical dating (Suzuki and Kato 2008). Improvements in EPMA sensitivity and the method make this a powerful technique moving forward (Konečný *et al.* 2018; Montel *et al.* 2018; Ning *et al.* 2019). Prior to EPMA dating, many studies utilized ID-TIMS geochronology of monazite (i.e. Smith and Barreiro 1990), and later the LA-ICP-MS approach (Machado and Gauthier 1996; Poitrasson *et al.* 2000). Due to its high U and Th contents, monazite is extremely amenable to LA-ICP-MS, where small spot sizes (8–12 μm) can be used. Similarly, geochronology of xenotime can be analysed *in situ* by both SIMS (Cross 2009; Fielding *et al.* 2017) and LA-ICP-MS (Lawley *et al.* 2015; Simpson *et al.* 2021) to collect texturally contextualized isotopic dates. Currently, no matrix-matched reference materials for xenotime are available as no homogeneous natural xenotime has been found. Therefore, first-order matrix corrections have been applied on xenotime reference materials such as z6413 (Stern and Rayner 2003) and MG-1

(Fletcher *et al.* 2004) for U–Pb geochronology, whereas glass NIST 610 is currently used as primary reference material for *in situ* Lu–Hf dating (Simpson *et al.* 2021). Due to the wealth of information provided by REE data, TEs are commonly collected either separately or simultaneously with geochronological data using one or two mass spectrometers (Holder *et al.* 2013; e.g. Kylander-Clark *et al.* 2013; Hacker *et al.* 2015; Volante *et al.* 2020*c*; Barrote *et al.* 2022*b*). Nanoscale geochronological analysis of monazite (Fougerouse *et al.* 2020, 2021) and xenotime (Joseph *et al.* 2021) via atom probe (ATP) is also possible. Analytical development has allowed to investigate diffusion and migration of atoms along monazite grain boundaries and/or crystal defects, and relates e.g. intracrystalline deformation with age resetting due to radiogenic Pb loss (Fougerouse *et al.* 2021). Great potential to determine ages by using the ATP was shown also on small xenotime crystals (Joseph *et al.* 2021). *In situ* studies allow monazite ages to be directly related to mineral textures present in the rock, so the age of deformation can be attributed to metamorphic events in complex terranes (e.g. Smith and Barreiro 1990; Foster *et al.* 2002; Štípská *et al.* 2015; Piechocka *et al.* 2017; Prent *et al.* 2019, 2020; Jiao *et al.* 2020*a*; Volante *et al.* 2020*c*).

Isotope geochemistry. In granitic rocks, high LREE minerals, like monazite, are great competitors for trace elements, including Sm–Nd and REE, in the host magmas (e.g. Fisher *et al.* 2017; Hammerli and Kemp 2021). The Sm–Nd isotope tracer system in monazite can complement the more commonly applied Lu–Hf system in zircon (e.g. Fisher *et al.* 2017; Martin *et al.* 2020; Mulder *et al.* 2021; Barrote *et al.* 2022*a*; Volante *et al.* 2022) and whole-rock Sm–Nd and/or Lu–Hf (e.g. Mark 2001; Hoffmann *et al.* 2011; Caxito *et al.* 2021), providing insights into the formation, evolution and differentiation of the continental crust (Hammerli and Kemp 2021). Significant contributions have been made to improve *in situ* Sm–Nd precision using LASS-MC-ICP-MS (e.g. Barrote *et al.* 2022*a*) to achieve a comparable level of precision to Lu–Hf in zircon (e.g. Fisher *et al.* 2011, 2020; Goudie *et al.* 2014; Spencer *et al.* 2020). Furthermore, monazite is less prone to weathering than other Sm–Nd-bearing major minerals (e.g. plagioclase), making it a valuable tool to investigate primary isotopic signatures (e.g. Barrote *et al.* 2022*a*).

Thermometry. To estimate minimum magmatic temperatures, monazite thermometry relies on whole-rock REE content in peraluminous and metaluminous granitic rocks (Montel 1993; Plank *et al.* 2009; Stepanov *et al.* 2012). While the Montel (1993) equation is calibrated only at low pressure, Stepanov *et al.* (2012) corrected it by extending experiments to higher pressures. Recent studies have presented the importance of applying variable H_2O contents for granitic rocks to determine monazite saturation temperatures, with this approach producing consistent zircon and monazite saturation temperatures across the same granitic samples (Volante *et al.* 2020*a*). The Y-HREE fractionation between monazite and xenotime results in an asymmetric miscibility gap in YPO_4-(REE)PO_4. This allows for the Y content of monazite to be used as a geothermometer, which is largely independent of pressure (e.g. Gratz and Heinrich 1997, 1998; Heinrich *et al.* 1997; Andrehs and Heinrich 1998). This thermometer can only be used when monazite has grown in the presence of xenotime. However, identifying and ascertaining that these two phases grew in equilibrium can be challenging (Pyle and Spear 1999). Like garnet, xenotime also preferentially incorporates HREE. Hence, xenotime is usually consumed during prograde metamorphism by garnet growth, and it commonly reappears during garnet breakdown at post-peak conditions or along the retrograde path (e.g. Hallett and Spear 2015). In this view, compositional variations in monazite (e.g. Regis *et al.* 2016; Manzotti *et al.* 2018) have been crucial to assess xenotime saturation within the rock system (e.g. Krenn and Finger 2010). For example, Y-rich monazite domains have been suggested to be plausible targets to use for thermometry (e.g. Viskupic and Hodges 2001; Krenn *et al.* 2012; Laurent *et al.* 2018). Y content can also be used to distinguish between different monazite age populations (i.e. Fig. 8d), and can be combined with thermometry to indicate the temperature–time evolution of the sample (e.g. Laurent *et al.* 2018). Some attempts were made to thermodynamically model monazite and xenotime (e.g. Kelsey *et al.* 2007, 2008; Spear and Pyle 2010; Shrestha *et al.* 2019). However, this approach only works with low-Ca bulk-rock compositions and requires the simplification of a complicated system.

Apatite

Apatite $Ca_5(PO_4)_3(F,Cl,OH)$ is a calcium phosphate (Fig. 2s-u; Fig. 9) that is often present as an accessory mineral in several rock types, including various igneous rocks (ultramafic–felsic) to metamorphic and sedimentary, and even in meteorites (e.g. Harlov 2015; McCubbin and Jones 2015; Webster and Piccoli 2015). Apatite can readily incorporate large amounts of TE (e.g. U, Th, REE, Y, Sr), which replace Ca in the crystal lattice with charge compensation mechanisms (Engi 2017), making apatite important for the trace element budget of a rock. In addition, apatite commonly contains significant amounts of water and/or halogens and volatile

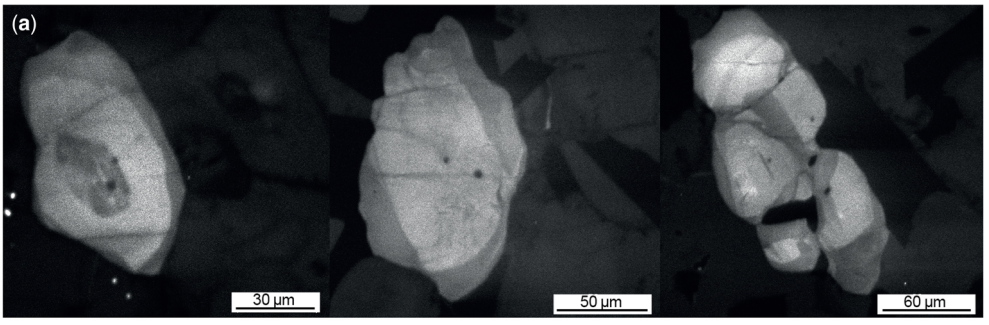
(a)
30 µm
50 µm
60 µm

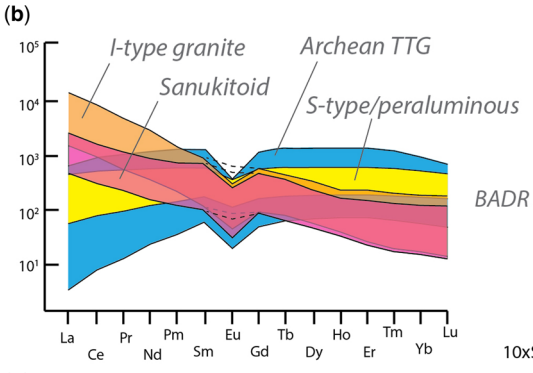
(b)
I-type granite
Archean TTG
Sanukitoid
S-type/peraluminous
La
Ce
Pr
Nd
Pm
Sm
Eu
Gd
Tb
Dy
Ho
Er
Tm
Yb
Lu

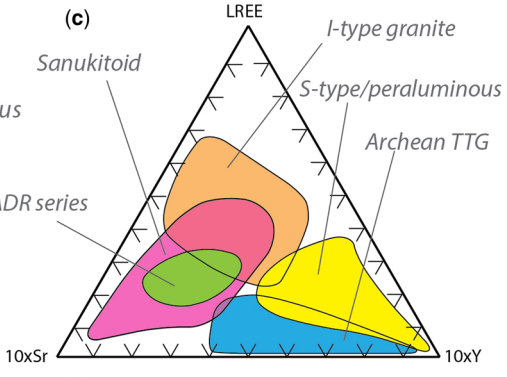
(c)
LREE
I-type granite
Sanukitoid
S-type/peraluminous
Archean TTG
BADR series
10xSr
10xY

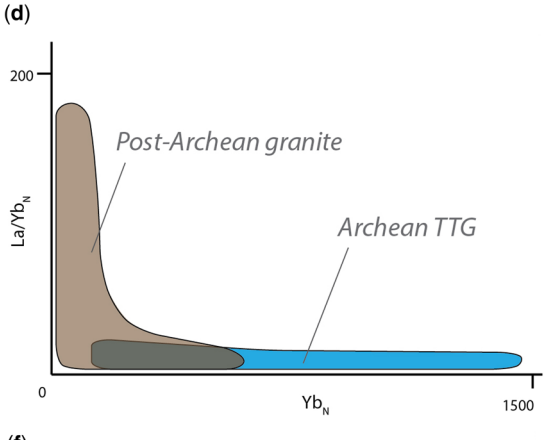
(d)
Post-Archean granite
Archean TTG
La/Yb_N
Yb_N
0
1500

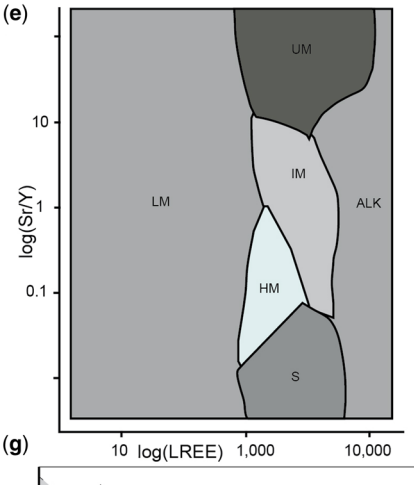
(e)
UM
IM
LM
ALK
HM
S
log(Sr/Y)
log(LREE)
10
1,000
10,000

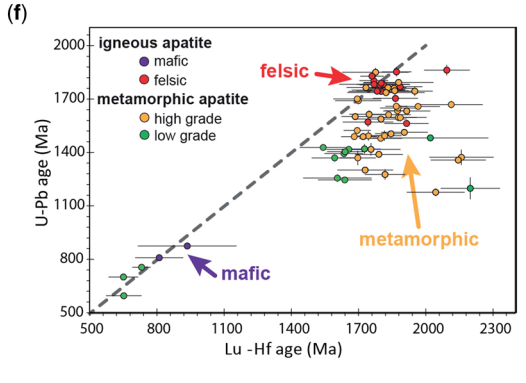
(f)
igneous apatite
mafic
felsic
metamorphic apatite
high grade
low grade
felsic
metamorphic
mafic
U-Pb age (Ma)
Lu -Hf age (Ma)

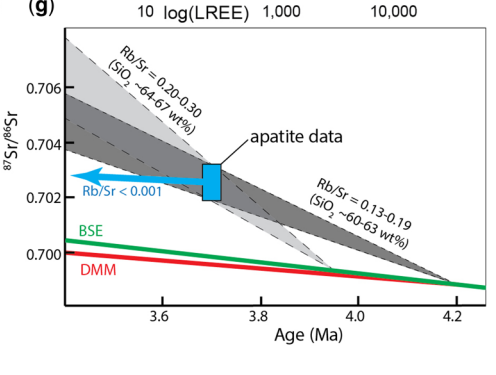
(g)
Rb/Sr = 0.20-0.30
(SiO2 ~64-67 wt%)
apatite data
Rb/Sr < 0.001
Rb/Sr = 0.13-0.19
(SiO2 ~60-63 wt%)
BSE
DMM
87Sr/86Sr
Age (Ma)

species (e.g. F and Cl; Harrison and Watson 1984; Piccoli and Candela 2002), and records the evolution of metasomatic and hydrothermal fluids (e.g. Harlov 2015; Lin *et al.* 2023). Combined, the geochemical characteristics of apatite make it suitable for many geochemical and petrological applications, with measurements being possible with a large variety of instruments (e.g. SIMS, (LA)-ICP-MS, (LA)-MC-ICP-MS, EPMA), imaging with BSE (Fig. 9a) and TE mapping with LA-ICP-MS (Fig. 2r). Depending on its crystallization conditions, apatite can exhibit various textures visible in CL or BSE images (e.g. Mühlberg *et al.* 2021) and geochemical signatures that make this mineral a very interesting proxy for rock formation and evolution as well as for chronological information (Chew *et al.* 2011; Hammerli *et al.* 2014; Kirkland *et al.* 2017; Antoine *et al.* 2020; Fisher *et al.* 2020; Prent *et al.* 2020; Paul *et al.* 2021).

Geochemical tools. Igneous apatite has reasonably similar total REE contents regardless of the protolith lithology (e.g. Chu *et al.* 2009), except for apatite in alkali-rich rocks, which are commonly significantly REE-rich (e.g. Zirner *et al.* 2015). However, relative REE concentrations, and Y and Sr, are variable within different rock-types and particularly effective for discriminating magma types (e.g. Bea 1996; Belousova *et al.* 2001; Bruand *et al.* 2020). Negative Eu anomalies are present in apatite from most igneous rocks except ultramafics (e.g. Chakhmouradian *et al.* 2017; Bruand *et al.* 2020), and the magnitude of Eu anomalies is typically positively correlated with SiO_2 content. In contrast, Sr content in apatite is negatively correlated with SiO_2 content, with the highest Sr contents being observed in ultramafic rocks (Ihlen *et al.* 2014) and the lowest Sr contents in felsic rocks (Sha and Chappell 1999). Also, Sr in apatite strongly correlates with Sr content in the corresponding whole-rock (Belousova *et al.* 2001; Jennings *et al.* 2011; Bruand *et al.* 2014). Variations in Sr content in TTGs are interpreted to directly correlate with the melting depth of the TTGs' source, where a deep source is in equilibrium with garnet and rutile, but no plagioclase (Moyen and Martin 2012). Moreover, apatite chemistry can be used as a tracer of different magmatic petrogenetic processes, reflecting geodynamic changes during crustal evolution (Bruand *et al.* 2020) such as $(La/Yb)_N$ v. Yb_N discrimination diagram for TTGs (Antoine *et al.* 2020; Fig. 9b–d).

Metamorphic apatite also exhibits contrasting signatures depending on its metamorphic grade and its textural context (e.g. O'Sullivan and Chew 2020; Prent *et al.* 2020). Total REE content increases with the metamorphic grade (e.g. El Korh *et al.* 2009), such that in high-grade rocks it is indistinguishable from that of igneous apatite (e.g. Bingen *et al.* 1996). In addition, negative Eu anomalies characterize apatite growing in low-grade metamorphic rocks (Henrichs *et al.* 2018). Also, metamorphic apatite contains higher Sr concentrations in greenschist- and blueschist-facies rocks (e.g. Nishizawa *et al.* 2005), and lower ones in migmatites and granulite-facies rocks (e.g. Nutman 2007). In felsic igneous and metamorphic rocks, apatite $(La/Lu)_N$ ratio is commonly ≤ 1, whereas in all other rocks $(La/Lu)_N$ ratio is >1, with the highest values recorded in ultramafic rocks (e.g. O'Reilly and Griffin 2000). A discrimination diagram using Sr/Y v. ΣLREE biplots from various igneous and metamorphic/metasomatic rocks (Fig. 9e) can be used to statistically categorize source lithologies (O'Sullivan *et al.* 2020). Additional discriminant diagrams based on the enrichment in LREEs and MREEs, Eu anomalies, the tetrad effect, Mn and Sr contents, total REEs and Y in apatite can be used to highlight the variability between different types of mineralization (Decrée *et al.* 2023). For example, bell-shaped REE patterns defined by MREE enrichment and positive Eu anomalies were found to be a unique indicator of hydrothermal apatite formed in a mineralized, reducing hydrothermal system (e.g. Krneta *et al.* 2018; Lin *et al.* 2023).

Geochronology. Apatite has long been the target for geochronological studies (e.g. Schoene and Bowring 2007; Chew *et al.* 2011; Glorie *et al.* 2022) either using the U–Th–Pb or Lu–Hf isotope system (e.g. Barfod *et al.* 2005; Chew *et al.* 2011; Simpson *et al.* 2021; Glorie *et al.* 2023), or Sm–Nd (Fisher *et al.* 2020). Apatite commonly incorporates

Fig. 9. (**a**) BSE images for magmatic apatite. (**b**) Distinct REE patterns for apatite from different types of granitoids. (**c**) Discrimination diagram for apatite from various granitoids. BADR, basalt–andesite–dacite–rhyolite series. (**d**) Chondrite-normalized La/Yb_N v. Yb_N diagram of apatite from post-Archean granites and Archean TTGs. (**e**) Lithological discrimination diagram. Abbreviations: ALK, alkali-rich igneous rocks; IM, mafic I-type granitoids and mafic igneous rocks; LM, low- and medium-grade metamorphic and metasomatic; HM, partial-melts/leucosomes/high-grade metamorphic; S, S-type granitoids and high aluminum saturation index (ASI) 'felsic' I-types; UM, ultramafic rocks including carbonatites, lherzolites and pyroxenites. (**f**) Binary diagram U–Pb v. Lu–Hf ages (Ma) in apatite. (**g**) $^{87}Sr/^{86}Sr$ v. age diagram showing how initial apatite Sr isotope signatures can be interpreted in terms of source lithology, derived from time-integrated Rb/Sr ratios, and resulting model age (intersection between grey fans and BSE evolution). Depleted MORB (Mid-ocean ridge basalt) mantle (DMM). Source: (b) and (c) modified after Bruand *et al.* (2020); (d) modified after Antoine *et al.* (2020); (e) modified after O'Sullivan *et al.* (2020); (f) rock lithologies following discrimination diagram from O'Sullivan *et al.* (2020); (g) modified after Emo *et al.* (2018).

significant amounts of Pb_c that vary from limited amounts in igneous apatite to larger amounts in hydrothermal apatite crystals (e.g. Kirkland *et al.* 2017). Low-grade metamorphic apatite typically provides poor precision for U–Pb dating due to low U concentrations (<5 ppm) and high initial Pb_c contents, while apatite from igneous rocks is typically U-rich (>20 ppm) and has lower Pb_c, leading to more precise U–Pb ages (e.g. Henrichs *et al.* 2018, 2019; O'Sullivan *et al.* 2018). Because of its Pb_c content, apatite can often produce U–Pb dates that are strongly discordant (also see Titanite section). This Pb_c presents a particular challenge for young samples that have had little time to accumulate substantial radiogenic Pb (Pb*), or for apatite grains with low concentrations of U. Following to the development of apatite U–Th–Pb age reference materials (e.g. Chew *et al.* 2011; Thomson *et al.* 2012; Apen *et al.* 2022; Lana *et al.* 2022) and data reduction schemes employing ^{208}Pb-, ^{207}Pb- or ^{204}Pb-based Pb_c corrections to age reference materials and unknowns, it is now possible to routinely date apatite both precisely and accurately (e.g. Andersson *et al.* 2008, 2022; Chew *et al.* 2011; Thomson *et al.* 2012; Antoine *et al.* 2020; Prent *et al.* 2020; Glorie *et al.* 2022). However, some complications in data interpretation can occur in apatite crystals that have undergone metamorphism due to diffusion effects (e.g. Paul *et al.* 2019). Apatite U–Pb dates may be reset by deformation and fluids, causing the age to represent the last major deformation event or latest dissolution–precipitation and/or chemical exchange (Odlum *et al.* 2022).

Recent advances including the development of LA-ICP-MS/MS technology allowed resolution of isobaric interferences for Lu–Hf *in situ* dating of apatite crystals (e.g. Barfod *et al.* 2003, 2005; Larsson and Söderlund 2005; Simpson *et al.* 2021; Gillespie *et al.* 2022; Glorie *et al.* 2022, this volume, in press) and Sm–Nd (e.g. Hammerli *et al.* 2014, 2019; Doucelance *et al.* 2020; Fisher *et al.* 2020), which is extremely useful to investigate post-metamorphic cooling history and/or compare crystallization ages. Apatite is commonly combined with other mineral phases that exhibit various parent/daughter ratios (i.e. Lu/Hf and Sm/Nd) to obtain a more robust isotope isochron (e.g. Hammerli *et al.* 2014; Laurent *et al.* 2017; Simpson *et al.* 2021). Advantages of the Lu–Hf isotope system in apatite over U–Pb include higher *Tc* of the former (Fig. 1), resulting in an age closer to the apatite crystallization age (e.g. Henrichs *et al.* 2019). Comparisons of the two systems can have significant advantages (Fig. 9f; Glorie *et al.* 2022).

Isotope geochemistry. The Sm–Nd isotope system in apatite can provide insights into timing and source of apatite host-rock (e.g. Fisher *et al.* 2020). Among stable isotopes, oxygen isotopes appear to be proxies for magma sources and to record fluid circulation and metamorphism processes (e.g. Bruand *et al.* 2019). Chlorine and hydrogen isotopes have also been used as proxies for volatilization/condensation processes (e.g. Potts *et al.* 2018; Wudarska *et al.* 2020). Isotope systematics such as ^{87}Rb–^{87}Sr can be measured using either (LA-)MC-ICP-MS or LA-ICP-MS/MS, TIMS or SIMS, and coupled to age information (Fig. 9g; Emo *et al.* 2018; Ravindran *et al.* 2020; Gillespie *et al.* 2021). The ^{87}Sr/^{86}Sr ratio of apatite may be used together with K-rich or Rb-bearing minerals such as micas for *in situ* Rb–Sr geochronology to create a combined isochron (Olierook *et al.* 2020).

Thermometry. There is no currently developed thermometer for apatite like those for zircon (Ti-in-zircon) or rutile (Zr-in-rutile), but the U–Pb *Tc* (350–570°C; Fig. 1) can be used as an indirect proxy for tracking metamorphic or magmatic cooling in combination with other chronometers in apatite (Fig. 1; e.g. Cherniak 2000*b*; Barfod *et al.* 2003, 2005; Cochrane *et al.* 2014; Chew and Spikings 2015; Kirkland *et al.* 2018; Ferreira *et al.* 2022).

Discussion

Applications of multi-mineral petrochronometers to metamorphic processes

Interplay between garnet–zircon–monazite–xenotime. Geochronological and geochemical data retrieved from metamorphic accessory minerals are commonly integrated with information from the major mineral paragenesis, *P–T* constraints from phase equilibrium diagram calculations and microstructures. Figure 10 reflects an example of two synoptic, theoretical *P–T–t* evolutions where petrochronological information of metamorphic accessory minerals such as monazite, zircon and garnet is linked to *P–T* information. The first *P–T* path (Fig. 10a) represents common clockwise granulite-facies metamorphism of a pelitic protolith hosting inherited zircon (Fig. 10a, i). During prograde metamorphism, garnet growth begins and inherited zircon grains start to recrystallize with increasing temperatures (Fig. 10a ii). This prograde part of the metamorphic evolution is often difficult to accurately constrain due to open-system processes, overprinting and/or exceeding closure temperatures of earlier phases. Zircon has been shown to grow along the prograde path connected to the movement of locally-derived melts (e.g. Harley and Nandakumar 2014; Harley 2016; Weinberg *et al.* 2020) as well as injected, externally-derived melts (Andersson *et al.* 2002; Flowerdew *et al.* 2006; Wu *et al.* 2007).

Once the sample crosses the solidus, partial melting begins. Inherited zircons may be consumed and or dissolved in the melt that becomes enriched in zirconium (Watson and Harrison 1984; Boehnke *et al.* 2013; Gervasoni *et al.* 2016), forming embayment and relict core textures in zircon. Monazite might also grow along the prograde and retrograde path (e.g. Rubatto 2002; Shrestha *et al.* 2019; Larson *et al.* 2022), but also during (Kelsey *et al.* 2008; Rubatto *et al.* 2009; Larson *et al.* 2022) and/or just after max T conditions are reached (Fig. 10a iii, v, vii; Clark *et al.* 2014; Shrestha *et al.* 2019), making it a more suitable time-capsule than zircon by preserving a greater *P–T–t* window at subsolidus conditions (e.g. Ambrose *et al.* 2015; Mottram *et al.* 2015; Hacker *et al.* 2019; Shrestha *et al.* 2020; Larson *et al.* 2022). Recent works modelled the *P–T* stability fields for monazite and xenotime, with monazite present during prograde growth of garnet, max T(/P) conditions and along the retrograde path during garnet breakdown at both sub- and suprasolidus conditions (Shrestha *et al.* 2019). In contrast, xenotime appears only at low *P–T* conditions during the early stages of the prograde path and/or along the retrograde path, when it would start to assimilate most of the Y and HREE, resulting in a decrease in monazite proportions (Shrestha *et al.* 2019). Prograde garnet sees further growth at suprasolidus conditions, combined with an additional generation of peritectic garnet (Fig. 10a iv) that could be distinguished based on different REE patterns and inclusions (Fig. 3f). Trace element partitioning is mostly utilized for max T(/P) to retrograde portion of the *P–T–t* history as this information is most likely preserved. For example, Figure 10a shows that garnet growth and metamorphic 'soccer ball' zircon (e.g. Vavra and Schaltegger 1999; Blereau *et al.* 2016; Taylor *et al.* 2016) grow in the same geochemical system and have a near 1:1 partitioning of M-HREE. How well these partitioning relationships are preserved depends on the conditions of metamorphism and how these affect the equilibration volume of the sample. Typically, this is largest at max T conditions, where rates of diffusion and potential fluids and/or melt increase. Approaching the solidus on the retrograde path, Zr-bearing phases may breakdown, e.g. garnet to cordierite (Fig. 10a vi) resulting in additional zircon growth (e.g. Fraser *et al.* 1997; Degeling *et al.* 2001; Wu *et al.* 2007; Kelsey *et al.* 2008), from rims to completely new grains (Fig. 10a vii). A subsequent fluid event, e.g. upon crystallization of local melt, can modify monazite and zircon textures, perturbing age and geochemical data (Poitrasson *et al.* 2000; Seydoux-Guillaume *et al.* 2012; Kröner *et al.* 2014; Taylor *et al.* 2014; Blereau *et al.* 2016; Prent *et al.* 2019). In more complex garnet textures, such as the unusual atoll garnet (e.g. Jonnalagadda *et al.* 2017; Kulhánek *et al.* 2021; Godet *et al.* 2022; Massonne and Li 2022), TE content recorded by subsequent growth of concentric garnet rings can also provide useful information about the interchange of TE within the system due to growth and breakdown of other accessory phases (Godet *et al.* 2022). For example, by using LA-ICP-MS trace element mapping, Godet *et al.* (2022) reported enrichment in V and Ti in the garnet inner rim compared to the core, which was attributed to rutile breakdown, whereas Cr, Y, LREE and MREE enrichment in the outer rim was interpreted to reflect allanite and monazite breakdown.

The second *P–T–t* evolution (Fig. 10b) represents a more residual scenario, where the protolith has already been partially melted. In this case, recrystallization and preservation of existing major and accessory minerals are promoted due to the lack and/or reduction in volume of partial melt being produced, which also limits the generation of new assemblages (Fig. 10b, i, ii, iii; Bea and Montero 1999; White and Powell 2002). Monazite and zircon contrast in their behaviour under these conditions. Monazite may grow in larger amounts than zircon, despite being in a melt poor environment, due to higher reactivity (e.g. Högdahl *et al.* 2012; Rubatto *et al.* 2013; Morrissey *et al.* 2016), potentially recording information completely missed by zircon. As in the first scenario (Fig. 10a), relict garnet breaks down during decompression to an intergrowth of plagioclase + orthopyroxene, another micro zircon permitting reaction (Fig. 10b). Local hydration or different amounts of melt loss (Morrissey *et al.* 2016; Larson *et al.* 2022) is reflected by a second *P–T* event (Fig. 10b, v, vi, vii) recorded only by more reactive high-strain microsites. The interpretation of geochronological data obtained from studies of high-grade metamorphic rocks can also be extremely challenging as most terranes record a spread of ages rather than statistical populations (e.g. Whitehouse and Kemp 2010; Farias *et al.* 2020; Taylor *et al.* 2020; Finch *et al.* 2021; Gutieva *et al.* 2021; Mulder and Cawood 2021; Salminen *et al.* 2022; Whitehouse *et al.* 2022). For example, in Figure 10c, the younger age population could represent either a single prolonged metamorphic event or potentially two events, with the second modifying the first and many other possible combinations. Determining the correct age interpretation depends on mineral textures, where the analyses and sample come together with complementary geochemical and isotopic information.

Interplay between allanite–monazite–xenotime–apatite–(titanite–rutile). Metamorphic reactions between REE-rich phases such as allanite–monazite–xenotime–apatite are illustrated with those of titanite–rutile on the same theoretical *P–T–t–(d)* path, though these sets of minerals may occur in

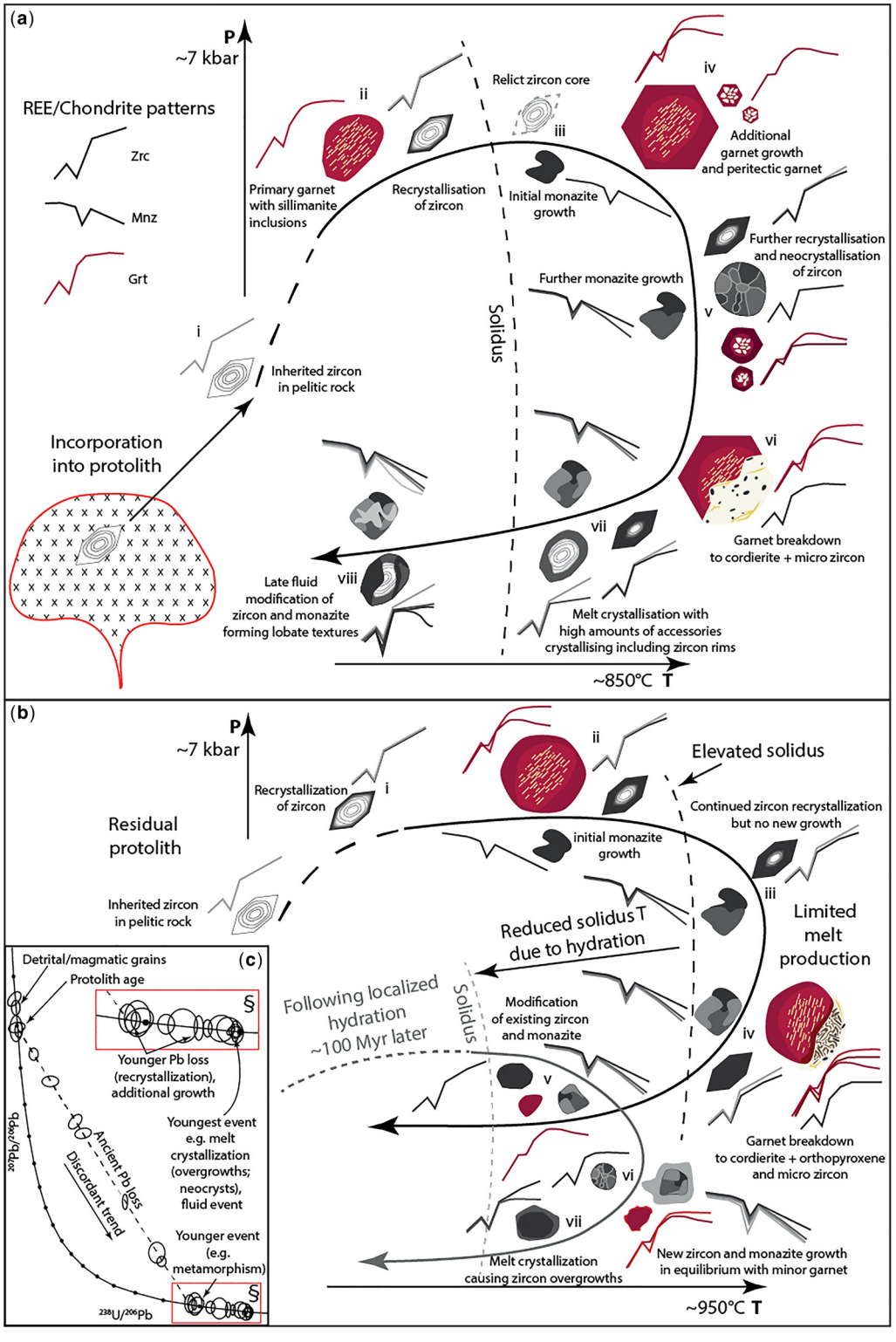
(a)
P
~7 kbar
REE/Chondrite patterns
Zrc
Mnz
Grt
Incorporation into protolith
i
Inherited zircon in pelitic rock
ii
Primary garnet with sillimanite inclusions
Relict zircon core
iii
Recrystallisation of zircon
Initial monazite growth
Solidus
Further monazite growth
iv
Additional garnet growth and peritectic garnet
Further recrystallisation and neocrystallisation of zircon
v
vi
Garnet breakdown to cordierite + micro zircon
vii
viii
Late fluid modification of zircon and monazite forming lobate textures
Melt crystallisation with high amounts of accessories crystallising including zircon rims
~850°C T
(b)
P
~7 kbar
Residual protolith
Recrystallization of zircon
i
Inherited zircon in pelitic rock
ii
Elevated solidus
Continued zircon recrystallization but no new growth
initial monazite growth
iii
Limited melt production
Reduced solidus T due to hydration
Following localized hydration ~100 Myr later
Solidus
Modification of existing zircon and monazite
iv
v
Garnet breakdown to cordierite + orthopyroxene and micro zircon
vi
vii
Melt crystallization causing zircon overgrowths
New zircon and monazite growth in equilibrium with minor garnet
~950°C T
(c)
Detrital/magmatic grains
Protolith age
§
Younger Pb loss (recrystallization), additional growth
Youngest event e.g. melt crystallization (overgrowths; neocrysts), fluid event
Ancient Pb loss
Discordant trend
Younger event (e.g. metamorphism)
§
207Pb/206Pb
238U/206Pb

different chemical systems (Fig. 11). The timing and sequence of metamorphic reactions (i.e. growth of accessory phases) depend not only on the variation of pressure and temperature conditions, including the residence time of a volume of rock at certain conditions, but also on the bulk-rock composition of the protolith and on strain rate, which strongly influence the reaction sequence during fluid–rock interaction at different crustal levels. Reconstructing the formation and breakdown of these minerals and growth of other major and minor phases in the rock usually requires a detailed petrographic investigation that includes X-ray compositional maps and analysis of Y and REE partitioning between the phases (e.g. Janots *et al.* 2008; Garber *et al.* 2017; Manzotti *et al.* 2018; Airaghi *et al.* 2019). Additionally, tools such as TE mapping by LA-ICP-MS (e.g. Raimondo *et al.* 2017; Chew *et al.* 2021; Sliwinski and Stoll 2021; Godet *et al.* 2022) allow for greater precision in determining chemical composition effects on growth or break-down of minerals associated with different *P–T* conditions and fluid-present or absent processes.

During the prograde evolution of a time capsule mineral such as garnet, key inclusions can be incorporated and provide insights regarding the *P* and *T* conditions a rock volume experienced during the early stages of the evolution path (Fig. 11). For example, identification of rutile inclusions in garnet core (Fig. 11) and prograde allanite can indicate that rutile grew during the prograde stages towards max *P* conditions (Boston *et al.* 2017). In this case, prograde growth of garnet sequestered most of the Mn and HREE, resulting in allanite cores with a relatively HREE-depleted pattern in relation to the rim. Manzotti *et al.* (2018) investigated rocks in which Y-rich garnet cores enclosed a first generation of rutile and allanite inclusions, whereas Y-poor garnet rims included monazite grains that crystallized aligned parallel to the matrix foliation (Fig. 11). At this stage, monazite may form after breakdown of allanite or other phosphates such as apatite and/or xenotime (Engi 2017; Manzotti *et al.* 2018), recording peak pressure conditions (e.g. Boston *et al.* 2017; Manzotti *et al.* 2018; Volante *et al.* 2020*c*; Barrote *et al.* 2022*b*; Fumes *et al.* 2022). Monazite REE patterns may exhibit low Y content together with a steeply negative HREE slope, suggesting that garnet was still stable during monazite growth, whereas pronounced negative Eu anomalies commonly suggest plagioclase stability or oxygen fugacity variations (Fig. 11; e.g. Boston *et al.* 2017; Holder *et al.* 2020). At low- to medium-metamorphic grade, allanite and monazite may replace each other, and this process depends on different factors including bulk-rock (e.g. Wing *et al.* 2003; Janots *et al.* 2008; Spear 2010) and fluid (Budzyń *et al.* 2010) compositions, as well as oxygen fugacity (Janots *et al.* 2011) and pressure and temperature conditions (Janots *et al.* 2007). Post-metamorphic pressure peak, along the lower-pressure, possibly higher-temperature path, a second generation of allanite and apatite can form at the expenses of monazite grains commonly exhibiting complex coronitic dissolution textures (Fig. 11; e.g. Manzotti *et al.* 2018). At this stage, in mafic and Ca-rich systems, titanite crystals may grow as a replacement product of rutile, whereas ilmenite would grow in a Ca-poor system and at lower pressures. During retrograde, low-grade hydrothermal metamorphism in pelitic systems, new xenotime and monazite may crystallize following allanite, apatite, residual monazite relicts and garnet breakdown, with xenotime associated with chlorite and minor biotite aggregates replacing garnet porphyroblasts (Fig. 11; Manzotti *et al.* 2018). Most of the Y released by garnet would be incorporated by xenotime and monazite in minor amounts. New rutile crystals may grow during the retrograde cooling stage at the expense of titanite and as rutile exsolution, growing parallel to biotite cleavage during its replacement by chlorite (Fig. 11). During this late hydrothermal stage, rutile may grow with apatite and record the cooling stages (e.g. Apen *et al.* 2020).

Applications of multi-mineral petrochronometers to magmatic processes

In this section, we emphasize that a combined multi-mineral approach is a powerful tool to provide

Fig. 10. Synoptic *P–T* evolutions of a metapelite in different hypothetical scenarios with associated types of zircon, monazite, xenotime, garnet growth/breakdown textures and potential REE patterns. (**a**) Singular clockwise *P–T* evolution: (i) inherited zircon; (ii) primary garnet and recrystallization of inherited zircon; (iii) relict zircon core, initial monazite growth; (iv) growth of garnet rim and peritectic garnet; (v) neocrystallized 'soccer ball' zircon, additional monazite and recrystallization of zircon; (vi) garnet breakdown; (vii) melt crystallization; (viii) late fluid modification. (**b**) A residual protolith along a clockwise polymetamorphic *P–T* path: (i) recrystallization of zircon; (ii) prograde monazite growth in the presence of relict garnet; (iii) at the elevated solidus, minor melting causes additional monazite but no new zircon growth; (iv) garnet breakdown, final monazite growth and complete 'ghost zoning' to recrystallized zircon. After a localized hydrous retrograde event, the hydrated areas follow a secondary *P–T* path; (v) melt modifies zircon and monazite to relict cores stable with relict garnet grains; (vi) new zircon and monazite; (vii) final melt crystallization. (**c**) Synthetic Tera–Wasserburg plot with interpretation based on the nature of analysed textures; § enlarged inset of younger ages. Source: (a–c) modified after Blereau (2017).

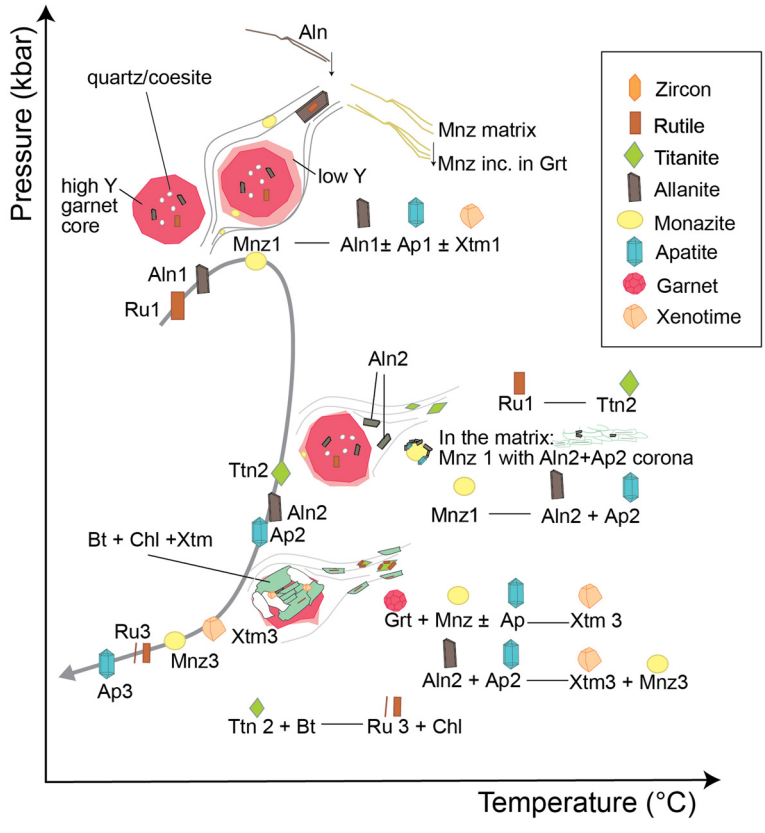

Fig. 11. Synoptic *P–T* evolution diagram including reactions of key petrochronometers such as garnet, allanite, monazite, rutile, apatite, xenotime and titanite. Source: modified after Manzotti *et al.* (2018) including key mineral reactions from Boston *et al.* (2017); Fumes *et al.* (2022); Manzotti *et al.* (2022).

constraints on magma sources (e.g. mineralogy, composition), differentiation processes (e.g. mixing, fractional crystallization) and timing of magma formation and crystallization. The first scenario corresponds to simple fractional crystallization of a single magma batch (Fig. 12). The second is a more complex scenario wherein magma is contaminated by a distinct lithology and/or mingles with a different magma. The third scenario refers to Precambrian gneisses, wherein the objective is to recover the initial magmatic signatures despite the occurrence of a metamorphic overprinting event.

To constrain the crystallization age of a magmatic rock, zircon is arguably the easiest mineral to date among those presented here but it is not necessarily observed in all rock types. Consequently, the timing of igneous rock formation can be addressed using other phases such as titanite, rutile, monazite, apatite or allanite, provided that they record a magmatic age or fast cooling. In a scenario where a magmatic intrusion does not experience post-crystallization disturbance and contains most mineral phases presented in this contribution, multi-mineral dating becomes useful as these phases likely record different ages reflecting the magma cooling history (Fig. 12; e.g. Schaltegger *et al.* 2009; Jayananda *et al.* 2015). A potential issue is the precision on determined ages, as granite batholiths can cool over relatively short timescales (e.g. Coleman *et al.* 2004; Schaltegger *et al.* 2009; Barboni *et al.* 2013). In the same scenario, Lu–Hf in zircon/apatite, Sm–Nd in monazite/titanite/apatite and Rb–Sr in apatite, combined, allow these source tracing radiogenic isotope systems to be directly compared, and coupled to geochronological data (i.e. U–Th–Pb and Lu–Hf in apatite, and Sm–Nd in monazite/titanite/apatite). Also, comparisons of these isotopic systems at the whole-rock and mineral scale can help constrain source composition or detect small discrepancies that may be important for understanding rock formation (e.g. Guitreau *et al.* 2012; Fisher *et al.* 2020; Barrote *et al.* 2022*a*; Volante *et al.* 2022; Zhang *et al.* 2022).

The second scenario includes a magmatic body that experienced mingling, mixing or contamination.

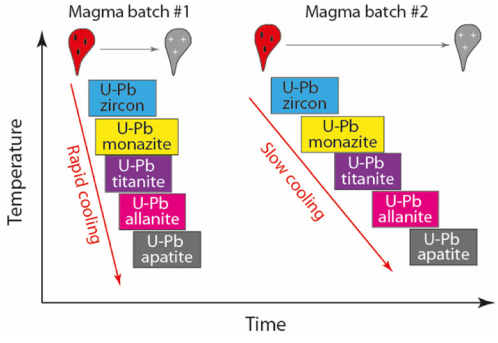

Fig. 12. Hypothetical temperature–time paths for two distinct intrusions with one having cooled rapidly and the other one slowly. Note that closure temperatures do not overlap between techniques and minerals for illustrative purposes only. Also, cooling paths are presented as straight lines which may not accurately depict actual cooling paths.

Radiogenic systems allow end-members to be identified due to specific sensitivity to contamination, source characteristics and respective elemental concentrations. For example, Laurent *et al.* (2017) used Rb–Sr and Sm–Nd in apatite and titanite, respectively, from hybrid granitoids to show that these minerals did not crystallize at the same time and that while apatite formed in both magmas before mingling and after mingling (zonation), titanite crystallized only in the mingled magma. To identify end-member isotopic compositions, another geochemical study investigated zircon, apatite and titanite, which revealed mingling of mantle and crust-derived magmas (Sun *et al.* 2010). If one of the end-members is crustal derived, zircon xenocrysts can provide further information about crustal diversity (e.g. Villaros *et al.* 2012; Bea *et al.* 2021). Also, monazite can inherit Nd isotope heterogeneities from the source while losing the original U–Pb crystallization age (Fisher *et al.* 2017). Trace element patterns and ratios can provide further insights into magma evolution after and/or before mixing/mingling (e.g. Sun *et al.* 2010; Laurent *et al.* 2017). Melt and/or mineral inclusions in accessory minerals can also provide information about the melt source composition (e.g. Bruand *et al.* 2017; Antoine *et al.* 2020; Ferrero *et al.* 2021).

The third scenario considers Precambrian rocks, which often experienced polyphase histories that involved at least one metamorphic episode potentially compromising one or more isotope systems (e.g. Black 1988; Hammerli *et al.* 2014; Emo *et al.* 2018; Guitreau *et al.* 2018; Antoine *et al.* 2020; Fisher *et al.* 2020; Hammerli and Kemp 2021). For example, *in situ* Sm–Nd investigation of apatite, allanite, titanite, xenotime and monazite in Precambrian metasedimentary rocks revealed re-equilibration of heterogeneous Nd isotope signature in apatite over 550°C, after which it retains its Nd isotope signature throughout anatexis (Hammerli *et al.* 2014). While titanite and allanite equilibrate at LT (350–400°C), REE-rich accessory phases exhibit homogeneous Nd isotopic signatures at HT (600°C) and behave as open systems during partial melting and anatexis (Hammerli *et al.* 2014).

Perspectives: unconventional analytical techniques. Where to?

From the conceptualization of petrochronology (as summarized in Engi *et al.* 2017; Kohn *et al.* 2017), significant analytical improvements have occurred in the field of geoscience and have been applied to all key mineral phases that are described in this review. New analytical methods have been developed (e.g. atom probe dating, Fougerouse *et al.* 2021; *in situ* Lu–Hf dating using LA-ICP-MS/MS, Simpson *et al.* 2021, 2022, 2023), previous analytical methods have been continuously updated and improved (e.g. *in situ* EPMA dating, Montel *et al.* 2018; *in situ* U–Pb dating, Millonig *et al.* 2020), new and updated numerical tools for quantitative petrology have been developed and enhanced, including imaging and modelling tools (e.g. XMapTools, Lanari *et al.* 2014, 2019; Q–XRMA, Ortolano *et al.* 2018, Zucali *et al.* 2021; Bingo-Antidote, Duesterhoeft and Lanari 2020) as well as the use of TE maps (e.g. Raimondo *et al.* 2017; George *et al.* 2018; Lanari and Piccoli 2020; Rubatto *et al.* 2020; Gaidies *et al.* 2021), and new boundaries have been pushed to investigate melting mechanisms (e.g. Ferrero *et al.* 2021). In this section, we briefly discuss the exciting and bright future in front of the discipline of petrochronology that has only started to push analytical advances to the limit of conventional methods, allowing for a better understanding of plate- to nanoscale crustal processes.

Garnet is the ultimate petrochronometer (Baxter *et al.* 2017), with the most exciting advance being the development of *in situ* Lu–Hf geochronology (Simpson *et al.* 2021). The use of inclusions as proxies for whole-rock isotopic composition also means that this method may be suitable for detrital garnet studies (Maneiro *et al.* 2019; Mark *et al.* 2022). Future work should focus on enhancing accuracy and precision of Lu–Hf and U–Pb measurement in secondary reference material e.g. Aysal *et al.* 2023 and finding primary reference material (i.e. isotopically homogeneous) for common Hf-bearing phases such as garnet (Simpson *et al.* 2021). Additionally, incorporation of Mn in the activity–composition relations for amphibole and clinopyroxene in the thermodynamic dataset for mafic systems (Green

et al. 2016) would also greatly enhance accuracy for garnet modelling (White *et al.* 2014). Recent advances using *in situ* U–Pb dating of garnet have also demonstrated significant potential (e.g. Seman *et al.* 2017; Millonig *et al.* 2020; Schannor *et al.* 2021) and applicability to almandine compositions (e.g. Cerva-Alves *et al.* 2021; Schannor *et al.* 2021). Further advances aim to extend the range of metasomatic and metamorphic garnet composition that can be targeted using this technique (Millonig *et al.* 2022; O'Sullivan *et al.* 2023). Finally, the continuous development of quantitative elemental and mineral map tools (e.g. XMapTools) along with EPMA and LA-ICP-MS trace element maps (e.g. Chew *et al.* 2021) will prove an extremely powerful tool to enhance *in situ* microanalytical investigations and our understanding of complex micro-chemical processes. The Bingo-Antidote add-on to XMapTools performs thermodynamic calculations by comparing modelled and observed mineral assemblages, modes and compositions (Duesterhoeft and Lanari 2020).

Zircon can preserve a realm of information that can be retrieved from images (optical, SEM), mineral inclusions and elemental and isotope data (e.g. Th/U, REE, $\delta^{18}O$, ε_{Hf}, $\delta^{30}Si$). Although zircon has long been used in igneous and metamorphic studies, recent technical and methodological advances allow to further extend our use of this mineral. These include analytical improvements in $\delta^{30}Si$ and $\delta^{94}Zr$ data acquisition to enhance and extend the use of these isotopes in zircon studies, and the integration of EBSD data with petrochronological investigation to better understand TE diffusion in zircon crystals under various *P*–*T* conditions. Pioneer work on elastic geobarometry for a noncubic host-inclusion system indicates potential of anisotropic quartz-in-zircon elastic model for elastic thermobarometry, and its potential wide applicability to crustal rocks (Gonzalez *et al.* 2021).

Monazite is an increasingly useful accessory mineral as it can be used to trace the presence of certain fluids (e.g. Weinberg *et al.* 2020; Salminen *et al.* 2022), and can potentially grow throughout metamorphism (e.g. Larson *et al.* 2022). With improvement of analytical and spatial resolution, even if highly zoned, monazite will only become more applicable for unravelling complex and multifaceted processes. However, even with the collection of *in situ* data, it can still be challenging to tie monazite growth to deformation and fluid-related processes. Further work into monazite behaviour under deformation combined with the use of EBSD may prove a powerful tool. Additionally, the integration of EBSD, crystallographic vorticity axis analysis and petrochronology should be applied to monazite within deformational structures as it has been done for zircon (Brown *et al.* 2022). More work needs to be done on monazite TE partitioning to better understand temperature dependencies (e.g. Larson *et al.* 2022). Some attempts have been made to thermodynamically model monazite and xenotime (e.g. Kelsey *et al.* 2007, 2008; Spear and Pyle 2010; Shrestha *et al.* 2019), however, this approach only works with low-Ca bulk-rock compositions and requires the simplification of a complicated system. These current limitations represent an extensive platform for improvements in this field.

Titanite is a very reactive mineral compared to other accessory minerals; however, its tendency to incorporate initial Pb requires combining U–Pb dating with trace-element composition, zoning and microstructural information to accurately filter out any additional, unrelated radiogenic Pb (Walters *et al.* 2022). Analytical improvement in acquisition of Sm–Nd and O isotopic analysis in titanite may be extremely beneficial to trace magmatic sources (e.g. Bonamici *et al.* 2014; Bruand *et al.* 2019, 2020) and the origin of fluids playing a major role in crustal-scale shear zones (Gordon *et al.* 2021; Moser *et al.* 2022) and ore deposit (e.g. Marfin *et al.* 2020) genesis. The assessment of ilmenite U–Pb dating by LA-ICP-MS (Thompson *et al.* 2021) may be a valuable contribution for evaluating residual initial Pb affecting titanite dating. It may also be useful to investigate the timing of replacement of these Ti-rich phases. Advancing and developing the recent application of elastic geothermobarometry of host-inclusion systems (e.g. Mazzucchelli *et al.* 2021) to titanite grains may provide a complementary non-destructive method to estimate the *P* and *T* at which inclusions were trapped in the hosting titanite (Nestola 2021).

Rutile is a crucial mineral to unravel the early history of rock's evolution, including the prograde, UHP, burial stage (e.g. Rezvukhina *et al.* 2021; Manzotti *et al.* 2022), to trace melt sources in magmatic systems using Lu–Hf as isotopic tracer (e.g. Ewing *et al.* 2011) and hydrothermal, metasomatic processes associated with ore deposit genesis (e.g. Agangi *et al.* 2019; Ballouard *et al.* 2020; Porter *et al.* 2020; Sciuba and Beaudoin 2021). Therefore, analytical advances in microanalytical and petrochronological investigations of this mineral phase are essential to contribute to our understanding of orogenic systems, tectonic environments and exploration strategies. A better micro- to nanoscale understanding of trace element mobility in rutile (Kooijman *et al.* 2012; Ewing *et al.* 2013; Kohn *et al.* 2016; Pape *et al.* 2016; Penniston-Dorland *et al.* 2018; Smye *et al.* 2018) may improve U–Pb dating and associated trace element distribution and isotopic information (Verberne *et al.* 2022*a*, *b*), including the investigation of Zr transport through the rock's matrix (Ewing *et al.* 2013; Kohn *et al.* 2016). Also, advancing the use of integrated EBSD

investigations of rutile grains within different rock-types with LA-ICP-MS trace element mapping may significantly enhance our understanding of trace element partitioning and concentration in this mineral.

Allanite has overcome various challenges as a petrochronometer. Indeed, the highly variable composition of natural allanite complicates petrological interpretations and applications. Thermobarometric, isotopic (e.g. *in situ* oxygen) and TE-based petrological investigations have to be carried out using microanalytical techniques such as EBSD and/or LA-ICP-MS TE maps to explore these compositional variations. The use of compositional maps to distinguish different generations of allanite has proven to be an essential step in geochronological and petrological studies (e.g. Burn 2016; Airaghi *et al.* 2019; Corti *et al.* 2020), and the use of TE maps obtained with LA-ICP-MS can improve classification and understanding of allanite growth history. The chemical distinction between magmatic and metamorphic allanite has been enhanced by machine learning (e.g. Di Rosa *et al.* 2020), but more data are required to improve this classification. Nd and Sr isotopes are valuable geochemical tools that have been utilized in previous studies. Recent analytical advancements and developments have further strengthened the importance of these isotopic systems as tracers in understanding magmatic and metamorphic processes, especially in investigations of hydrothermal processes. Also, a better comprehension of the stability conditions (pressure, temperature and fluid) of allanite and correlated accessory minerals (e.g. monazite) is required. This would involve experiments, improvements on the thermodynamic dataset and investigation of inclusions (mineral, fluid and melt) in allanite.

Apatite is a useful tool for studying crustal processes by means of a variety of petrochronology methods, continuously enhanced in their accuracy and precision. Glorie *et al.* (2022, this volume, in press) show the promising apatite Lu–Hf geochronology method using LA ICP-MS/MS, which is more likely to reveal primary apatite growth ages in reworked terranes, due to the higher *Tc*, than the U–Pb system (Fig. 1). This may be important since Odlum *et al.* (2022) show that apatite REEs and U–Pb behaviour are decoupled in high-grade gneiss samples, suggesting REEs record higher-temperature processes than U–Pb isotopic systems. LA-ICP-MS trace element mapping is a promising technique to monitor the behaviour of trace elements in accessory mineral phases, and it should be more routinely applied. In apatite, it can be used to distinguish between metamorphic and magmatic grains or identify growth zones (Henrichs *et al.* 2018, 2019; Chew *et al.* 2021). Recent techniques such as age-depth profiles and laser ablation split stream make it possible to identify individual apatite generations and can aid with interpreting data from apatite domains with complex thermal histories (Kirkland *et al.* 2018). New apatite reference material is being characterized for *in situ* apatite U–Pb petrochronology and Sr–Nd isotope geochemistry (e.g. Apen *et al.* 2022; Kennedy *et al.* 2022) to obtain more precise and robust data.

In addition to the key mineral phases discussed in this contribution, we encourage and see potential in integrating other mineral phases in magmatic and metamorphic studies. Multi-mineral studies are paramount to combine major and accessory mineral phases that record different steps of the prograde and retrograde history of a volume of rock with lower temperature petrochronometers, which may retain useful information on the youngest evolution of the system. Critical and crucial advancement in petrochronology in the near future includes *in situ* investigations, where microanalytical studies are linked to the chemical and chronological information of different minerals and associated fabrics in a rock volume. Extreme potential is foreseen in the development and acquisition of quantitative LA-ICP-MS TE (e.g. George *et al.* 2018; Muñoz-Montecinos, J. *et al.* 2023) and geochronological maps (e.g. Chew *et al.* 2021). In this scenario, by enabling near-simultaneous detection, the time of flight (TOF) detector is a key component of LA-ICP-TOF-MS, a promising technique that captures the complete elemental mass spectrum for each laser pulse (Chew *et al.* 2021). Generating quantitative chemical and geochronological maps of a whole mineral using LA-ICP-MS can facilitate exploring the relationships between internal textures and trace and major elemental variation over time. This analytical technique will allow to discriminate distinct textural domains based on the ages and major, minor and trace elements, possibly avoiding issues such as mixing domains to help the interpretation of complex mineral textures. The advances made in LA-ICP-MS imaging have made it a critical analytical technique in the geosciences, as it enables the acquisition of high-resolution geochemical data that can help to constrain the timing and nature of igneous, metamorphic, ore-forming, sedimentary and diagenetic processes.

Acknowledgements We thank Catherine Mottram and an anonymous reviewer for their constructive and insightful comments that greatly improved the manuscript. We also thank Inês Pereira for helpful comments and for her editorial handling. Martin Engi and Daniela Rubatto are thanked for insightful discussion on allanite. Vitor Barrote is thanked for long insightful discussion throughout the preparation of the manuscript about the pros and cons of using different analytical techniques in petrochronology applied to the mineral phases discussed in this manuscript.

M. Tedeschi was supported by the National Council for Scientific and Technological Development – CNPq through a Research Productivity Grant 308733/2021-5. This is contribution no. 591 of the ClerVolc program of the International Research Center for Disaster Sciences and Sustainable Development of the University of Clermont Auvergne.

Competing interests The authors declare that they have no known competing financial interests or personal relationships that could have appeared to influence the work reported in this paper.

Author contributions **SV**: conceptualization (lead), formal analysis (lead), project administration (lead), writing – original draft (lead), writing – review & editing (lead); **EB**: conceptualization (equal), formal analysis (equal), writing – original draft (equal), writing – review & editing (equal); **MG**: conceptualization (equal), formal analysis (equal), writing – original draft (equal), writing – review & editing (equal); **MT**: conceptualization (supporting), formal analysis (supporting), writing – original draft (supporting), writing – review & editing (supporting); **VVS**: conceptualization (supporting), data curation (supporting), writing – original draft (supporting), writing – review & editing (supporting); **KC**: conceptualization (supporting), data curation (supporting), writing – original draft (supporting), writing – review & editing (supporting).

Funding This research received no specific grant from any funding agency in the public, commercial or not-for-profit sectors.

Data availability Data sharing is not applicable to this article as no datasets were generated or analysed during the current study.

References

Adlakha, E. and Hattori, K. 2021. Thermotectonic events recorded by U–Pb geochronology and Zr-in-rutile thermometry of Ti oxides in basement rocks along the P2 fault, eastern Athabasca Basin, Saskatchewan, Canada. *GSA Bulletin*, **134**, 567–576, https://doi.org/10.1130/B35820.1

Aerden, D.G.A.M., Bell, T.H., Puga, E., Sayab, M., Lozano, J.A. and Diaz de Federico, A. 2013. Multi-stage mountain building v. relative plate motions in the Betic Cordillera deduced from integrated microstructural and petrological analysis of porphyroblast inclusion trails. *Tectonophysics*, **587**, 188–206, https://doi.org/10.1016/j.tecto.2012.11.025

Aerden, D.G.A.M., Ruiz-Fuentes, A., Sayab, M. and Forde, A. 2021. Kinematics of subduction in the Ibero-Armorican arc constrained by 3D microstructural analysis of garnet and pseudomorphed lawsonite porphyroblasts from Île de Groix (Variscan belt). *Solid Earth*, **12**, 971–992, https://doi.org/10.5194/se-12-971-2021

Agangi, A., Reddy, S.M., Plavsa, D., Fougerouse, D., Clark, C., Roberts, M. and Johnson, T.E. 2019. Antimony in rutile as a pathfinder for orogenic gold deposits. *Ore Geology Reviews*, **106**, 1–11, https://doi.org/10.1016/j.oregeorev.2019.01.018

Airaghi, L., Janots, E., Lanari, P., de Sigoyer, J. and Magnin, V. 2019. Allanite petrochronology in fresh and retrogressed garnet–biotite metapelites from the Longmen Shan (Eastern Tibet). *Journal of Petrology*, **60**, 151–176, https://doi.org/10.1093/petrology/egy109

Ambrose, T.K., Larson, K.P., Guilmette, C., Cottle, J.M., Buckingham, H. and Rai, S. 2015. Lateral extrusion, underplating, and out-of-sequence thrusting within the Himalayan metamorphic core, Kanchenjunga, Nepal. *Lithosphere*, **7**, 441–464, https://doi.org/10.1130/L437.1

Amelin, Y. 2009. Sm–Nd and U–Pb systematics of single titanite grains. *Chemical Geology*, **261**, 53–61, https://doi.org/10.1016/j.chemgeo.2009.01.014

Amelin, Y., Lee, D.-C. and Halliday, A.N. 2000. Early–middle Archaean crustal evolution deduced from Lu–Hf and U–Pb isotopic studies of single zircon grains. *Geochimica et Cosmochimica Acta*, **64**, 4205–4225, https://doi.org/10.1016/S0016-7037(00)00493-2

An, Y., Huang, J.-X., Griffin, W.L., Liu, C. and Huang, F. 2017. Isotopic composition of Mg and Fe in garnet peridotites from the Kaapvaal and Siberian cratons. *Geochimica et Cosmochimica Acta*, **200**, 167–185, https://doi.org/10.1016/j.gca.2016.11.041

Anderson, A.J., Hanchar, J.M., Hodges, K.V. and van Soest, M.C. 2020. Mapping radiation damage zoning in zircon using Raman spectroscopy: implications for zircon chronology. *Chemical Geology*, **538**, article 119494, https://doi.org/10.1016/j.chemgeo.2020.119494

Andersson, J., Möller, C. and Johansson, L. 2002. Zircon geochronology of migmatite gneisses along the Mylonite Zone (S Sweden): a major Sveconorwegian terrane boundary in the Baltic Shield. *Precambrian Research*, **114**, 121–147, https://doi.org/10.1016/S0301-9268(01)00220-0

Andersson, J., Bingen, B., Cornell, D., Johansson, L., Söderlund, U. and Möller, C. 2008. The Sveconorwegian orogen of southern Scandinavia: setting, petrology and geochronology of polymetamorphic high-grade terranes. *33rd International Geological Congress*, 6–14 August 2008, Oslo, Norway, Field Excursion Guide.

Andersson, J.B.H., Logan, L. *et al*. 2022. U–Pb zircon–titanite–apatite age constraints on basin development and basin inversion in the Kiruna mining district, Sweden. *Precambrian Research*, **372**, article 106613, https://doi.org/10.1016/j.precamres.2022.106613

Andrehs, G. and Heinrich, W. 1998. Experimental determination of REE distributions between monazite and xenotime: potential for temperature-calibrated geochronology. *Chemical Geology*, **149**, 83–96, https://doi.org/10.1016/S0009-2541(98)00039-4

Anenburg, M., Broom-Fendley, S. and Chen, W. 2021. Formation of rare earth deposits in carbonatites. *Elements*, **17**, 327–332. https://doi.org/10.2138/gselements.17.5.327

Antoine, C., Bruand, E., Guitreau, M. and Devidal, J. 2020. Understanding preservation of primary signatures

in apatite by comparing matrix and zircon-hosted crystals from the Eoarchean Acasta Gneiss Complex (Canada). *Geochemistry, Geophysics, Geosystems*, **21**, article e2020GC008923, https://doi.org/10.1029/2020GC008923

Apen, F.E., Rudnick, R.L., Cottle, J.M., Kylander-Clark, A.R.C., Blondes, M.S., Piccoli, P.M. and Seward, G. 2020. Four-dimensional thermal evolution of the East African Orogen: accessory phase petrochronology of crustal profiles through the Tanzanian Craton and Mozambique Belt, northeastern Tanzania. *Contributions to Mineralogy and Petrology*, **175**, article 97, https://doi.org/10.1007/s00410-020-01737-6

Apen, F.E., Wall, C.J., Cottle, J.M., Schmitz, M.D., Kylander-Clark, A.R. and Seward, G.G. 2022. Apatites for destruction: reference apatites from Morocco and Brazil for U–Pb petrochronology and Nd and Sr isotope geochemistry. *Chemical Geology*, **590**, article 120689, https://doi.org/10.1016/j.chemgeo.2021.120689

Aranovich, L.Y., Bortnikov, N. *et al*. 2017. Morphology and impurity elements of zircon in the oceanic lithosphere at the Mid-Atlantic ridge axial zone (6–13 N): evidence of specifics of magmatic crystallization and postmagmatic transformations. *Petrology*, **25**, 339–364, https://doi.org/10.1134/S0869591117040026

Armbruster, T., Bonazzi, P. *et al*. 2006. Recommended nomenclature of epidote-group minerals. *European Journal of Mineralogy*, **18**, 551–567, https://doi.org/10.1127/0935-1221/2006/0018-0551

Asami, M., Suzuki, K. and Grew, E.S. 2002. Chemical Th–U–total Pb dating by electron microprobe analysis of monazite, xenotime and zircon from the Archean Napier Complex, East Antarctica: evidence for ultra-high-temperature metamorphism at 2400 Ma. *Precambrian Research*, **114**, 249–275, https://doi.org/10.1016/S0301-9268(01)00228-5

Atherton, M.P. 1968. The variation in garnet, biotite and chlorite composition in medium grade pelitic rocks from the Dalradian, Scotland, with particular reference to the zonation in garnet. *Contributions to Mineralogy and Petrology*, **18**, 347–371, https://doi.org/10.1007/BF00399696

Aulbach, S., O'Reilly, S.Y., Griffin, W. and Pearson, N.J. 2008. Subcontinental lithospheric mantle origin of high niobium/tantalum ratios in eclogites. *Nature Geoscience*, **1**, 468–472, https://doi.org/10.1038/ngeo226

Axelsson, E., Pape, J., Berndt, J., Corfu, F., Mezger, K. and Raith, M.M. 2018. Rutile R632 – a new natural reference material for U–Pb and Zr determination. *Geostandards and Geoanalytical Research*, **42**, 319–338, https://doi.org/10.1111/ggr.12213

Aysal, N., Guillong, M. *et al*. 2023. A New Natural Secondary Reference Material for Garnet U-Pb Dating by TIMS and LA-ICP-MS. *Geostandards and Geoanalytical Rsearch*, https://doi.org/10.1111/ggr.12493

Balan, E., Neuville, D.R., Trocellier, P., Fritsch, E., Muller, J.-P. and Calas, G. 2001. Metamictization and chemical durability of detrital zircon. *American Mineralogist*, **86**, 1025–1033, https://doi.org/10.2138/am-2001-8-909

Baldwin, J.A. and Brown, M. 2008. Age and duration of ultrahigh-temperature metamorphism in the Anápolis–Itauçu Complex, Southern Brasília Belt, central Brazil – constraints from U–Pb geochronology, mineral rare earth element chemistry and trace-element thermometry. *Journal of Metamorphic Geology*, **26**, 213–233, https://doi.org/10.1111/j.1525-1314.2007.00759.x

Ballouard, C., Massuyeau, M., Elburg, M.A., Tappe, S., Viljoen, F. and Brandenburg, J.-T. 2020. The magmatic and magmatic-hydrothermal evolution of felsic igneous rocks as seen through Nb–Ta geochemical fractionation, with implications for the origins of rare-metal mineralizations. *Earth-Science Reviews*, **203**, article 103115, https://doi.org/10.1016/j.earscirev.2020.103115

Barboni, M., Schoene, B., Ovtcharova, M., Bussy, F., Schaltegger, U. and Gerdes, A. 2013. Timing of incremental pluton construction and magmatic activity in a back-arc setting revealed by ID-TIMS U/Pb and Hf isotopes on complex zircon grains. *Chemical Geology*, **342**, 76–93, https://doi.org/10.1016/j.chemgeo.2012.12.011

Barfod, G.H., Otero, O. and Albarède, F. 2003. Phosphate Lu–Hf geochronology. *Chemical Geology*, **200**, 241–253, https://doi.org/10.1016/S0009-2541(03)00202-X

Barfod, G.H., Krogstad, E.J., Frei, R. and Albarède, F. 2005. Lu–Hf and PbSL geochronology of apatites from Proterozoic terranes: a first look at Lu–Hf isotopic closure in metamorphic apatite. *Geochimica et Cosmochimica Acta*, **69**, 1847–1859, https://doi.org/10.1016/j.gca.2004.09.014

Barla, A. 2021. Titanite petrochronology by LA-ICPMS: method and significance in deciphering igneous processes, Msc Thesis, University of Arizona, USA.

Barrote, V.R., McNaughton, N.J., Tessalina, S.G., Evans, N.J., Talavera, C., Zi, J.-W. and McDonald, B.J. 2020. The 4D evolution of the Teutonic Bore Camp VHMS deposits, Yilgarn Craton, Western Australia. *Ore Geology Reviews*, **120**, article 103448, https://doi.org/10.1016/j.oregeorev.2020.103448

Barrote, V.R., Nebel, O., Wainwright, A.N., Cawood, P.A., Hollis, S.P. and Raveggi, M. 2022*a*. Testing the advantages of simultaneous *in-situ* SmNd, UPb and elemental analysis of igneous monazite for petrochronological studies. An example from the late Archean, Penzance granite, Western Australia. *Chemical Geology*, **594**, article 120760, https://doi.org/10.1016/j.chemgeo.2022.120760

Barrote, V.R., Volante, S., Blereau, E.R., Rosière, C.A. and Spencer, C.J. 2022*b*. Implications of the dominant *LP–HT* deformation in the Guanhães Block for the Araçuaí West-Congo Orogen evolution. *Gondwana Research*, **107**, 154–175, https://doi.org/10.1016/j.gr.2022.03.012

Barrow, G. 1893. On an intrusion of muscovite–biotite gneiss in the South-eastern Highlands of Scotland, and its accompanying metamorphism. *Quarterly Journal of the Geological Society*, **49**, 330–358, https://doi.org/10.1144/GSL.JGS.1893.049.01-04.52

Barrow, G. 1912. On the geology of lower Dee-side and the southern Highland border. *Proceedings of the Geologists' Association*, **23**, 274–290, https://doi.org/10.1016/S0016-7878(12)80018-6

Barth, S., Oberli, F. and Meier, M. 1994. ThPb v. UPb isotope systematics in allanite from co-genetic rhyolite and granodiorite: implications for geochronology. *Earth and Planetary Science Letters*, **124**, 149–159, https://doi.org/10.1016/0012-821X(94)00073-5

Bartoli, O., Cesare, B., Poli, S., Bodnar, R.J., Acosta-Vigil, A., Frezzotti, M.L. and Meli, S. 2013. Recovering the composition of melt and the fluid regime at the onset of crustal anatexis and S-type granite formation. *Geology*, **41**, 115–118, https://doi.org/10.1130/G33455.1

Baxter, E.F. and Scherer, E.E. 2013. Garnet geochronology: timekeeper of tectonometamorphic processes. *Elements*, **9**, 433–438, https://doi.org/10.2113/gselements.9.6.433

Baxter, E.F., Caddick, M.J. and Dragovic, B. 2017. Garnet: a rock-forming mineral petrochronometer. *Reviews in Mineralogy and Geochemistry*, **83**, 469–533, https://doi.org/10.2138/rmg.2017.83.15

Bea, F. 1996. Residence of REE, Y, Th and U in granites and crustal protoliths; implications for the chemistry of crustal melts. *Journal of Petrology*, **37**, 521–552, https://doi.org/10.1093/petrology/37.3.521

Bea, F. and Montero, P. 1999. Behavior of accessory phases and redistribution of Zr, REE, Y, Th, and U during metamorphism and partial melting of metapelites in the lower crust: an example from the Kinzigite Formation of Ivrea–Verbano, NW Italy. *Geochimica et Cosmochimica Acta*, **63**, 1133–1153, https://doi.org/10.1016/S0016-7037(98)00292-0

Bea, F., Pereira, M.D. and Stroh, A. 1994. Mineral/leucosome trace-element partitioning in a peraluminous migmatite (a laser ablation-ICP-MS study). *Chemical Geology*, **117**, 291–312, https://doi.org/10.1016/0009-2541(94)90133-3

Bea, F., Morales, I., Molina, J.F., Montero, P. and Cambeses, A. 2021. Zircon stability grids in crustal partial melts: implications for zircon inheritance. *Contributions to Mineralogy and Petrology*, **176**, 1–13, https://doi.org/10.1007/s00410-020-01755-4

Bea, F., Bortnikov, N. *et al*. 2022. Zircon crystallization in low-Zr mafic magmas: possible or impossible? *Chemical Geology*, **602**, article 120898, https://doi.org/10.1016/j.chemgeo.2022.120898

Bebout, G.E., Tsujimori, T., Ota, T., Shimaki, Y., Kunihiro, T., Carlson, W.D. and Nakamura, E. 2014. Lithium behavior during growth of metasedimentary garnets from the Cignana UHP locality, Italy. *American Geophysical Union Fall Meeting*, 15–19 December 2014, San Francisco, CA, Abstracts, V31D-4783.

Bebout, G.E., Ota, T., Kunihiro, T., Carlson, W.D. and Nakamura, E. 2022. Lithium in garnet as a tracer of subduction zone metamorphic reactions: the record in ultrahigh-pressure metapelites at Lago di Cignana, Italy. *Geosphere*, **18**, 1020–1029, https://doi.org/10.1130/GES02473.1

Bell, E.A., Boehnke, P., Hopkins-Wielicki, M.D. and Harrison, T.M. 2015. Distinguishing primary and secondary inclusion assemblages in Jack Hills zircons. *Lithos*, **234**, 15–26, https://doi.org/10.1016/j.lithos.2015.07.014

Belousova, E.A., Walters, S., Griffin, W.L. and O'Reilly, S.Y. 2001. Trace-element signatures of apatites in granitoids from the Mt Isa Inlier, northwestern Queensland. *Australian Journal of Earth Sciences*, **48**, 603–619, https://doi.org/10.1046/j.1440-0952.2001.00879.x

Belousova, E., Griffin, W.L., O'Reilly, S.Y. and Fisher, N. 2002. Igneous zircon: trace element composition as an indicator of source rock type. *Contributions to Mineralogy and Petrology*, **143**, 602–622, https://doi.org/10.1007/s00410-002-0364-7

Berman, R.G. 1988. Internally-consistent thermodynamic data for minerals in the system Na_2O–K2O–CaO–MgO–FeO–Fe_2O_3–Al_2O_3–SiO_2–TiO_2–H_2O–CO_2. *Journal of Petrology*, **29**, 445–522, https://doi.org/10.1093/petrology/29.2.445

Bindeman, I. 2008. Oxygen isotopes in mantle and crustal magmas as revealed by single crystal analysis. *Reviews in Mineralogy and Geochemistry*, **69**, 445–478, https://doi.org/10.2138/rmg.2008.69.12

Bingen, B., Demaiffe, D. and Hertogen, J. 1996. Redistribution of rare earth elements, thorium, and uranium over accessory minerals in the course of amphibolite to granulite facies metamorphism: the role of apatite and monazite in orthogneisses from southwestern Norway. *Geochimica et Cosmochimica Acta*, **60**, 1341–1354, https://doi.org/10.1016/0016-7037(96)00006-3

Black, L.P. 1988. Isotopic resetting of U–Pb zircon and Rb–Sr and Sm–Nd whole-rock systems in Enderby Land, Antarctica: implications for the interpretation of isotopic data from polymetamorphic and multiply deformed terrains. *Precambrian Research*, **38**, 355–365, https://doi.org/10.1016/0301-9268(88)90033-2

Black, L.P., Fitzgerald, J.D. and Harley, S.L. 1984. Pb isotopic composition, colour, and microstructure of monazites from a polymetamorphic rock in Antarctica. *Contributions to Mineralogy and Petrology*, **85**, 141–148, https://doi.org/10.1007/BF00371704

Blereau, E., Clark, C., Taylor, R.J., Johnson, T., Fitzsimons, I. and Santosh, M. 2016. Constraints on the timing and conditions of high-grade metamorphism, charnockite formation and fluid–rock interaction in the Trivandrum Block, southern India. *Journal of Metamorphic Geology*, **34**, 527–549, https://doi.org/10.1111/jmg.12192

Blereau, E. 2017. A Petrochronological Investigation of Metamorphic, Melt and Fluid Related Processes in Lower Crustal Rocks from Southwestern Norway and Southern India. PhD Thesis, Curtin University, Western Australia. http://hdl.handle.net/20.500.11937/59704

Blereau, E., Clark, C., Kinny, P.D., Sansom, E., Taylor, R.J.M. and Hand, M. 2022. Probing the history of ultra-high temperature metamorphism through rare earth element diffusion in zircon. *Journal of Metamorphic Geology*, **40**, 329–357, https://doi.org/10.1111/jmg.12630

Blichert-Toft, J. and Albarède, F. 1997. The Lu–Hf isotope geochemistry of chondrites and the evolution of the mantle–crust system. *Earth and Planetary Science Letters*, **148**, 243–258, https://doi.org/10.1016/S0012-821X(97)00040-X

Bloch, E., Jollands, M. *et al*. 2022. Diffusion anisotropy of Ti in zircon and implications for Ti-in-zircon thermometry. *Earth and Planetary Science Letters*, **578**, article 117317, https://doi.org/10.1016/j.epsl.2021.117317

Boehnke, P., Watson, E.B., Trail, D., Harrison, T.M. and Schmitt, A.K. 2013. Zircon saturation re-revisited. *Chemical Geology*, **351**, 324–334, https://doi.org/10.1016/j.chemgeo.2013.05.028

Böhnke, M., Bröcker, M., Maulana, A., Klemd, R., Berndt, J. and Baier, H. 2019. Geochronology and Zr-in-rutile thermometry of high-pressure/low temperature metamorphic rocks from the Bantimala complex, SW

Sulawesi, Indonesia. *Lithos*, **324–325**, 340–355, https://doi.org/10.1016/j.lithos.2018.11.020

Bollen, E.M., Stowell, H.H., Aronoff, R.F., Stotter, S.V., Daniel, C.G., McFarlane, C.R.M. and Vervoort, J.D. 2022. Reconciling garnet Lu–Hf and Sm–Nd and monazite U–Pb ages for a prolonged metamorphic event, northern New Mexico. *Journal of Petrology*, **63**, article egac031, https://doi.org/10.1093/petrology/egac031

Bonamici, C.E. and Blum, T.B. 2020. Reconsidering initial Pb in titanite in the context of *in situ* dating. *American Mineralogist: Journal of Earth and Planetary Materials*, **105**, 1672–1685, https://doi.org/10.2138/am-2020-7274

Bonamici, C.E., Kozdon, R., Ushikubo, T. and Valley, J.W. 2011. High-resolution P–T–t paths from $\delta^{18}O$ zoning in titanite: a snapshot of late-orogenic collapse in the Grenville of New York. *Geology*, **39**, 959–962, https://doi.org/10.1130/G32130.1

Bonamici, C.E., Kozdon, R., Ushikubo, T. and Valley, J.W. 2014. Intragrain oxygen isotope zoning in titanite by SIMS: cooling rates and fluid infiltration along the Carthage-Colton Mylonite Zone, Adirondack Mountains, NY, USA. *Journal of Metamorphic Geology*, **32**, 71–92, https://doi.org/10.1111/jmg.12059

Bonamici, C.E., Fanning, C.M., Kozdon, R., Fournelle, J.H. and Valley, J.W. 2015. Combined oxygen-isotope and U–Pb zoning studies of titanite: new criteria for age preservation. *Chemical Geology*, **398**, 70–84, https://doi.org/10.1016/j.chemgeo.2015.02.002

Bonnet, G., Chopin, C., Locatelli, M., Kylander-Clark, A.R.C. and Hacker, B.R. 2022. Protracted subduction of the European hyperextended margin revealed by rutile U–Pb geochronology across the Dora-Maira Massif (Western Alps). *Tectonics*, **41**, article e2021 TC007170, https://doi.org/10.1029/2021TC007170

Borghini, A., Ferrero, S., O'Brien, P.J., Laurent, O., Günter, C. and Ziemann, M.A. 2020. Cryptic metasomatic agent measured *in situ* in Variscan mantle rocks: melt inclusions in garnet of eclogite, Granulitgebirge, Germany. *Journal of Metamorphic Geology*, **38**, 207–234, https://doi.org/10.1111/jmg.12519

Bosse, V. and Villa, I.M. 2019. Petrochronology and hygrochronology of tectono-metamorphic events. *Gondwana Research*, **71**, 76–90, https://doi.org/10.1016/j.gr.2018.12.014

Boston, K.R., Rubatto, D., Hermann, J., Engi, M. and Amelin, Y. 2017. Geochronology of accessory allanite and monazite in the Barrovian metamorphic sequence of the Central Alps, Switzerland. *Lithos*, **286**, 502–518, https://doi.org/10.1016/j.lithos.2017.06.025

Bouvier, A., Vervoort, J.D. and Patchett, P.J. 2008. The Lu–Hf and Sm–Nd isotopic composition of CHUR: constraints from unequilibrated chondrites and implications for the bulk composition of terrestrial planets. *Earth and Planetary Science Letters*, **273**, 48–57, https://doi.org/10.1016/j.epsl.2008.06.010

Bouvier, A.-S., Ushikubo, T., Kita, N.T., Cavosie, A.J., Kozdon, R. and Valley, J.W. 2012. Li isotopes and trace elements as a petrogenetic tracer in zircon: insights from Archean TTGs and sanukitoids. *Contributions to Mineralogy and Petrology*, **163**, 745–768, https://doi.org/10.1007/s00410-011-0697-1

Braun, I., Montel, J.-M. and Nicollet, C. 1998. Electron microprobe dating of monazites from high-grade gneisses and pegmatites of the Kerala Khondalite Belt, southern India. *Chemical Geology*, **146**, 65–85, https://doi.org/10.1016/S0009-2541(98)00005-9

Brown, D.A., Simpson, A., Hand, M., Morrissey, L.J., Gilbert, S., Tamblyn, R. and Glorie, S. 2022. Laser-ablation Lu–Hf dating reveals Laurentian garnet in subducted rocks from southern Australia. *Geology*, **50**, 837–842, https://doi.org/10.1130/G49784.1

Bruand, E., Storey, C. and Fowler, M. 2014. Accessory mineral chemistry of high Ba–Sr granites from northern Scotland: constraints on petrogenesis and records of whole-rock signature. *Journal of Petrology*, **55**, 1619–1651, https://doi.org/10.1093/petrology/egu037

Bruand, E., Fowler, M., Storey, C. and Darling, J. 2017. Apatite trace element and isotope applications to petrogenesis and provenance. *American Mineralogist*, **102**, 75–84, https://doi.org/10.2138/am-2017-5744

Bruand, E., Storey, C., Fowler, M. and Heilimo, E. 2019. Oxygen isotopes in titanite and apatite, and their potential for crustal evolution research. *Geochimica et Cosmochimica Acta*, **255**, 144–162, https://doi.org/10.1016/j.gca.2019.04.002

Bruand, E., Fowler, M. *et al*. 2020. Accessory mineral constraints on crustal evolution: elemental fingerprints for magma discrimination. *Geochemical Perspectives Letters*, **13**, 7–12, https://doi.org/10.7185/geochemlet.2006

Budzyń, B., Hetherington, C.J., Williams, M.L., Jercinovic, M.J. and Michalik, M. 2010. Fluid–mineral interactions and constraints on monazite alteration during metamorphism. *Mineralogical Magazine*, **74**, 659–681, https://doi.org/10.1180/minmag.2010.074.4.659

Buick, I.S., Hermann, J., Williams, I.S., Gibson, R.L. and Rubatto, D. 2006. A SHRIMP U–Pb and LA-ICP-MS trace element study of the petrogenesis of garnet–cordierite–orthoamphibole gneisses from the Central Zone of the Limpopo Belt, South Africa. *Lithos*, **88**, 150–172, https://doi.org/10.1016/j.lithos.2005.09.001

Buick, I.S., Clark, C., Rubatto, D., Hermann, J., Pandit, M. and Hand, M. 2010. Constraints on the Proterozoic evolution of the Aravalli–Delhi Orogenic Belt (NW India) from monazite geochronology and mineral trace element geochemistry. *Lithos*, **120**, 511–528, https://doi.org/10.1016/j.lithos.2010.09.011

Burn, M. 2016. LA-ICP-QMS Th–U/Pb allanite dating: methods and applications, Doctoral dissertation, Philosophisch-naturwissenschfatliche Fakultät der Universität Bern, Germany.

Burn, M., Lanari, P., Pettke, T. and Engi, M. 2017. Non-matrix-matched standardisation in LA-ICP-MS analysis: general approach, and application to allanite Th–U–Pb dating. *Journal of Analytical Atomic Spectrometry*, **32**, 1359–1377, https://doi.org/10.1039/C7JA00095B

Caddick, M.J. and Thompson, A.B. 2008. Quantifying the tectono-metamorphic evolution of pelitic rocks from a wide range of tectonic settings: mineral compositions in equilibrium. *Contributions to Mineralogy and Petrology*, **156**, 177–195, https://doi.org/10.1007/s00410-008-0280-6

Caddick, M.J., Konopásek, J. and Thompson, A.B. 2010. Preservation of garnet growth zoning and the duration of prograde metamorphism. *Journal of Petrology*, **51**, 2327–2347, https://doi.org/10.1093/petrology/egq059

Campomenosi, N., Scambelluri, M. *et al*. 2021. Using the elastic properties of zircon–garnet host-inclusion pairs for thermobarometry of the ultrahigh-pressure Dora-Maira whiteschists: problems and perspectives. *Contributions to Mineralogy and Petrology*, **176**, article 36, https://doi.org/10.1007/s00410-021-01793-6

Cao, M., Qin, K., Li, G., Evans, N.J. and Jin, L. 2015. *In situ* LA-(MC)-ICP-MS trace element and Nd isotopic compositions and genesis of polygenetic titanite from the Baogutu reduced porphyry Cu deposit, Western Junggar, NW China. *Ore Geology Reviews*, **65**, 940–954, https://doi.org/10.1016/j.oregeorev.2014.07.014

Carruzzo, S., Clarke, D.B., Pelrine, K.M. and MacDonald, M.A. 2006. Texture, composition, and origin of rutile in the South Mountain Batholith, Nova Scotia. *The Canadian Mineralogist*, **44**, 715–729, https://doi.org/10.2113/gscanmin.44.3.715

Carvalho, B.B., Bartoli, O. *et al*. 2019. Anatexis and fluid regime of the deep continental crust: new clues from melt and fluid inclusions in metapelitic migmatites from Ivrea Zone (NW Italy). *Journal of Metamorphic Geology*, **37**, 951–975, https://doi.org/10.1111/jmg.12463

Castelli, D. and Rubatto, D. 2002. Stability of Al- and F-rich titanite in metacarbonate: petrologic and isotopic constraints from a polymetamorphic eclogitic marble of the internal Sesia Zone (Western Alps). *Contributions to Mineralogy and Petrology*, **142**, 627–639, https://doi.org/10.1007/s00410-001-0317-6

Catlos, E., Sorensen, S.S. and Harrison, T.M. 2000. Th–Pb ion-microprobe dating of allanite. *American Mineralogist*, **85**, 633–648, https://doi.org/10.2138/am-2000-5-601

Cavosie, A.J., Erickson, T.M. *et al*. 2015. A terrestrial perspective on using *ex situ* shocked zircons to date lunar impacts. *Geology*, **43**, 999–1002, https://doi.org/10.1130/G37059.1

Cavosie, A.J., Spencer, C.J., Evans, N., Rankenburg, K., Thomas, R.J. and Macey, P.H. 2022. Granular titanite from the Roter Kamm crater in Namibia: product of regional metamorphism, not meteorite impact. *Geoscience Frontiers*, **13**, article 101350, https://doi.org/10.1016/j.gsf.2022.101350

Caxito, F.A., Basto, C.F. *et al*. 2021. Neoproterozoic magmatic arc volcanism in the Borborema Province, NE Brazil: possible flare-ups and lulls and implications for western Gondwana assembly. *Gondwana Research*, **92**, 1–25, https://doi.org/10.1016/j.gr.2020.11.015

Cenki-Tok, B., Oliot, E. *et al*. 2011. Preservation of Permian allanite within an Alpine eclogite facies shear zone at Mt Mucrone, Italy: mechanical and chemical behavior of allanite during mylonitization. *Lithos*, **125**, 40–50, https://doi.org/10.1016/j.lithos.2011.01.005

Cenki-Tok, B., Darling, J.R., Rolland, Y., Dhuime, B. and Storey, C.D. 2014. Direct dating of mid-crustal shear zones with synkinematic allanite: new *in situ* U–Th–Pb geochronological approaches applied to the Mont Blanc Massif. *Terra Nova*, **26**, 29–37, https://doi.org/10.1111/ter.12066

Cerny, P., Novak, M., Chapman, R. and Ferreira, K.J. 2007. Subsolidus behavior of niobian rutile from the Pisek region, Czech Republic: a model for exsolution in W- and Fe^{2+} >>Fe^{3+} -rich phases. *Journal of Geosciences*, **52**, 143–159, https://doi.org/10.3190/jgeosci.008

Cerva-Alves, T., Hartmann, L.A., Queiroga, G.N., Lana, C., Castro, M.P., Maciel, L.A.C. and Remus, M.V.D. 2021. Metamorphic evolution of the juvenile Serrinha forearc basin in the southern Brasiliano Orogen. *Precambrian Research*, **365**, article 106394, https://doi.org/10.1016/j.precamres.2021.106394

Cesare, B., Ferrero, S., Salvioli-Mariani, E., Pedron, D. and Cavallo, A. 2009. 'Nanogranite' and glassy inclusions: the anatectic melt in migmatites and granulites. *Geology*, **37**, 627–630, https://doi.org/10.1130/G25759A.1

Cesare, B., Acosta-Vigil, A., Ferrero, S., Bartoli, O. and Forster, M. 2011. Melt inclusions in migmatites and granulites. *Journal of the Virtual Explorer*, **38**, article 2, https://doi.org/10.3809/jvirtex.2011.00268

Chakhmouradian, A.R., Reguir, E.P. *et al*. 2017. Apatite in carbonatitic rocks: compositional variation, zoning, element partitioning and petrogenetic significance. *Lithos*, **274**, 188–213, https://doi.org/10.1016/j.lithos.2016.12.037

Chamberlain, C.P. and Conrad, M.E. 1991. Oxygen isotope zoning in garnet. *Science*, **254**, 403–406, https://doi.org/10.1126/science.254.5030.403

Chamberlain, K.R., Schmitt, A.K. *et al*. 2010. *In situ* U–Pb SIMS (IN-SIMS) micro-baddeleyite dating of mafic rocks: method with examples. *Precambrian Research*, **183**, 379–387, https://doi.org/10.1016/j.precamres.2010.05.004

Chaussidon, M., Deng, Z., Villeneuve, J., Moureau, J., Watson, B., Richter, F. and Moynier, F. 2017. *In situ* analysis of non-traditional isotopes by SIMS and LA-MC-ICP-MS: key aspects and the example of Mg isotopes in olivines and silicate glasses. *Reviews in Mineralogy and Geochemistry*, **82**, 127–163, https://doi.org/10.2138/rmg.2017.82.5

Chen, X., Wang, W., Zhang, Z., Nie, N.X. and Dauphas, N. 2020. Evidence from Ab initio and transport modeling for diffusion-driven zirconium isotopic fractionation in igneous rocks. *ACS Earth and Space Chemistry*, **4**, 1572–1595, https://doi.org/10.1021/acsearthspacechem.0c00146

Cherniak, D.J. 1993. Lead diffusion in titanite and preliminary results on the effects of radiation damage on Pb transport. *Chemical Geology*, **110**, 177–194, https://doi.org/10.1016/0009-2541(93)90253-F

Cherniak, D.J. 1995. Sr and Nd diffusion in titanite. *Chemical Geology*, **125**, 219–232, https://doi.org/10.1016/0009-2541(95)00074-V

Cherniak, D.J. 2000*a*. Pb diffusion in rutile. *Contributions to Mineralogy and Petrology*, **139**, 198–207, https://doi.org/10.1007/PL00007671

Cherniak, D.J. 2000*b*. Rare earth element diffusion in apatite. *Geochimica et Cosmochimica Acta*, **64**, 3871– 3885, https://doi.org/10.1016/S0016-7037(00)00467-1

Cherniak, D.J. 2006. Pb and rare earth element diffusion in xenotime. *Lithos*, **88**, 1–14, https://doi.org/10.1016/j.lithos.2005.08.002

Cherniak, D.J. and Watson, E.B. 2001. Pb diffusion in zircon. *Chemical Geology*, **172**, 5–24, https://doi.org/10.1016/S0009-2541(00)00233-3

Cherniak, D.J. and Watson, E.B. 2003. Diffusion in zircon. *Reviews in Mineralogy and Geochemistry*, **53**, 113–143, https://doi.org/10.2113/0530113

Cherniak, D.J. and Watson, E. 2007. Ti diffusion in zircon. *Chemical Geology*, **242**, 470–483, https://doi.org/10.1016/j.chemgeo.2007.05.005

Cherniak, D.J., Lanford, W.A. and Ryerson, F.J. 1991. Lead diffusion in apatite and zircon using ion implantation and Rutherford backscattering techniques. *Geochimica et Cosmochimica Acta*, **55**, 1663–1673, https://doi.org/10.1016/0016-7037(91)90137-T

Cherniak, D.J., Watson, E.B., Grove, M. and Harrison, T.M. 2004. Pb diffusion in monazite: a combined RBS/SIMS study. *Geochimica et Cosmochimica Acta*, **68**, 829–840, https://doi.org/10.1016/j.gca.2003.07.012

Cherniak, D.J., Manchester, J. and Watson, E. 2007. Zr and Hf diffusion in rutile. *Earth and Planetary Science Letters*, **261**, 267–279, https://doi.org/10.1016/j.epsl.2007.06.027

Chew, D.M. and Spikings, R.A. 2015. Geochronology and thermochronology using apatite: time and temperature, lower crust to surface. *Elements*, **11**, 189–194, https://doi.org/10.2113/gselements.11.3.189

Chew, D.M., Sylvester, P.J. and Tubrett, M.N. 2011. U–Pb and Th–Pb dating of apatite by LA-ICPMS. *Chemical Geology*, **280**, 200–216, https://doi.org/10.1016/j.chemgeo.2010.11.010

Chew, D.M., Petrus, J.A. and Kamber, B.S. 2014. U–Pb LA-ICPMS dating using accessory mineral standards with variable common Pb. *Chemical Geology*, **363**, 185–199, https://doi.org/10.1016/j.chemgeo.2013.11.006

Chew, D.M., Petrus, J.A., Kenny, G.G. and McEvoy, N. 2017. Rapid high-resolution U–Pb LA-Q-ICPMS age mapping of zircon. *Journal of Analytical Atomic Spectrometry*, **32**, 262–276, https://doi.org/10.1039/C6JA00404K

Chew, D., Drost, K., Marsh, J.H. and Petrus, J.A. 2021. LA-ICP-MS imaging in the geosciences and its applications to geochronology. *Chemical Geology*, **559**, article 119917, https://doi.org/10.1016/j.chemgeo.2020.119917

Choukroun, M., O'Reilly, S.Y., Griffin, W.L., Pearson, N.J. and Dawson, J.B. 2005. Hf isotopes of MARID (mica–amphibole–rutile–ilmenite–diopside) rutile trace metasomatic processes in the lithospheric mantle. *Geology*, **33**, 45–48, https://doi.org/10.1130/G21084.1

Chu, M.-F., Wang, K.-L., Griffin, W.L., Chung, S.-L., O'Reilly, S.Y., Pearson, N.J. and Iizuka, Y. 2009. Apatite composition: tracing petrogenetic processes in Transhimalayan granitoids. *Journal of Petrology*, **50**, 1829–1855, https://doi.org/10.1093/petrology/egp054

Cioffi, C.R., da Campos Neto, M.C., Möller, A. and Rocha, B.C. 2019. Titanite petrochronology of the southern Brasília Orogen basement: effects of retrograde net-transfer reactions on titanite trace element compositions. *Lithos*, **344–345**, 393–408, https://doi.org/10.1016/j.lithos.2019.06.035

Clark, C., Collins, A.S., Santosh, M., Taylor, R. and Wade, B.P. 2009. The P–T–t architecture of a Gondwanan suture: REE, U–Pb and Ti-in-zircon thermometric constraints from the Palghat Cauvery shear system, South India. *Precambrian Research*, **174**, 129–144, https://doi.org/10.1016/J.PRECAMRES.2009.07.003

Clark, C., Kirkland, C.L., Spaggiari, C.V., Oorschot, C., Wingate, M.T.D. and Taylor, R.J. 2014. Proterozoic granulite formation driven by mafic magmatism: an example from the Fraser Range Metamorphics, Western Australia. *Precambrian Research*, **240**, 1–21, https://doi.org/10.1016/J.PRECAMRES.2013.07.024

Clark, C., Taylor, R.J.M., Johnson, T.E., Harley, S.L., Fitzsimons, I.C.W. and Oliver, L. 2019. Testing the fidelity of thermometers at ultrahigh temperatures. *Journal of Metamorphic Geology*, **37**, 917–934, https://doi.org/10.1111/jmg.12486

Clark, J.R. and Williams-Jones, A.E. 2004. *Rutile as a Potential Indicator Mineral for Metamorphosed Metallic Ore Deposits*. Rapport Final de DIVEX, Sous-projet SC2, Montréal, Canada.

Cochrane, R., Spikings, R.A. *et al*. 2014. High temperature (>350°C) thermochronology and mechanisms of Pb loss in apatite. *Geochimica et Cosmochimica Acta*, **127**, 39–56, https://doi.org/10.1016/j.gca.2013.11.028

Coleman, D.S., Gray, W. and Glazner, A.F. 2004. Rethinking the emplacement and evolution of zoned plutons: geochronologic evidence for incremental assembly of the Tuolumne Intrusive Suite, California. *Geology*, **32**, 433–436, https://doi.org/10.1130/G20220.1

Collins, W.J., Huang, H.-Q. and Jiang, X. 2016. Water-fluxed crustal melting produces Cordilleran batholiths. *Geology*, **44**, 143–146, https://doi.org/10.1130/G37398.1

Copeland, P., Parrish, R.R. and Harrison, T.M. 1988. Identification of inherited radiogenic Pb in monazite and its implications for U–Pb systematics. *Nature*, **333**, 760–763, https://doi.org/10.1038/333760a0

Corfu, F., Hanchar, J.M., Hoskin, P.W.O. and Kinny, P. 2003. Atlas of zircon textures. *Reviews in Mineralogy and Geochemistry*, **53**, 469–500, https://doi.org/10.2113/0530469

Corti, L., Zanoni, D., Gatta, G.D. and Zucali, M. 2020. Strain partitioning in host rock controls light rare earth element release from allanite-(Ce) in subduction zones. *Mineralogical Magazine*, **84**, 93–108, https://doi.org/10.1180/mgm.2020.4

Cox, M.A., Cavosie, A.J. *et al*. 2022. Impact and habitability scenarios for early Mars revisited based on a 4.45-Ga shocked zircon in regolith breccia. *Science Advances*, **8**, article eabl7497, https://doi.org/10.1126/sciadv.abl7497

Cross, A.J. 2009. *SHRIMP U–Pb Xenotime Geochronology and Its Application to Dating Mineralisation, Sediment Deposition and Metamorphism*. PhD thesis, Australian National University, https://doi.org/10.25911/5d778658a52a2

Crowe, D.E., Riciputi, L.R., Bezenek, S. and Ignatiev, A. 2001. Oxygen isotope and trace element zoning in hydrothermal garnets: windows into large-scale fluid-flow behavior. *Geology*, **29**, 479–482, https://doi.org/10.1130/0091-7613(2001)029<0479:OIATEZ>2.0.CO;2

Cruz-Uribe, A.M., Feineman, M.D., Zack, T. and Barth, M. 2014. Metamorphic reaction rates at ~650–800°C from diffusion of niobium in rutile. *Geochimica et*

Cosmochimica Acta, **130**, 63–77, https://doi.org/10.1016/j.gca.2013.12.015

Cutts, K.A., Hand, M., Kelsey, D.E., Wade, B., Strachan, R.A., Clark, C. and Netting, A. 2009. Evidence for 930 Ma metamorphism in the Shetland Islands, Scottish Caledonides: implications for Neoproterozoic tectonics in the Laurentia–Baltica sector of Rodinia. *Journal of the Geological Society, London*, **166**, 1033–1047, https://doi.org/10.1144/0016-76492009-006

Cutts, K.A., Kinny, P.D. *et al*. 2010. Three metamorphic events recorded in a single garnet: integrated phase modelling, *in situ* LA-ICPMS and SIMS geochronology from the Moine Supergroup, NW Scotland. *Journal of Metamorphic Geology*, **28**, 249–267, https://doi.org/10.1111/j.1525-1314.2009.00863.x

Cutts, K.A., Kelsey, D.E. and Hand, M. 2013. Evidence for late Paleoproterozoic (*ca* 1690–1665 Ma) high- to ultrahigh-temperature metamorphism in southern Australia: implications for Proterozoic supercontinent models. *Gondwana Research*, **23**, 617–640, https://doi.org/10.1016/j.gr.2012.04.009

Cutts, K.A., Stevens, G., Hoffmann, J.E., Buick, I.S., Frei, D. and Münker, C. 2014. Paleo- to Mesoarchean polymetamorphism in the Barberton Granite–Greenstone Belt, South Africa: constraints from U–Pb monazite and Lu–Hf garnet geochronology on the tectonic processes that shaped the belt. *GSA Bulletin*, **126**, 251–270, https://doi.org/10.1130/B30807.1

Cutts, K., Lana, C., Alkmim, F. and Peres, G.G. 2018. Metamorphic imprints on units of the southern Araçuaí belt, SE Brazil: the history of superimposed Transamazonian and Brasiliano orogenesis. *Gondwana Research*, **58**, 211–234, https://doi.org/10.1016/j.gr.2018.02.016

Cygan, R.T. and Lasaga, A.C. 1985. Self-diffusion of magnesium in garnet at 750 degrees to 900 degrees C. *American Journal of Science*, **285**, 328–350, https://doi.org/10.2475/ajs.285.4.328

Dachille, F., Simons, P.Y. and Roy, R. 1968. Pressure–temperature studies of anatase, brookite, rutile and TiO2-II. *American Mineralogist*, **53**, 1929–1939.

Darling, J.R., Storey, C.D. and Engi, M. 2012. Allanite U–Th–Pb geochronology by laser ablation ICPMS. *Chemical Geology*, **292**, 103–115, https://doi.org/10.1016/j.chemgeo.2011.11.012

Davis, D.W., Krogh, T.E. and Williams, I.S. 2003. Historical development of zircon geochronology. *Reviews in Mineralogy and Geochemistry*, **53**, 145–181, https://doi.org/10.2113/0530145

Decrée, S., Coint, N., Debaille, V., Hagen-Peter, G., Leduc, T. and Schiellerup, H. 2023. The potential for REEs in igneous-related apatite deposits in Europe. *Geological Society, London, Special Publications*, **526**, 2021–2175, https://doi.org/10.1144/SP526-2021-175

Degeling, H., Eggins, S. and Ellis, D. 2001. Zr budgets for metamorphic reactions, and the formation of zircon from garnet breakdown. *Mineralogical Magazine*, **65**, 749–758, https://doi.org/10.1180/002646101656006

Delavault, H., Dhuime, B., Hawkesworth, C.J., Cawood, P.A., Marschall, H. and the Edinburgh Ion Microprobe Facility 2016. Tectonic settings of continental crust formation: insights from Pb isotopes in feldspar inclusions in zircon. *Geology*, **44**, 819–822, https://doi.org/10.1130/G38117.1

Dempster, T.J., Coleman, S., Kennedy, R., Chung, P. and Brown, R.W. 2020. Growth zoning of garnet porphyroblasts: grain boundary and microtopographic controls. *Journal of Metamorphic Geology*, **38**, 1011–1027, https://doi.org/10.1111/jmg.12558

Deng, Z., Chaussidon, M., Guitreau, M., Puchtel, I.S., Dauphas, N. and Moynier, F. 2019. An oceanic subduction origin for Archaean granitoids revealed by silicon isotopes. *Nature Geoscience*, **12**, 774–778, https://doi.org/10.1038/s41561-019-0407-6

D'Errico, M., Lackey, J. *et al*. 2012. A detailed record of shallow hydrothermal fluid flow in the Sierra Nevada magmatic arc from low-$\delta^{18}O$ skarn garnets. *Geology*, **40**, 763–766, https://doi.org/10.1130/G33008.1

Dev, J.A., Tomson, J.K., Sorcar, N. and Nandakumar, V. 2021. Combined U–Pb/Hf isotopic studies and phase equilibrium modelling of HT–UHT metapelites from Kambam ultrahigh-temperature belt, South India: constraints on tectonothermal history of the terrane. *Lithos*, **406–407**, article 106531, https://doi.org/10.1016/j.lithos.2021.106531

Dhuime, B., Hawkesworth, C.J., Cawood, P.A. and Storey, C.D. 2012. A change in the geodynamics of continental growth 3 billion years ago. *Science*, **335**, 1334–1336, https://doi.org/10.1126/science.1216066

Di Rosa, M., Farina, F., Lanari, P. and Marroni, M. 2020. Pre-Alpine thermal history recorded in the continental crust from Alpine Corsica (France): evidence from zircon and allanite LA-ICP-MS dating. *Swiss Journal of Geosciences*, **113**, article 19, https://doi.org/10.1186/s00015-020-00374-2

Dodson, M.H. 1973. Closure temperature in cooling geochronological and petrological systems. *Contributions to Mineralogy and Petrology*, **40**, 259–274, https://doi.org/10.1007/BF00373790

Dohmen, R., Marschall, H.R., Ludwig, T. and Polednia, J. 2019. Diffusion of Zr, Hf, Nb and Ta in rutile: effects of temperature, oxygen fugacity, and doping level, and relation to rutile point defect chemistry. *Physics and Chemistry of Minerals*, **46**, 311–332, https://doi.org/10.1007/s00269-018-1005-7

Doucelance, R., Bruand, E., Matte, S., Bosq, C., Auclair, D. and Gannoun, A.-M. 2020. *In-situ* determination of Nd isotope ratios in apatite by LA-MC-ICPMS: challenges and limitations. *Chemical Geology*, **550**, article 119740, https://doi.org/10.1016/j.chemgeo.2020.119740

Dragovic, B., Samanta, L.M., Baxter, E.F. and Selverstone, J. 2012. Using garnet to constrain the duration and rate of water-releasing metamorphic reactions during subduction: an example from Sifnos, Greece. *Chemical Geology*, **314–317**, 9–22, https://doi.org/10.1016/j.chemgeo.2012.04.016

Dragovic, B., Baxter, E.F. and Caddick, M.J. 2015. Pulsed dehydration and garnet growth during subduction revealed by zoned garnet geochronology and thermodynamic modeling, Sifnos, Greece. *Earth and Planetary Science Letters*, **413**, 111–122, https://doi.org/10.1016/j.epsl.2014.12.024

Duan, Z., Gleeson, S.A., Gao, W.-S., Wang, F.-Y., Li, C.-J. and Li, J.-W. 2020. Garnet U–Pb dating of the Yinan Au–Cu skarn deposit, Luxi District, North China

Craton: implications for district-wide coeval Au–Cu and Fe skarn mineralization. *Ore Geology Reviews*, **118**, article 103310, https://doi.org/10.1016/j.oregeorev.2020.103310

Duchêne, S., Blichert-Toft, J., Luais, B., Télouk, P., Lardeaux, J.-M. and Albarède, F. 1997. The Lu–Hf dating of garnets and the ages of the Alpine high-pressure metamorphism. *Nature*, **387**, 586–589, https://doi.org/10.1038/42446

Duesterhoeft, E. and Lanari, P. 2020. Iterative thermodynamic modelling – part 1: a theoretical scoring technique and a computer program (Bingo-Antidote). *Journal of Metamorphic Geology*, **38**, 527–551, https://doi.org/10.1111/jmg.12538

Durgalakshmi, Sajeev, K. *et al*. 2021. The timing, duration and conditions of UHT metamorphism in remnants of the former eastern Gondwana. *Journal of Petrology*, **62**, article egab068, https://doi.org/10.1093/petrology/egab068

Dziggel, A., Wulff, K., Kolb, J., Meyer, F.M. and Lahaye, Y. 2009. Significance of oscillatory and bell-shaped growth zoning in hydrothermal garnet: evidence from the Navachab gold deposit, Namibia. *Chemical Geology*, **262**, 262–276, https://doi.org/10.1016/j.chemgeo.2009.01.027

El Korh, A., Schmidt, S.T., Ulianov, A. and Potel, S. 2009. Trace element partitioning in HP–LT metamorphic assemblages during subduction-related metamorphism, Ile de Groix, France: a detailed LA-ICPMS study. *Journal of Petrology*, **50**, 1107–1148, https://doi.org/10.1093/petrology/egp034

Emo, R.B., Smit, M.A. *et al*. 2018. Evidence for evolved Hadean crust from Sr isotopes in apatite within Eoarchean zircon from the Acasta Gneiss Complex. *Geochimica et Cosmochimica Acta*, **235**, 450–462, https://doi.org/10.1016/j.gca.2018.05.028

Engi, M. 2017. Petrochronology based on REE-minerals: monazite, allanite, xenotime, apatite. *Reviews in Mineralogy and Geochemistry*, **83**, 365–418, https://doi.org/10.2138/rmg.2017.83.12

Engi, M., Lanari, P. and Kohn, M.J. 2017. Significant ages – an introduction to petrochronology. *Reviews in Mineralogy and Geochemistry*, **83**, 1–12, https://doi.org/10.2138/rmg.2017.83.1

Evans, J. and Zalasiewicz, J. 1996. UPb, PbPb and SmNd dating of authigenic monazite: implications for the diagenetic evolution of the Welsh Basin. *Earth and Planetary Science Letters*, **144**, 421–433, https://doi.org/10.1016/S0012-821X(96)00177-X

Evans, T.P. 2004. A method for calculating effective bulk composition modification due to crystal fractionation in garnet-bearing schist: implications for isopleth thermobarometry. *Journal of Metamorphic Geology*, **22**, 547–557, https://doi.org/10.1111/j.1525-1314.2004.00532.x

Ewing, R.C., Meldrum, A., Wang, L., Weber, W.J. and Corrales, L.R. 2003. Radiation effects in zircon. *Reviews in Mineralogy and Geochemistry*, **53**, 387–425, https://doi.org/10.2113/0530387

Ewing, T.A. and Müntener, O. 2018. The mantle source of island arc magmatism during early subduction: evidence from Hf isotopes in rutile from the Jijal Complex (Kohistan arc, Pakistan). *Lithos*, **308–309**, 262–277, https://doi.org/10.1016/j.lithos.2018.03.005

Ewing, T.A., Rubatto, D., Eggins, S.M. and Hermann, J. 2011. *In situ* measurement of hafnium isotopes in rutile by LA-MC-ICPMS: protocol and applications. *Chemical Geology*, **281**, 72–82, https://doi.org/10.1016/j.chemgeo.2010.11.029

Ewing, T.A., Hermann, J. and Rubatto, D. 2013. The robustness of the Zr-in-rutile and Ti-in-zircon thermometers during high-temperature metamorphism (Ivrea–Verbano Zone, northern Italy). *Contributions to Mineralogy and Petrology*, **165**, 757–779, https://doi.org/10.1007/s00410-012-0834-5

Ewing, T.A., Rubatto, D. and Hermann, J. 2014. Hafnium isotopes and Zr/Hf of rutile and zircon from lower crustal metapelites (Ivrea–Verbano Zone, Italy): implications for chemical differentiation of the crust. *Earth and Planetary Science Letters*, **389**, 106–118, https://doi.org/10.1016/j.epsl.2013.12.029

Ewing, T.A., Rubatto, D., Beltrando, M. and Hermann, J. 2015. Constraints on the thermal evolution of the Adriatic margin during Jurassic continental break-up: U–Pb dating of rutile from the Ivrea–Verbano Zone, Italy. *Contributions to Mineralogy and Petrology*, **169**, 1–22, https://doi.org/10.1007/s00410-015-1135-6

Farias, P., Weinberg, R., Sola, A. and Becchio, R. 2020. From crustal thickening to orogen-parallel escape: the 120-myr-long HT–LP evolution recorded by titanite in the Paleozoic Famatinian Backarc, NW Argentina. *Tectonics*, **39**, article e2020TC006184, https://doi.org/10.1029/2020TC006184

Ferreira, J.A., Pereira, I., Bento dos Santos, T. and Mata, J. 2022. U–Pb age constraints on the protolith, cooling and exhumation of a Variscan middle crust migmatite complex from the Central Iberian Zone: insights into the Variscan metamorphic evolution and Ediacaran palaeogeographic implications. *Journal of the Geological Society*, **179**, jgs2021-072, https://doi.org/10.1144/jgs2021-072

Ferrero, S., Bartoli, O. *et al*. 2012. Microstructures of melt inclusions in anatectic metasedimentary rocks. *Journal of Metamorphic Geology*, **30**, 303–322, https://doi.org/10.1111/j.1525-1314.2011.00968.x

Ferrero, S., Wannhoff, I. *et al*. 2021. Embryos of TTGs in Gore Mountain garnet megacrysts from water-fluxed melting of the lower crust. *Earth and Planetary Science Letters*, **569**, article 117058, https://doi.org/10.1016/j.epsl.2021.117058

Ferry, J.M. and Spear, F. 1978. Experimental calibration of the partitioning of Fe and Mg between biotite and garnet. *Contributions to Mineralogy and Petrology*, **66**, 113–117, https://doi.org/10.1007/BF00372150

Ferry, J.M. and Watson, E.B. 2007. New thermodynamic models and revised calibrations for the Ti-in-zircon and Zr-in-rutile thermometers. *Contributions to Mineralogy and Petrology*, **154**, 429–437, https://doi.org/10.1007/s00410-007-0201-0

Fielding, I.O.H., Johnson, S.P. *et al*. 2017. Using *in situ* SHRIMP U–Pb monazite and xenotime geochronology to determine the age of orogenic gold mineralization: an example from the Paulsens mine, southern Pilbara Craton. *Economic Geology*, **112**, 1205–1230, https://doi.org/10.5382/econgeo.2017.4507

Finch, M., Weinberg, R., Barrote, V. and Cawood, P. 2021. Hf isotopic ratios in zircon reveal processes of anatexis and pluton construction. *Earth and Planetary Science*

Letters, **576**, article 117215, https://doi.org/10.1016/j.epsl.2021.117215

Finger, F. and Krenn, E. 2007. Three metamorphic monazite generations in a high-pressure rock from the Bohemian Massif and the potentially important role of apatite in stimulating polyphase monazite growth along a PT loop. *Lithos*, **95**, 103–115, https://doi.org/10.1016/j.lithos.2006.06.003

Fischer, S., Prave, A.R., Johnson, T.E., Cawood, P.A., Hawkesworth, C.J., Horstwood, M.S.A. and EIMF 2021. Using zircon in mafic migmatites to disentangle complex high-grade gneiss terrains – terrane spotting in the Lewisian complex, NW Scotland. *Precambrian Research*, **355**, article 106074, https://doi.org/10.1016/j.precamres.2020.106074

Fisher, C.M., McFarlane, C.R.M., Hanchar, J.M., Schmitz, M.D., Sylvester, P.J., Lam, R. and Longerich, H.P. 2011. Sm–Nd isotope systematics by laser ablation-multicollector-inductively coupled plasma mass spectrometry: methods and potential natural and synthetic reference materials. *Chemical Geology*, **284**, 1–20, https://doi.org/10.1016/j.chemgeo.2011.01.012

Fisher, C.M., Vervoort, J.D. and DuFrane, S.A. 2014*a*. Accurate Hf isotope determinations of complex zircons using the 'laser ablation split stream' method. *Geochemistry, Geophysics, Geosystems*, **15**, 121–139, https://doi.org/10.1002/2013GC004962

Fisher, C.M., Vervoort, J.D. and Hanchar, J.M. 2014*b*. Guidelines for reporting zircon Hf isotopic data by LA-MC-ICPMS and potential pitfalls in the interpretation of these data. *Chemical Geology*, **363**, 125–133, https://doi.org/10.1016/j.chemgeo.2013.10.019

Fisher, C.M., Hanchar, J.M., Miller, C.F., Phillips, S., Vervoort, J.D. and Whitehouse, M.J. 2017. Combining Nd isotopes in monazite and Hf isotopes in zircon to understand complex open-system processes in granitic magmas. *Geology*, **45**, 267–270, https://doi.org/10.1130/G38458.1

Fisher, C.M., Bauer, A.M. *et al*. 2020. Laser ablation split-stream analysis of the Sm–Nd and U–Pb isotope compositions of monazite, titanite, and apatite – improvements, potential reference materials, and application to the Archean Saglek Block gneisses. *Chemical Geology*, **539**, article 119493, https://doi.org/10.1016/j.chemgeo.2020.119493

Fletcher, I.R., McNaughton, N.J., Aleinikoff, J.A., Rasmussen, B. and Kamo, S.L. 2004. Improved calibration procedures and new standards for U–Pb and Th–Pb dating of Phanerozoic xenotime by ion microprobe. *Chemical Geology*, **209**, 295–314, https://doi.org/10.1016/j.chemgeo.2004.06.015

Flowerdew, M., Millar, I.L., Vaughan, A., Horstwood, M. and Fanning, C. 2006. The source of granitic gneisses and migmatites in the Antarctic Peninsula: a combined U–Pb SHRIMP and laser ablation Hf isotope study of complex zircons. *Contributions to Mineralogy and Petrology*, **151**, 751–768, https://doi.org/10.1007/s00410-006-0091-6

Foley, S., Tiepolo, M. and Vannucci, R. 2002. Growth of early continental crust controlled by melting of amphibolite in subduction zones. *Nature*, **417**, 837–840, https://doi.org/10.1038/nature00799

Fornelli, A., Langone, A., Micheletti, F., Pascazio, A. and Piccarreta, G. 2014. The role of trace element partitioning between garnet, zircon and orthopyroxene on the interpretation of zircon U–Pb ages: an example from high-grade basement in Calabria (southern Italy). *International Journal of Earth Sciences*, **103**, 487–507, https://doi.org/10.1007/s00531-013-0971-8

Fornelli, A., Langone, A., Micheletti, F. and Piccarreta, G. 2018. REE partition among zircon, orthopyroxene, amphibole and garnet in a high-grade metabasic system. *Geological Magazine*, **155**, 1705–1726, https://doi.org/10.1017/S001675681700067X

Förster, H.-J. 1998. The chemical composition of REE–Y–Th–U-rich accessory minerals in peraluminous granites of the Erzgebirge–Fichtelgebirge region, Germany, part I: the monazite-(Ce)-brabantite solid solution series. *American Mineralogist*, **83**, 259–272, https://doi.org/10.2138/am-1998-3-409

Fortier, S.M. and Giletti, B.J. 1989. An empirical model for predicting diffusion coefficients in silicate minerals. *Science*, **245**, 1481–1484, https://doi.org/10.1126/science.245.4925.1481

Foster, G., Gibson, H.D., Parrish, R., Horstwood, M., Fraser, J. and Tindle, A. 2002. Textural, chemical and isotopic insights into the nature and behaviour of metamorphic monazite. *Chemical Geology*, **191**, 183–207, https://doi.org/10.1016/S0009-2541(02)00156-0

Fougerouse, D., Kirkland, C.L., Saxey, D.W., Seydoux-Guillaume, A.-M., Rowles, M.R., Rickard, W.D.A. and Reddy, S.M. 2020. Nanoscale isotopic dating of monazite. *Geostandards and Geoanalytical Research*, **44**, 637–652, https://doi.org/10.1111/ggr.12340

Fougerouse, D., Cavosie, A.J. *et al*. 2021. A new method for dating impact events – thermal dependency on nanoscale Pb mobility in monazite shock twins. *Geochimica et Cosmochimica Acta*, **314**, 381–396, https://doi.org/10.1016/j.gca.2021.08.025

Fraser, G., Ellis, D. and Eggins, S. 1997. Zirconium abundance in granulite-facies minerals, with implications for zircon geochronology in high-grade rocks. *Geology*, **25**, 607–610, https://doi.org/10.1130/0091-7613(1997)025<0607:ZAIGFM>2.3.CO;2

Frost, B.R., Chamberlain, K.R. and Schumacher, J.C. 2001. Sphene (titanite): phase relations and role as a geochronometer. *Chemical Geology*, **172**, 131–148, https://doi.org/10.1016/S0009-2541(00)00240-0

Froude, D.O., Ireland, T.R., Kinny, P.D., Williams, I.S., Compston, W., Williams, I.R. and Myers, J.S. 1983. Ion microprobe identification of 4,100–4,200 Myr-old terrestrial zircons. *Nature*, **304**, 616–618, https://doi.org/10.1038/304616a0

Fu, B., Page, F.Z. *et al*. 2008. Ti-in-zircon thermometry: applications and limitations. *Contributions to Mineralogy and Petrology*, **156**, 197–215, https://doi.org/10.1007/s00410-008-0281-5

Fumes, R.A., Luvizotto, G.L. *et al*. 2022. Petrochronology of high-pressure granulite facies rocks from Southern Brasília Orogen, SE Brazil: combining quantitative compositional mapping, single-element thermometry and geochronology. *Journal of Metamorphic Geology*, **40**, 517–552, https://doi.org/10.1111/jmg.12637

Gaidies, F., de Capitani, C. and Abart, R. 2008. THERIA_G: a software program to numerically model prograde garnet growth. *Contributions to Mineralogy*

and Petrology, **155**, 657–671, https://doi.org/10.1007/s00410-007-0263-z

Gaidies, F., Morneau, Y.E., Petts, D.C., Jackson, S.E., Zagorevski, A. and Ryan, J.J. 2021. Major and trace element mapping of garnet: unravelling the conditions, timing and rates of metamorphism of the Snowcap assemblage, west–central Yukon. *Journal of Metamorphic Geology*, **39**, 133–164, https://doi.org/10.1111/jmg.12562

Ganguly, J. and Saxena, S.K. 1984. Mixing properties of aluminosilicate garnets: constraints from natural and experimental data, and applications to geothermobarometry. *American Mineralogist*, **69**, 88–97.

Gao, X.-Y., Zheng, Y.-F., Chen, Y.-X. and Guo, J. 2012. Geochemical and U–Pb age constraints on the occurrence of polygenetic titanites in UHP metagranite in the Dabie orogen. *Lithos*, **136–139**, 93–108, https://doi.org/10.1016/j.lithos.2011.03.020

Garber, J.M., Hacker, B.R., Kylander-Clark, A.R.C., Stearns, M. and Seward, G. 2017. Controls on trace element uptake in metamorphic titanite: implications for petrochronology. *Journal of Petrology*, **58**, 1031– 1057, https://doi.org/10.1093/petrology/egx046

Gardiner, N.J., Kirkland, C.L., Hollis, J., Szilas, K., Steenfelt, A., Yakymchuk, C. and Heide-Jørgensen, H. 2019. Building Mesoarchaean crust upon Eoarchaean roots: the Akia Terrane, West Greenland. *Contributions to Mineralogy and Petrology*, **174**, article 20, https://doi.org/10.1007/s00410-019-1554-x

George, F., Gaidies, F. and Boucher, B. 2018. Population-wide garnet growth zoning revealed by LA-ICP-MS mapping: implications for trace element equilibration and syn-kinematic deformation during crystallisation. *Contributions to Mineralogy and Petrology*, **173**, 1–22, https://doi.org/10.1007/s00410-018-1503-0

Gerdes, A. and Zeh, A. 2009. Zircon formation v. zircon alteration – new insights from combined U–Pb and Lu–Hf *in-situ* LA-ICP-MS analyses, and consequences for the interpretation of Archean zircon from the Central Zone of the Limpopo Belt. *Chemical Geology*, **261**, 230–243, https://doi.org/10.1016/j.chemgeo.2008.03.005

Gerrits, A.R., Inglis, E.C., Dragovic, B., Starr, P.G., Baxter, E.F. and Burton, K.W. 2019. Release of oxidizing fluids in subduction zones recorded by iron isotope zonation in garnet. *Nature Geoscience*, **12**, 1029–1033, https://doi.org/10.1038/s41561-019-0471-y

Gervasoni, F., Klemme, S., Rocha-Júnior, E.R.V. and Berndt, J. 2016. Zircon saturation in silicate melts: a new and improved model for aluminous and alkaline melts. *Contributions to Mineralogy and Petrology*, **171**, article 21, https://doi.org/10.1007/s00410-016-1227-y

Gevedon, M., Seman, S., Barnes, J.D., Lackey, J.S. and Stockli, D.F. 2018. Unraveling histories of hydrothermal systems via U–Pb laser ablation dating of skarn garnet. *Earth and Planetary Science Letters*, **498**, 237–246, https://doi.org/10.1016/j.epsl.2018.06.036

Ghent, E.D. 1976. Plagioclase–garnet–Al2SiO5–quartz; a potential geobarometer–geothermometer. *American Mineralogist*, **61**, 710–714.

Gieré, R. and Sorensen, S.S. 2004. Allanite and other REE-rich epidote-group minerals. *Reviews in Mineralogy and Geochemistry*, **56**, 431–493, https://doi.org/10.2138/gsrmg.56.1.431

Gillespie, J., Kinny, P.D., Kirkland, C.L., Martin, L., Nemchin, A.A., Cavosie, A.J. and Hasterok, D. 2021. Isotopic modelling of Archean crustal evolution from comagmatic zircon–apatite pairs. *Earth and Planetary Science Letters*, **575**, article 117194, https://doi.org/10.1016/j.epsl.2021.117194

Gillespie, J., Kirkland, C.L., Kinny, P.D., Simpson, A., Glorie, S. and Rankenburg, K. 2022. Lu–Hf, Sm–Nd, and U–Pb isotopic coupling and decoupling in apatite. *Geochimica et Cosmochimica Acta*, **338**, 121–135, https://doi.org/10.1016/j.gca.2022.09.038

Giuntoli, F., Lanari, P., Burn, M., Kunz, B.E. and Engi, M. 2018. Deeply subducted continental fragments – part 2: insight from petrochronology in the central Sesia Zone (western Italian Alps). *Solid Earth*, **9**, 191–222, https://doi.org/10.5194/se-9-191-2018

Glorie, S., Gillespie, J. *et al*. 2022. Detrital apatite Lu–Hf and U–Pb geochronology applied to the southwestern Siberian margin. *Terra Nova*, **34**, 201–209, https://doi.org/10.1111/ter.12580

Glorie, S. *et al*. 2023. Robust laser ablation Lu–Hf dating of apatite: an empirical evaluation. *Geological Society, London, Special Publications*, **537**, https://doi.org/10.1144/SP537-2022-205

Godet, A., Raimondo, T. and Guilmette, C. 2022. Atoll garnet: insights from LA-ICP-MS trace element mapping. *Contributions to Mineralogy and Petrology*, **177**, article 57, https://doi.org/10.1007/s00410-022-01924-7

Gonçalves, G.O., Lana, C., Buick, I.S., Alkmim, F.F., Scholz, R. and Queiroga, G. 2019. Twenty million years of post-orogenic fluid production and hydrothermal mineralization across the external Araçuaí orogen and adjacent São Francisco craton, SE Brazil. *Lithos*, **342–343**, 557–572, https://doi.org/10.1016/j.lithos.2019.04.022

Gonzalez, J.P., Thomas, J.B., Baldwin, S.L. and Alvaro, M. 2019. Quartz-in-garnet and Ti-in-quartz thermobarometry: methodology and first application to a quartzofeldspathic gneiss from eastern Papua New Guinea. *Journal of Metamorphic Geology*, **37**, 1193–1208, https://doi.org/10.1111/jmg.12508

Gonzalez, J.P., Mazzucchelli, M.L., Angel, R.J. and Alvaro, M. 2021. Elastic geobarometry for anisotropic inclusions in anisotropic host minerals: quartz-in-zircon. *Journal of Geophysical Research: Solid Earth*, **126**, article e2021JB022080, https://doi.org/10.1029/2021JB022080

Goodenough, K.M., Crowley, Q.G., Krabbendam, M. and Parry, S.F. 2013. New U–Pb age constraints for the Laxford Shear Zone, NW Scotland: evidence for tectono-magmatic processes associated with the formation of a Paleoproterozoic supercontinent. *Precambrian Research*, **233**, 1–19, https://doi.org/10.1016/j.precamres.2013.04.010

Gordon, S.M., Kirkland, C.L. *et al*. 2021. Deformation-enhanced recrystallization of titanite drives decoupling between U–Pb and trace elements. *Earth and Planetary Science Letters*, **560**, article 116810, https://doi.org/10.1016/j.epsl.2021.116810

Goudie, D.J., Fisher, C.M., Hanchar, J.M., Crowley, J.L. and Ayers, J.C. 2014. Simultaneous *in situ* determination of U–Pb and Sm–Nd isotopes in monazite by

laser ablation ICP-MS. *Geochemistry, Geophysics, Geosystems*, **15**, 2575–2600, https://doi.org/10.1002/2014GC005431

Gratz, R. and Heinrich, W. 1997. Monazite–xenotime thermobarometry: experimental calibration of the miscibility gap in the binary system $CePO_4$–YPO_4. *American Mineralogist*, **82**, 772–780, https://doi.org/10.2138/am-1997-7-816

Gratz, R. and Heinrich, W. 1998. Monazite–xenotime thermometry. III. Experimental calibration of the partitioning of gadolinium between monazite and xenotime. *European Journal of Mineralogy*, **10**, 579–588, https://doi.org/10.1127/ejm/10/3/0579

Green, E.C.R., White, R.W., Diener, J.F.A., Powell, R., Holland, T.J.B. and Palin, R.M. 2016. Activity–composition relations for the calculation of partial melting equilibria in metabasic rocks. *Journal of Metamorphic Geology*, **34**, 845–869, https://doi.org/10.1111/jmg.12211

Gregory, C.J., Rubatto, D., Allen, C.M., Williams, I.S., Hermann, J. and Ireland, T. 2007. Allanite microgeochronology: a LA-ICP-MS and SHRIMP U–Th–Pb study. *Chemical Geology*, **245**, 162–182, https://doi.org/10.1016/j.chemgeo.2007.07.029

Gregory, C.J., Rubatto, D., Hermann, J., Berger, A. and Engi, M. 2012. Allanite behaviour during incipient melting in the southern Central Alps. *Geochimica et Cosmochimica Acta*, **84**, 433–458, https://doi.org/10.1016/j.gca.2012.01.020

Grimes, C.B., John, B.E. *et al*. 2007. Trace element chemistry of zircons from oceanic crust: a method for distinguishing detrital zircon provenance. *Geology*, **35**, 643–646, https://doi.org/10.1130/G23603A.1

Grimes, C.B., Wooden, J.L., Cheadle, M.J. and John, B.E. 2015. 'Fingerprinting' tectono-magmatic provenance using trace elements in igneous zircon. *Contributions to Mineralogy and Petrology*, **170**, 1–26.

Gualda, G.A.R., Ghiorso, M.S., Lemons, R.V. and Carley, T.L. 2012. Rhyolite-MELTS: a modified calibration of MELTS optimized for silica-rich, fluid-bearing magmatic systems. *Journal of Petrology*, **53**, 875–890, https://doi.org/10.1093/petrology/egr080

Gudelius, D., Zeh, A., Almeev, R.R., Wilson, A.H., Fischer, L.A. and Schmitt, A.K. 2020. Zircon melt inclusions in mafic and felsic rocks of the Bushveld Complex – constraints for zircon crystallization temperatures and partition coefficients. *Geochimica et Cosmochimica Acta*, **289**, 158–181, https://doi.org/10.1016/j.gca.2020.08.027

Guitreau, M. and Flahaut, J. 2019. Record of low-temperature aqueous alteration of Martian zircon during the late Amazonian. *Nature Communications*, **10**, 1–9, https://doi.org/10.1038/s41467-019-10382-y

Guitreau, M., Blichert-Toft, J., Martin, H., Mojzsis, S.J. and Albarède, F. 2012. Hafnium isotope evidence from Archean granitic rocks for deep-mantle origin of continental crust. *Earth and Planetary Science Letters*, **337**, 211–223, https://doi.org/10.1016/j.epsl.2012.05.029

Guitreau, M., Mora, N. and Paquette, J. 2018. Crystallization and disturbance histories of single zircon crystals from Hadean–Eoarchean Acasta gneisses examined by LA-ICP-MS U–Pb traverses. *Geochemistry, Geophysics, Geosystems*, **19**, 272–291, https://doi.org/10.1002/2017GC007310

Guitreau, M., Boyet, M. *et al*. 2019. Hadean protocrust reworking at the origin of the Archean Napier Complex (Antarctica). *Geochemical Perspectives Letters*, **12**, 7–11, https://doi.org/10.7185/geochemlet.1927

Guitreau, M., Gannoun, A., Deng, Z., Marin-Carbonne, J., Chaussidon, M. and Moynier, F. 2020. Silicon isotope measurement in zircon by laser ablation multiple collector inductively coupled plasma mass spectrometry. *Journal of Analytical Atomic Spectrometry*, **35**, 1597–1606, https://doi.org/10.1039/D0JA00214C

Guitreau, M., Gannoun, A., Deng, Z., Chaussidon, M., Moynier, F., Barbarin, B. and Marin-Carbonne, J. 2022. Stable isotope geochemistry of silicon in granitoid zircon. *Geochimica et Cosmochimica Acta*, **316**, 273–294, https://doi.org/10.1016/j.gca.2021.09.029

Guo, J.-L., Wang, Z., Zhang, W., Moynier, F., Cui, D., Hu, Z. and Ducea, M.N. 2020. Significant Zr isotope variations in single zircon grains recording magma evolution history. *Proceedings of the National Academy of Sciences of the USA*, **117**, 21125–21131, https://doi.org/10.1073/pnas.2002053117

Gutieva, L., Dziggel, A., Volante, S. and Johnson, T. 2021. Zircon U–Pb and Lu–Hf record from the Archean Lewisian Gneiss Complex, NW Scotland. *Goldschmidt Conference 2021*, 4–9 July 2021, virtual event, https://doi.org/10.7185/gold2021.4082

Hacker, B.R., Kylander-Clark, A.R., Holder, R., Andersen, T.B., Peterman, E.M., Walsh, E.O. and Munnikhuis, J.K. 2015. Monazite response to ultrahigh-pressure subduction from U–Pb dating by laser ablation split stream. *Chemical Geology*, **409**, 28–41, https://doi.org/10.1016/j.chemgeo.2015.05.008

Hacker, B., Kylander-Clark, A. and Holder, R. 2019. REE partitioning between monazite and garnet: implications for petrochronology. *Journal of Metamorphic Geology*, **37**, 227–237, https://doi.org/10.1111/jmg.12458

Hagen-Peter, G., Cottle, J.M., Smit, M. and Cooper, A.F. 2016. Coupled garnet Lu–Hf and monazite U–Pb geochronology constrain early convergent margin dynamics in the Ross orogen, Antarctica. *Journal of Metamorphic Geology*, **34**, 293–319, https://doi.org/10.1111/jmg.12182

Hallett, B.W. and Spear, F.S. 2015. Monazite, zircon, and garnet growth in migmatitic pelites as a record of metamorphism and partial melting in the East Humboldt Range, Nevada. *American Mineralogist*, **100**, 951–972, https://doi.org/10.2138/am-2015-4839

Hammerli, J. and Kemp, T.I.S. 2021. Combined Hf and Nd isotope microanalysis of co-existing zircon and REE-rich accessory minerals: high resolution insights into crustal processes. *Chemical Geology*, **581**, article 120393, https://doi.org/10.1016/j.chemgeo.2021.120393

Hammerli, J., Kemp, A.I.S. and Spandler, C. 2014. Neodymium isotope equilibration during crustal metamorphism revealed by *in situ* microanalysis of REE-rich accessory minerals. *Earth and Planetary Science Letters*, **392**, 133–142, https://doi.org/10.1016/j.epsl.2014.02.018

Hammerli, J., Kemp, A.I.S. and Whitehouse, M.J. 2019. *In situ* trace element and Sm–Nd isotope analysis of accessory minerals in an Eoarchean tonalitic gneiss from Greenland: implications for Hf and Nd isotope decoupling in Earth's ancient rocks. *Chemical Geology*,

524, 394–405, https://doi.org/10.1016/j.chemgeo.2019.06.025

Hanchar, J.M. and Miller, C.F. 1993. Zircon zonation patterns as revealed by cathodoluminescence and backscattered electron images: implications for interpretation of complex crustal histories. *Chemical Geology*, **110**, 1–13, https://doi.org/10.1016/0009-2541(93)90244-D

Harley, S.L. 2008. Refining the P–T records of UHT crustal metamorphism. *Journal of Metamorphic Geology*, **26**, 125–154, https://doi.org/10.1111/j.1525-1314.2008.00765.x

Harley, S.L. 2016. A matter of time: the importance of the duration of UHT metamorphism. *Journal of Mineralogical and Petrological Sciences*, **111**, 50–72, https://doi.org/10.2465/jmps.160128

Harley, S.L. and Kelly, N.M. 2007. The impact of zircon–garnet REE distribution data on the interpretation of zircon U–Pb ages in complex high-grade terrains: an example from the Rauer Islands, East Antarctica. *Chemical Geology*, **241**, 62–87, https://doi.org/10.1016/j.chemgeo.2007.02.011

Harley, S.L. and Nandakumar, V. 2014. Accessory mineral behaviour in granulite migmatites: a case study from the Kerala Khondalite Belt, India. *Journal of Petrology*, **55**, 1965–2002, https://doi.org/10.1093/petrology/egu047

Harley, S.L., Kinny, P., Snape, I. and Black, L.P. 2001. Zircon chemistry and the definition of events in Archaean granulite terrains. *Extended Abstracts of the 4th International Archaean Symposium*, 24–28 September, Perth, Australia. AGSO-Geoscience Australia, 511–513.

Harlov, D.E. 2015. Apatite: a fingerprint for metasomatic processes. *Elements*, **11**, 171–176, https://doi.org/10.2113/gselements.11.3.171

Harlov, D.E. and Hetherington, C.J. 2010. Partial high-grade alteration of monazite using alkali-bearing fluids: experiment and nature. *American Mineralogist*, **95**, 1105–1108, https://doi.org/10.2138/am.2010.3525

Harlov, D.E., Wirth, R. and Hetherington, C.J. 2011. Fluid-mediated partial alteration in monazite: the role of coupled dissolution–reprecipitation in element redistribution and mass transfer. *Contributions to Mineralogy and Petrology*, **162**, 329–348, https://doi.org/10.1007/s00410-010-0599-7

Harris, C. and Vogeli, J. 2010. Oxygen isotope composition of garnet in the Peninsula Granite, Cape Granite Suite, South Africa: constraints on melting and emplacement mechanisms. *South African Journal of Geology*, **113**, 401–412, https://doi.org/10.2113/gssajg.113.4.401

Harrison, T.M. and Watson, E.B. 1984. The behavior of apatite during crustal anatexis: equilibrium and kinetic considerations. *Geochimica et Cosmochimica Acta*, **48**, 1467–1477, https://doi.org/10.1016/0016-7037(84)90403-4

Hart, E., Storey, C., Harley, S.L. and Fowler, M. 2018. A window into the lower crust: trace element systematics and the occurrence of inclusions/intergrowths in granulite-facies rutile. *Gondwana Research*, **59**, 76–86, https://doi.org/10.1016/j.gr.2018.02.021

Hartnady, M.I.H., Kirkland, C.L., Clark, C., Spaggiari, C.V., Smithies, R.H., Evans, N.J. and McDonald, B.J. 2019. Titanite dates crystallization: slow Pb diffusion during super-solidus re-equilibration. *Journal of Metamorphic Geology*, **37**, 823–838, https://doi.org/10.1111/jmg.12489

Hayden, L.A., Watson, E.B. and Wark, D.A. 2008. A thermobarometer for sphene (titanite). *Contributions to Mineralogy and Petrology*, **155**, 529–540, https://doi.org/10.1007/s00410-007-0256-y

Heinrich, W., Rehs, G. and Franz, G. 1997. Monazite–xenotime miscibility gap thermometry. I. An empirical calibration. *Journal of Metamorphic Geology*, **15**, 3–16, https://doi.org/10.1111/j.1525-1314.1997.t01-1-00052.x

Henrichs, I.A., O'Sullivan, G., Chew, D.M., Mark, C., Babechuk, M.G., McKenna, C. and Emo, R. 2018. The trace element and U–Pb systematics of metamorphic apatite. *Chemical Geology*, **483**, 218–238, https://doi.org/10.1016/j.chemgeo.2017.12.031

Henrichs, I.A., Chew, D.M., O'Sullivan, G.J., Mark, C., McKenna, C. and Guyett, P. 2019. Trace element (Mn–Sr–Y–Th–REE) and U–Pb isotope systematics of metapelitic apatite during progressive greenschist- to amphibolite-facies Barrovian metamorphism. *Geochemistry, Geophysics, Geosystems*, **20**, 4103–4129, https://doi.org/10.1029/2019GC008359

Hermann, J. 2002. Allanite: thorium and light rare earth element carrier in subducted crust. *Chemical Geology*, **192**, 289–306, https://doi.org/10.1016/S0009-2541(02)00222-X

Hermann, J. and Rubatto, D. 2003. Relating zircon and monazite domains to garnet growth zones: age and duration of granulite facies metamorphism in the Val Malenco lower crust. *Journal of Metamorphic Geology*, **21**, 833–852, https://doi.org/10.1046/j.1525-1314.2003.00484.x

Hermann, J. and Rubatto, D. 2009. Accessory phase control on the trace element signature of sediment melts in subduction zones. *Chemical Geology*, **265**, 512–526, https://doi.org/10.1016/j.chemgeo.2009.05.018

Hermann, J. and Rubatto, D. 2014. Subduction of continental crust to mantle depth: geochemistry of ultrahigh-pressure rocks. *In*: Holland, H.D. and Turekian, K.K. (eds) *Treatise on Geochemistry*. 2nd edn, 309–340, https://doi.org/10.1016/B978-0-08-095975-7.00309-0.

Hoffmann, J.E., Münker, C., Polat, A., Rosing, M.T. and Schulz, T. 2011. The origin of decoupled Hf–Nd isotope compositions in Eoarchean rocks from southern West Greenland. *Geochimica et Cosmochimica Acta*, **75**, 6610–6628, https://doi.org/10.1016/j.gca.2011.08.018

Hofmann, A.E., Baker, M.B. and Eiler, J.M. 2013. An experimental study of Ti and Zr partitioning among zircon, rutile, and granitic melt. *Contributions to Mineralogy and Petrology*, **166**, 235–253, https://doi.org/10.1007/s00410-013-0873-6

Högdahl, K., Majka, J., Sjöström, H., Nilsson, K.P., Claesson, S. and Konečný, P. 2012. Reactive monazite and robust zircon growth in diatexites and leucogranites from a hot, slowly cooled orogen: implications for the Palaeoproterozoic tectonic evolution of the central Fennoscandian Shield, Sweden. *Contributions to Mineralogy and Petrology*, **163**, 167–188, https://doi.org/10.1007/s00410-011-0664-x

Hokada, T. and Harley, S.L. 2004. Zircon growth in UHT leucosome: constraints from zircon-garnet rare earth elements (REE) relations in Napier Complex, East Antarctica. *Journal of Mineralogical and Petrological*

Sciences, **99**, 180–190, https://doi.org/10.2465/jmps.99.180

Holdaway, M. 2001. Recalibration of the GASP geobarometer in light of recent garnet and plagioclase activity models and versions of the garnet-biotite geothermometer. *American Mineralogist*, **86**, 1117–1129, https://doi.org/10.2138/am-2001-1001

Holder, R.M. and Hacker, B.R. 2019. Fluid-driven resetting of titanite following ultrahigh-temperature metamorphism in southern Madagascar. *Chemical Geology*, **504**, 38–52, https://doi.org/10.1016/j.chemgeo.2018.11.017

Holder, R.M., Hacker, B.R. and Kylander-Clark, A.R. 2013. Monazite petrochronology from the UHP Western Gneiss region, Norway. *American Geophysical Union Fall Meeting*, 9–13 December 2013, San Francisco, CA, Abstracts, *2013AGUFM. V23A2759H.*

Holder, R.M., Hacker, B.R., Seward, G.G.E. and Kylander-Clark, A.R.C. 2019. Interpreting titanite U–Pb dates and Zr thermobarometry in high-grade rocks: empirical constraints on elemental diffusivities of Pb, Al, Fe, Zr, Nb, and Ce. *Contributions to Mineralogy and Petrology*, **174**, article 42, https://doi.org/10.1007/s00410-019-1578-2

Holder, R.M., Yakymchuk, C. and Viete, D.R. 2020. Accessory mineral Eu anomalies in suprasolidus rocks: beyond feldspar. *Geochemistry, Geophysics, Geosystems*, **21**, article e2020GC009052, https://doi.org/10.1029/2020GC009052

Holland, H.D. and Gottfried, D. 1955. The effect of nuclear radiation on the structure of zircon. *Acta Crystallographica*, **8**, 291–300, https://doi.org/10.1107/S0365110X55000947

Holland, T.J.B. and Powell, R. 1990. An enlarged and updated internally consistent thermodynamic dataset with uncertainties and correlations: the system K_2O–Na_2O–CaO–MgO–MnO–FeO–Fe_2O_3–Al_2O_3–TiO_2–SiO_2–C–H_2–O_2. *Journal of Metamorphic Geology*, **8**, 89–124, https://doi.org/10.1111/j.1525-1314.1990.tb00458.x

Holland, T.J.B. and Powell, R. 1998. An internally consistent thermodynamic data set for phases of petrological interest. *Journal of Metamorphic Geology*, **16**, 309–344, https://doi.org/10.1111/j.1525-1314.1998.00140.x

Holland, T.J.B. and Powell, R. 2011. An improved and extended internally consistent thermodynamic dataset for phases of petrological interest, involving a new equation of state for solids. *Journal of Metamorphic Geology*, **29**, 333–383, https://doi.org/10.1111/j.1525-1314.2010.00923.x

Hollister, L.S. 1966. Garnet zoning: an interpretation based on the Rayleigh fractionation model. *Science*, **154**, 1647–1651, https://doi.org/10.1126/science.154.3757.1647

Holtmann, R., Muñoz-Montecinos, J. *et al.* 2022. Cretaceous thermal evolution of the closing Neo-Tethyan realm revealed by multi-method petrochronology. *Lithos*, **422–423**, 106731, https://doi.org/10.1016/j.lithos.2022.106731

Hoover, W.F., Penniston-Dorland, S.C., Baumgartner, L.P., Bouvier, A.-S., Baker, D., Dragovic, B. and Gion, A. 2021. A method for secondary ion mass spectrometry measurement of lithium isotopes in garnet: the utility of glass reference materials. *Geostandards and Geoanalytical Research*, **45**, 477–499, https://doi.org/10.1111/ggr.12383

Hoover, W.F., Penniston-Dorland, S. *et al.* 2022. Episodic fluid flow in an eclogite-facies shear zone: insights from Li isotope zoning in garnet. *Geology*, **50**, 746–750, https://doi.org/10.1130/G49737.1

Hopkins, M., Harrison, T.M. and Manning, C.E. 2008. Low heat flow inferred from >4 Gyr zircons suggests Hadean plate boundary interactions. *Nature*, **456**, 493–496, https://doi.org/10.1038/nature07465

Horton, F., Holder, R.M. and Swindle, C.R. 2022. An extensive record of orogenesis recorded in a Madagascar granulite. *Journal of Metamorphic Geology*, **40**, 287–305, https://doi.org/10.1111/jmg.12628.

Hoschek, G. 2016. Phase relations of the REE minerals florencite, allanite and monazite in quartzitic garnet–kyanite schist of the Eclogite Zone, Tauern Window, Austria. *European Journal of Mineralogy*, **28**, 735–750.

Hoshino, M., Kimata, M., Arakawa, Y., Shimizu, M., Nishida, N. and Nakai, S. 2007. Allanite-(Ce) as an indicator of the origin of granitic rocks in Japan: importance of Sr–Nd isotopic and chemical composition. *The Canadian Mineralogist*, **45**, 1329–1336, https://doi.org/10.3749/canmin.45.6.1329

Hoskin, P.W.O. and Black, L.P. 2000. Metamorphic zircon formation by solid-state recrystallization of protolith igneous zircon. *Journal of Metamorphic Geology*, **18**, 423–439, https://doi.org/10.1046/j.1525-1314.2000.00266.x

Hoskin, P.W.O. and Schaltegger, U. 2003. The composition of zircon and igneous and metamorphic petrogenesis. *Reviews in Mineralogy and Geochemistry*, **53**, 27–62, https://doi.org/10.2113/0530027

Humphries, F.J. and Cliff, R.A. 1982. Sm–Nd dating and cooling history of Scourian granulites, Sutherland. *Nature*, **295**, 515–517, https://doi.org/10.1038/295515a0

Ibañez-Mejia, M. and Tissot, F.L. 2019. Extreme Zr stable isotope fractionation during magmatic fractional crystallization. *Science Advances*, **5**, article eaax8648, https://doi.org/10.1126/sciadv.aax8648

Ihlen, P.M., Schiellerup, H., Gautneb, H. and Skår, Ø. 2014. Characterization of apatite resources in Norway and their REE potential – a review. *Ore Geology Reviews*, **58**, 126–147, https://doi.org/10.1016/j.oregeorev.2013.11.003

Iizuka, T., Hirata, T., Komiya, T., Rino, S., Katayama, I., Motoki, A. and Maruyama, S. 2005. U–Pb and Lu–Hf isotope systematics of zircons from the Mississippi River sand: implications for reworking and growth of continental crust. *Geology*, **33**, 485–488, https://doi.org/10.1130/G21427.1

Iizuka, T., Campbell, I.H., Allen, C.M., Gill, J.B., Maruyama, S. and Makoka, F. 2013. Evolution of the African continental crust as recorded by U–Pb, Lu–Hf and O isotopes in detrital zircons from modern rivers. *Geochimica et Cosmochimica Acta*, **107**, 96–120, https://doi.org/10.1016/j.gca.2012.12.028

Iizuka, T., Yamaguchi, T., Hibiya, Y. and Amelin, Y. 2015. Meteorite zircon constraints on the bulk Lu−Hf isotope composition and early differentiation of the Earth. *Proceedings of the National Academy of Sciences of the*

USA, **112**, 5331–5336, https://doi.org/10.1073/pnas.1501658112

Itano, K., Ueki, K., Iizuka, T. and Kuwatani, T. 2020. Geochemical discrimination of monazite source rock based on machine learning techniques and multinomial logistic regression analysis. *Geosciences*, **10**, article 63, https://doi.org/10.3390/geosciences10020063

Jaffey, A., Flynn, K., Glendenin, L., Bentley, W.T. and Essling, A. 1971. Precision measurement of half-lives and specific activities of ^{235}U and ^{238}U. *Physical Review C*, **4**, article 1889, https://doi.org/10.1103/PhysRevC.4.1889

Jamieson, J.C. and Olinger, B. 1969. Pressure–temperature studies of anatase, brookite rutile, and Ti02(II): a discussion. *American Mineralogist*, **54**, 1477–1481.

Janots, E. and Rubatto, D. 2014. U–Th–Pb dating of collision in the external Alpine domains (Urseren zone, Switzerland) using low temperature allanite and monazite. *Lithos*, **184–187**, 155–166, https://doi.org/10.1016/j.lithos.2013.10.036

Janots, E., Negro, F., Brunet, F., Goffé, B., Engi, M. and Bouybaouène, M.L. 2006. Evolution of the REE mineralogy in HP–LT metapelites of the Sebtide Complex, Rif, Morocco: monazite stability and geochronology. *Lithos*, **87**, 214–234, https://doi.org/10.1016/j.lithos.2005.06.008

Janots, E., Brunet, F., Goffé, B., Poinssot, C., Burchard, M. and Cemič, L. 2007. Thermochemistry of monazite-(La) and dissakisite-(La): implications for monazite and allanite stability in metapelites. *Contributions to Mineralogy and Petrology*, **154**, 1–14, https://doi.org/10.1007/s00410-006-0176-2

Janots, E., Engi, M., Berger, A., Allaz, J., Schwarz, J. and Spandler, C. 2008. Prograde metamorphic sequence of REE minerals in pelitic rocks of the Central Alps: implications for allanite–monazite–xenotime phase relations from 250 to 610°C. *Journal of Metamorphic Geology*, **26**, 509–526, https://doi.org/10.1111/j.1525-1314.2008.00774.x

Janots, E., Engi, M., Rubatto, D., Berger, A., Gregory, C. and Rahn, M. 2009. Metamorphic rates in collisional orogeny from *in situ* allanite and monazite dating. *Geology*, **37**, 11–14, https://doi.org/10.1130/G25192A.1

Janots, E., Berger, A. and Engi, M. 2011. Physico-chemical control on the REE minerals in chloritoid-grade metasediments from a single outcrop (Central Alps, Switzerland). *Lithos*, **121**, 1–11, https://doi.org/10.1016/j.lithos.2010.08.023

Jayananda, M., Chardon, D., Peucat, J.-J. and Fanning, C.M. 2015. Paleo- to Mesoarchean TTG accretion and continental growth in the western Dharwar craton, southern India: constraints from SHRIMP U–Pb zircon geochronology, whole-rock geochemistry and Nd–Sr isotopes. *Precambrian Research*, **268**, 295–322, https://doi.org/10.1016/j.precamres.2015.07.015

Jennings, E.S., Marschall, H., Hawkesworth, C. and Storey, C. 2011. Characterization of magma from inclusions in zircon: apatite and biotite work well, feldspar less so. *Geology*, **39**, 863–866, https://doi.org/10.1130/G32037.1

Jiao, S., Fitzsimons, I.C.W., Zi, J.-W., Evans, N.J., Mcdonald, B.J. and Guo, J. 2020*a*. Texturally controlled U–Th–Pb monazite geochronology reveals Paleoproterozoic UHT metamorphic evolution in the Khondalite Belt, North China Craton. *Journal of Petrology*, **61**, article egaa023, https://doi.org/10.1093/petrology/egaa023

Jiao, S., Guo, J., Evans, N.J., Mcdonald, B.J., Liu, P., Ouyang, D. and Fitzsimons, I.C.W. 2020*b*. The timing and duration of high-temperature to ultrahigh-temperature metamorphism constrained by zircon U–Pb–Hf and trace element signatures in the Khondalite Belt, North China Craton. *Contributions to Mineralogy and Petrology*, **175**, article 66, https://doi.org/10.1007/s00410-020-01706-z

Jiao, S., Evans, N.J., Mitchell, R.N., Fitzsimons, I.C.W. and Guo, J. 2021. Heavy rare-earth element and Y partitioning between monazite and garnet in aluminous granulites. *Contributions to Mineralogy and Petrology*, **176**, article 50, https://doi.org/10.1007/s00410-021-01808-2

John, T., Klemd, R., Klemme, S., Pfänder, J.A., Elis Hoffmann, J. and Gao, J. 2011. Nb–Ta fractionation by partial melting at the titanite–rutile transition. *Contributions to Mineralogy and Petrology*, **161**, 35–45, https://doi.org/10.1007/s00410-010-0520-4

Johnson, S.E. 1999. Porphyroblast microstructures: a review of current and future trends. *American Mineralogist*, **84**, 1711–1726, https://doi.org/10.2138/am-1999-11-1202

Johnson, T.A., Vervoort, J.D., Ramsey, M.J., Aleinikoff, J.N. and Southworth, S. 2018. Constraints on the timing and duration of orogenic events by combined Lu–Hf and Sm–Nd geochronology: an example from the Grenville orogeny. *Earth and Planetary Science Letters*, **501**, 152–164, https://doi.org/10.1016/j.epsl.2018.08.030

Jonnalagadda, M.K., Karmalkar, N.R., Duraiswami, R.A., Harshe, S., Gain, S. and Griffin, W.L. 2017. Formation of atoll garnets in the UHP eclogites of the Tso Morari Complex, Ladakh, Himalaya. *Journal of Earth System Science*, **126**, article 107, https://doi.org/10.1007/s12040-017-0887-y

Joseph, C., Fougerouse, D., Saxey, D.W., Verberne, R., Reddy, S.M. and Rickard, W.D.A. 2021. Xenotime at the nanoscale: U–Pb geochronology and optimisation of analyses by atom probe tomography. *Geostandards and Geoanalytical Research*, **45**, 443–456, https://doi.org/10.1111/ggr.12398

Kamber, B.S., Frei, R. and Gibb, A.J. 1998. Pitfalls and new approaches in granulite chronometry: an example from the Limpopo Belt, Zimbabwe. *Precambrian Research*, **91**, 269–285, https://doi.org/10.1016/S0301-9268(98)00053-9

Kamenetsky, V.S., Doroshkevich, A.G., Elliott, H.A.L. and Zaitsev, A.N. 2021. Carbonatites: contrasting, complex, and controversial. *Elements*, **17**, 307–314, https://doi.org/10.2138/gselements.17.5.307

Kapp, P., Manning, C.E. and Tropper, P. 2009. Phase-equilibrium constraints on titanite and rutile activities in mafic epidote amphibolites and geobarometry using titanite–rutile equilibria. *Journal of Metamorphic Geology*, **27**, 509–521, https://doi.org/10.1111/j.1525-1314.2009.00836.x

Karioris, F., Gowda, K.A. and Cartz, L. 1981. Heavy ion bombardment of monoclinic $ThSiO_4$, ThO_2 and monazite. *Radiation Effects*, **58**, 1–3, https://doi.org/10.1080/01422448108226520

Kelly, N.M. and Harley, S.L. 2005. An integrated microtextural and chemical approach to zircon geochronology: refining the Archaean history of the Napier Complex, east Antarctica. *Contributions to Mineralogy and Petrology*, **149**, 57–84, https://doi.org/10.1007/s00410-004-0635-6

Kelly, N.M., Harley, S.L. and Möller, A. 2012. Complexity in the behavior and recrystallization of monazite during high-T metamorphism and fluid infiltration. *Chemical Geology*, **322**, 192–208, https://doi.org/10.1016/j.chemgeo.2012.07.001

Kelsey, D.E. and Powell, R. 2011. Progress in linking accessory mineral growth and breakdown to major mineral evolution in metamorphic rocks: A thermodynamic approach in the Na_2O-CaO-K_2O-FeO-MgO-Al_2O_3-SiO_2-H_2O-TiO_2-ZrO_2 system. *Journal of Metamorphic Geology*, **29**, 151–166.

Kelsey, D.E., Hand, M., Clark, C. and Wilson, C.J.L. 2007. On the application of *in situ* monazite chemical geochronology to constraining P–T–t histories in high-temperature (>850°C) polymetamorphic granulites from Prydz Bay, East Antarctica. *Journal of the Geological Society, London*, **164**, 667–683, https://doi.org/10.1144/0016-76492006-013

Kelsey, D.E., Clark, C. and Hand, M. 2008. Thermobarometric modelling of zircon and monazite growth in melt-bearing systems: examples using model metapelitic and metapsammitic granulites. *Journal of Metamorphic Geology*, **26**, 199–212, https://doi.org/10.1111/j.1525-1314.2007.00757.x

Kemp, A., Hawkesworth, C. *et al*. 2007. Magmatic and crustal differentiation history of granitic rocks from Hf–O isotopes in zircon. *Science*, **315**, 980–983, https://doi.org/10.1126/science.1136154

Kennedy, A.K., Wotzlaw, J.-F. *et al*. 2022. Apatite reference materials for SIMS microanalysis of isotopes and trace elements. *Geostandards and Geoanalytical Research*, **47**, 215–467, https://doi.org/10.1111/ggr.12477

King, E.M. and Valley, J.W. 2001. The source, magmatic contamination, and alteration of the Idaho wbatholith. *Contributions to Mineralogy and Petrology*, **142**, 72–88, https://doi.org/10.1007/s004100100278

King, E.M., Valley, J.W., Davis, D.W. and Kowallis, B.J. 2001. Empirical determination of oxygen isotope fractionation factors for titanite with respect to zircon and quartz. *Geochimica et Cosmochimica Acta*, **65**, 3165–3175, https://doi.org/10.1016/S0016-7037(01)00639-1

King, P.L., Sham, T.-K., Gordon, R.A. and Dyar, M.D. 2013. Microbeam X-ray analysis of Ce^{3+}/Ce^{4+} in Ti-rich minerals: a case study with titanite (sphene) with implications for multivalent trace element substitution in minerals. *American Mineralogist*, **98**, 110–119, https://doi.org/10.2138/am.2013.3959

Kingsbury, J.A., Miller, C.F., Wooden, J.L. and Harrison, T.M. 1993. Monazite paragenesis and U–Pb systematics in rocks of the eastern Mojave Desert, California, USA: implications for thermochronometry. *Chemical Geology*, **110**, 147–167, https://doi.org/10.1016/0009-2541(93)90251-D

Kirkland, C.L., Smithies, R.H., Taylor, R.J.M., Evans, N. and McDonald, B. 2015. Zircon Th/U ratios in magmatic environs. *Lithos*, **212**, 397–414, https://doi.org/10.1016/j.lithos.2014.11.021

Kirkland, C.L., Spaggiari, C.V. *et al*. 2016. Grain size matters: Implications for element and isotopic mobility in titanite. *Precambrian Research*, **278**, 283–302, https://doi.org/10.1016/j.precamres.2016.03.002.

Kirkland, C.L., Hollis, J., Danisik, M., Petersen, J., Evans, N. and Mcdonald, B. 2017. Apatite and titanite from the Karrat Group, Greenland; implications for charting the thermal evolution of crust from the U–Pb geochronology of common Pb bearing phases. *Precambrian Research*, **300**, 107–120, https://doi.org/10.1016/j.precamres.2017.07.033

Kirkland, C.L., Fougerouse, D., Reddy, S.M., Hollis, J. and Saxey, D.W. 2018. Assessing the mechanisms of common Pb incorporation into titanite. *Chemical Geology*, **483**, 558–566, https://doi.org/10.1016/j.chemgeo.2018.03.026

Kirkland, C.L., Yakymchuk, C., Gardiner, N.J., Szilas, K., Hollis, J., Olierook, H. and Steenfelt, A. 2020. Titanite petrochronology linked to phase equilibrium modelling constrains tectono-thermal events in the Akia Terrane, West Greenland. *Chemical Geology*, **536**, article, 119467, https://doi.org/10.1016/j.chemgeo.2020.119467

Kirkland, C.L., Hartnady, M.I.H., Barham, M., Olierook, H.K.H., Steenfelt, A. and Hollis, J.A. 2021. Widespread reworking of Hadean-to-Eoarchean continents during Earth's thermal peak. *Nature Communications*, **12**, article 331, https://doi.org/10.1038/s41467-020-20514-4

Klemme, S., Prowatke, S., Hametner, K. and Günther, D. 2005. Partitioning of trace elements between rutile and silicate melts: implications for subduction zones. *Geochimica et Cosmochimica Acta*, **69**, 2361–2371, https://doi.org/10.1016/j.gca.2004.11.015

Kohn, M.J. 2017. Titanite petrochronology. *Reviews in Mineralogy and Geochemistry*, **83**, 419–441, https://doi.org/10.2138/rmg.2017.83.13

Kohn, M.J. 2020. A refined zirconium-in-rutile thermometer. *American Mineralogist: Journal of Earth and Planetary Materials*, **105**, 963–971, https://doi.org/10.2138/am-2020-7091

Kohn, M.J. and Corrie, S.L. 2011. Preserved Zr-temperatures and U–Pb ages in high-grade metamorphic titanite: evidence for a static hot channel in the Himalayan orogen. *Earth and Planetary Science Letters*, **311**, 136–143, https://doi.org/10.1016/j.epsl.2011.09.008

Kohn, M.J. and Valley, J.W. 1998. Effects of cation substitutions in garnet and pyroxene on equilibrium oxygen isotope fractionations. *Journal of Metamorphic Geology*, **16**, 625–639, https://doi.org/10.1111/j.1525-1314.1998.00162.x

Kohn, M.J., Penniston-Dorland, S.C. and Ferreira, J.C.S. 2016. Implications of near-rim compositional zoning in rutile for geothermometry, geospeedometry, and trace element equilibration. *Contributions to Mineralogy and Petrology*, **171**, article 78, https://doi.org/10.1007/s00410-016-1285-1

Kohn, M.J., Engi, M. and Lanari, P. 2017. Petrochronology: methods and applications. *Reviews in Mineralogy and Geochemistry*, **83**, https://doi.org/10.1515/9783110561890

Konečný, P., Kusiak, M.A. and Dunkley, D.J. 2018. Improving U–Th–Pb electron microprobe dating using monazite age references. *Chemical Geology*, **484**, 22– 35, https://doi.org/10.1016/j.chemgeo.2018.02.014

Kooijman, E., Mezger, K. and Berndt, J. 2010. Constraints on the U–Pb systematics of metamorphic rutile from *in situ* LA-ICP-MS analysis. *Earth and Planetary Science Letters*, **293**, 321–330, https://doi.org/10.1016/j.epsl.2010.02.047

Kooijman, E., Smit, M.A., Mezger, K. and Berndt, J. 2012. Trace element systematics in granulite facies rutile: implications for Zr geothermometry and provenance studies. *Journal of Metamorphic Geology*, **30**, 397–412, https://doi.org/10.1111/j.1525-1314.2012.00972.x

Košler, J., Wiedenbeck, M., Wirth, R., Hovorka, J., Sylvester, P. and Míková, J. 2005. Chemical and phase composition of particles produced by laser ablation of silicate glass and zircon–implications for elemental fractionation during ICP-MS analysis. *Journal of Analytical Atomic Spectrometry*, **20**, 402–409, https://doi.org/10.1039/B416269B

Krenn, E. and Finger, F. 2010. Unusually Y-rich monazite-(Ce) with 6–14 wt.% Y_2O_3 in a granulite from the Bohemian Massif: implications for high-temperature monazite growth from the monazite–xenotime miscibility gap thermometry. *Mineralogical Magazine*, **74**, 217–225, https://doi.org/10.1180/minmag.2010.073.2.217

Krenn, E., Schulz, B. and Finger, F. 2012. Three generations of monazite in Austroalpine basement rocks to the south of the Tauern Window: evidence for Variscan, Permian and Eo-Alpine metamorphic events. *Swiss Journal of Geosciences*, **105**, 343–360, https://doi.org/10.1007/s00015-012-0104-6

Krneta, S., Ciobanu, C.L., Cook, N.J. and Ehrig, K.J. 2018. Numerical modeling of REE fractionation patterns in fluorapatite from the Olympic Dam Deposit (South Australia). *Minerals*, **8**, article 342, https://doi.org/10.3390/min8080342

Krogstad, E.J. and Walker, R.J. 1994. High closure temperatures of the U–Pb system in large apatites from the Tin Mountain pegmatite, Black Hills, South Dakota, USA. *Geochimica et Cosmochimica Acta*, **58**, 3845–3853, https://doi.org/10.1016/0016-7037(94)90367-0

Kröner, A., Wan, Y., Liu, X. and Liu, D. 2014. Dating of zircon from high-grade rocks: which is the most reliable method? *Geoscience Frontiers*, **5**, 515–523, https://doi.org/10.1016/j.gsf.2014.03.012

Kulhánek, J., Faryad, S.W., Jedlicka, R. and Svojtka, M. 2021. Dissolution and reprecipitation of garnet during eclogite-facies metamorphism; major and trace element transfer during atoll garnet formation. *Journal of Petrology*, **62**, article egab077, https://doi.org/10.1093/petrology/egab077

Kunz, B.E., Regis, D. and Engi, M. 2018. Zircon ages in granulite facies rocks: decoupling from geochemistry above 850°C? *Contributions to Mineralogy and Petrology*, **173**, article 26, https://doi.org/10.1007/s00410-018-1454-5

Kusiak, M.A., Whitehouse, M.J., Wilde, S.A., Nemchin, A.A. and Clark, C. 2013. Mobilization of radiogenic Pb in zircon revealed by ion imaging: implications for early Earth geochronology. *Geology*, **41**, 291–294, https://doi.org/10.1130/G33920.1

Kylander-Clark, A.R.C., Hacker, B.R. and Mattinson, J.M. 2008. Slow exhumation of UHP terranes: titanite and rutile ages of the Western Gneiss Region, Norway. *Earth and Planetary Science Letters*, **272**, 531–540, https://doi.org/10.1016/j.epsl.2008.05.019

Kylander-Clark, A.R.C., Hacker, B.R. and Cottle, J.M. 2013. Laser-ablation split-stream ICP petrochronology. *Chemical Geology*, **345**, 99–112, https://doi.org/10.1016/J.CHEMGEO.2013.02.019

Lackey, J.S., Valley, J.W. and Hinke, H.J. 2006. Deciphering the source and contamination history of peraluminous magmas using $\delta^{18}O$ of accessory minerals: examples from garnet-bearing plutons of the Sierra Nevada batholith. *Contributions to Mineralogy and Petrology*, **151**, 20–44, https://doi.org/10.1007/s00410-005-0043-6

Lana, C., Gonçalves, G.O. *et al*. 2022. Assessing the U–Pb, Sm–Nd and Sr–Sr isotopic compositions of the Sumé apatite as a reference material for LA-ICP-MS analysis. *Geostandards and Geoanalytical Research*, **46**, 71–95, https://doi.org/10.1111/ggr.12413

Lanari, P. and Engi, M. 2017. Local bulk composition effects on metamorphic mineral assemblages. *Reviews in Mineralogy and Geochemistry*, **83**, 55–102, https://doi.org/10.2138/rmg.2017.83.3

Lanari, P and Piccoli, F 2020. *IOP Conference Series: Materials Science and Engineering*, **891**, 012016, https://doi.org/10.1088/1757-899X/891/1/012016

Lanari, P., Vidal, O., De Andrade, V., Dubacq, B., Lewin, E., Grosch, E.G. and Schwartz, S. 2014. XMapTools: a MATLAB©-based program for electron microprobe X-ray image processing and geothermobarometry. *Computers & Geosciences*, **62**, 227–240, https://doi.org/10.1016/j.cageo.2013.08.010

Lanari, P., Giuntoli, F., Loury, C., Burn, M. and Engi, M. 2017. An inverse modeling approach to obtain P–T conditions of metamorphic stages involving garnet growth and resorption. *European Journal of Mineralogy*, **29**, 181–199, https://doi.org/10.1127/ejm/2017/0029-2597

Lanari, P., Ferrero, S., Goncalves, P. and Grosch, E.G. 2019. Metamorphic geology: progress and perspectives. *Geological Society, London, Special Publications*, **478**, 1–12, https://doi.org/10.1144/SP478-2018-186

Larson, K.P., Ali, A., Shrestha, S., Soret, M., Cottle, J.M. and Ahmad, R. 2019. Timing of metamorphism and deformation in the Swat Valley, northern Pakistan: insight into garnet-monazite HREE partitioning. *Geoscience Frontiers*, **10**, 849–861, https://doi.org/10.1016/j.gsf.2018.02.008

Larson, K.P., Shrestha, S., Cottle, J.M., Guilmette, C., Johnson, T.A., Gibson, H.D. and Gervais, F. 2022. Re-evaluating monazite as a record of metamorphic reactions. *Geoscience Frontiers*, **13**, article 101340, https://doi.org/10.1016/j.gsf.2021.101340

Larsson, D. and Söderlund, U. 2005. Lu–Hf apatite geochronology of mafic cumulates: an example from a Fe–Ti mineralization at Smålands Taberg, southern Sweden. *Chemical Geology*, **224**, 201–211, https://doi.org/10.1016/j.chemgeo.2005.07.007

Laurent, A.T., Duchene, S., Bingen, B., Bosse, V. and Seydoux-Guillaume, A.-M. 2018. Two successive phases of ultrahigh temperature metamorphism in Rogaland, S. Norway: evidence from Y-in-monazite thermometry. *Journal of Metamorphic Geology*, **36**, 1009–1037, https://doi.org/10.1111/jmg.12425

Laurent, O., Zeh, A., Gerdes, A., Villaros, A., Gros, K. and Słaby, E. 2017. How do granitoid magmas mix with each other? Insights from textures, trace element and Sr–Nd isotopic composition of apatite and titanite from the Matok pluton (South Africa). *Contributions to Mineralogy and Petrology*, **172**, article 80, https://doi.org/10.1007/s00410-017-1398-1

Laurent, O., Moyen, J.-F., Wotzlaw, J.-F., Björnsen, J. and Bachmann, O. 2021. Early Earth zircons formed in residual granitic melts produced by tonalite differentiation. *Geology*, **50**, 437–441, https://doi.org/10.1130/G49232.1

Lawley, C.J.M., Creaser, R.A. *et al*. 2015. Unraveling the western Churchill Province Paleoproterozoic gold metallotect: constraints from Re–Os arsenopyrite and U–Pb xenotime geochronology and LA-ICP-MS arsenopyrite trace element chemistry at the BIF-hosted Meliadine gold district, Nunavut, Canada. *Economic Geology*, **110**, 1425–1454, https://doi.org/10.2113/econgeo.110.6.1425

Lee, J.K.W., Williams, I.S. and Ellis, D.J. 1997. Pb, U and Th diffusion in natural zircon. *Nature*, **390**, 159–162, https://doi.org/10.1038/36554

Lei, H., Xu, H. and Liu, P. 2020. Decoupling between Ti-in-zircon and Zr-in-rutile thermometry during ultrahigh temperature metamorphism of the Dabie Orogen, China. *Geological Journal*, **55**, 6442–6449, https://doi.org/10.1002/gj.3819

Le Roux, L. and Glendenin, L. 1963. Half-life of ^{232}Th. In: *Proceedings of the National Meeting on Nuclear Energy*, Pretoria, South Africa. **83**, 94.

Li, B., Ge, J. and Zhang, B. 2018. Diffusion in garnet: a review. *Acta Geochimica*, **37**, 19–31, https://doi.org/10.1007/s11631-017-0187-x

Li, D., Fu, Y. *et al*. 2022. PL57 garnet as a new natural reference material for *in situ* U–Pb isotope analysis and its perspective for geological applications. *Contributions to Mineralogy and Petrology*, **177**, article 19, https://doi.org/10.1007/s00410-021-01884-4

Li, R., Collins, W.J., Yang, J.-H., Blereau, E. and Wang, H. 2021. Two-stage hybrid origin of Lachlan S-type magmas: a re-appraisal using isotopic microanalysis of lithic inclusion minerals. *Lithos*, **402–403**, article 106378, https://doi.org/10.1016/j.lithos.2021.106378

Li, W.-T., Jiang, S.-Y., Fu, B., Liu, D.-L. and Xiong, S.-F. 2021. Zircon Hf–O isotope and magma oxidation state evidence for the origin of Early Cretaceous granitoids and porphyry Mo mineralization in the Tongbai–Hong'an–Dabie orogens, eastern China. *Lithos*, **398**, article 106281, https://doi.org/10.1016/j.lithos.2021.106281

Liao, X., Li, Q., Whitehouse, M.J., Yang, Y. and Liu, Y. 2020. Allanite U–Th–Pb geochronology by ion microprobe. *Journal of Analytical Atomic Spectrometry*, **35**, 489–497, https://doi.org/10.1039/C9JA00426B

Liebmann, J., Spencer, C.J., Kirkland, C.L., Xia, X.-P. and Bourdet, J. 2021. Effect of water on δ^{18}O in zircon. *Chemical Geology*, **574**, article 120243, https://doi.org/10.1016/j.chemgeo.2021.120243

Lin, S., Hu, K., Cao, J., Liu, Y., Liu, S. and Zhang, B. 2023. Geochemistry and origin of hydrothermal apatite in Carlin-type Au deposits, southwestern China (Gaolong deposit). *Ore Geology Reviews*, **154**, article 105312, https://doi.org/10.1016/j.oregeorev.2023.105312

Liu, Z.-C., Wu, F.-Y., Ji, W.-Q., Wang, J.-G. and Liu, C.-Z. 2014. Petrogenesis of the Ramba leucogranite in the Tethyan Himalaya and constraints on the channel flow model. *Lithos*, **208–209**, 118–136, https://doi.org/10.1016/j.lithos.2014.08.022

Loader, M.A., Nathwani, C.L., Wilkinson, J.J. and Armstrong, R.N. 2022. Controls on the magnitude of Ce anomalies in zircon. *Geochimica et Cosmochimica Acta*, **328**, 242–257, https://doi.org/10.1016/j.gca.2022.03.024

López-Moro, F.J., Romer, R., López-Plaza, M. and Sanchez, M.G. 2017. Zircon and allanite U–Pb ID-TIMS ages of vaugnerites from the Calzadilla pluton, Salamanca (Spain): dating mantle-derived magmatism and post-magmatic subsolidus overprint. *Geologica Acta*, **15**, 395–408, https://doi.org/10.1344/GeologicaActa2017.15.4.9

Lü, Z., Zhang, L., Du, J. and Bucher, K. 2008. Coesite inclusions in garnet from eclogitic rocks in western Tianshan, northwest China: convincing proof of UHP metamorphism. *American Mineralogist*, **93**, 1845–1850, https://doi.org/10.2138/am.2008.2800

Lucassen, F., Franz, G., Dulski, P., Romer, R.L. and Rhede, D. 2011. Element and Sr isotope signatures of titanite as indicator of variable fluid composition in hydrated eclogite. *Lithos*, **121**, 12–24, https://doi.org/10.1016/j.lithos.2010.09.018

Lucassen, F., Franz, G. and Rhede, D. 2012. Small-scale transport of trace elements Nb and Cr during growth of titanite: an experimental study at 600°C, 0.4 GPa. *Contributions to Mineralogy and Petrology*, **164**, 987–997, https://doi.org/10.1007/s00410-012-0784-y

Luvizotto, G.L. and Zack, T. 2009. Nb and Zr behavior in rutile during high-grade metamorphism and retrogression: an example from the Ivrea–Verbano Zone. *Chemical Geology*, **261**, 303–317, https://doi.org/10.1016/j.chemgeo.2008.07.023

Luvizotto, G.L., Zack, T. *et al*. 2009. Rutile crystals as potential trace element and isotope mineral standards for microanalysis. *Chemical Geology*, **261**, 346–369, https://doi.org/10.1016/j.chemgeo.2008.04.012

Ma, Q., Evans, N.J., Ling, X.-X., Yang, J.-H., Wu, F.-Y., Zhao, Z.-D. and Yang, Y.-H. 2019. Natural titanite reference materials for *in situ* U–Pb and Sm–Nd isotopic measurements by LA-(MC)-ICP-MS. *Geostandards and Geoanalytical Research*, **43**, 355–384, https://doi.org/10.1111/ggr.12264

Machado, N. and Gauthier, G. 1996. Determination of ^{207}Pb/^{206}Pb ages on zircon and monazite by laser-ablation ICPMS and application to a study of sedimentary provenance and metamorphism in southeastern Brazil. *Geochimica et Cosmochimica Acta*, **60**, 5063–5073, https://doi.org/10.1016/S0016-7037(96)00287-6

Mahan, K.H., Goncalves, P., Williams, M.L. and Jercinovic, M.J. 2006. Dating metamorphic reactions and fluid flow: application to exhumation of high-P granulites in a

crustal-scale shear zone, western Canadian Shield. *Journal of Metamorphic Geology*, **24**, 193–217, https://doi.org/10.1111/j.1525-1314.2006.00633.x

Maneiro, K.A., Baxter, E.F., Samson, S.D., Marschall, H.R. and Hietpas, J. 2019. Detrital garnet geochronology: application in tributaries of the French Broad River, southern Appalachian Mountains, USA. *Geology*, **47**, 1189–1192, https://doi.org/10.1130/G46840.1

Manzotti, P., Bosse, V., Pitra, P., Robyr, M., Schiavi, F. and Ballèvre, M. 2018. Exhumation rates in the Gran Paradiso Massif (Western Alps) constrained by *in situ* U–Th–Pb dating of accessory phases (monazite, allanite and xenotime). *Contributions to Mineralogy and Petrology*, **173**, article 24, https://doi.org/10.1007/s00410-018-1452-7

Manzotti, P., Schiavi, F., Nosenzo, F., Pitra, P. and Ballèvre, M. 2022. A journey towards the forbidden zone: a new, cold, UHP unit in the Dora-Maira Massif (Western Alps). *Contributions to Mineralogy and Petrology*, **177**, 1–22, https://doi.org/10.1007/s00410-022-01923-8

Marfin, A.E., Ivanov, A.V., Kamenetsky, V.S., Abersteiner, A., Yakich, T.Y. and Dudkin, T.V. 2020. Contact metamorphic and metasomatic processes at the Kharaelakh intrusion, Oktyabrsk deposit, Norilsk–Talnakh ore district: application of LA-ICP-MS dating of perovskite, apatite, garnet, and titanite. *Economic Geology*, **115**, 1213–1226, https://doi.org/10.5382/econgeo.4744

Mark, C., Stutenbecker, L. *et al*. 2022. Detrital garnet Lu–Hf and U–Pb geochronometry coupled with compositional analysis: possibilities and limitations as a sediment provenance indicator. *EGU General Assembly, Conference Abstracts*, 23–27 May 2022, Vienna, Austria, EGU22-6405, https://doi.org/10.5194/egusphere-egu22-6405.

Mark, G. 2001. Nd isotope and petrogenetic constraints for the origin of the Mount Angelay igneous complex: implications for the origin of intrusions in the Cloncurry district, NE Australia. *Precambrian Research*, **105**, 17–35, https://doi.org/10.1016/S0301-9268(00)00101-7

Marmo, B., Clarke, G. and Powell, R. 2002. Fractionation of bulk rock composition due to porphyroblast growth: effects on eclogite facies mineral equilibria, Pam Peninsula, New Caledonia. *Journal of Metamorphic Geology*, **20**, 151–165, https://doi.org/10.1046/j.0263-4929.2001.00346.x

Marsh, J.H. and Smye, A.J. 2017. U–Pb systematics and trace element characteristics in titanite from a high-pressure mafic granulite. *Chemical Geology*, **466**, 403–416, https://doi.org/10.1016/j.chemgeo.2017.06.029

Martin, A.J., Gehrels, G.E. and DeCelles, P.G. 2007. The tectonic significance of (U, Th)/Pb ages of monazite inclusions in garnet from the Himalaya of central Nepal. *Chemical Geology*, **244**, 1–24, https://doi.org/10.1016/j.chemgeo.2007.05.003

Martin, E.L., Collins, W.J. and Spencer, C.J. 2020. Laurentian origin of the Cuyania suspect terrane, western Argentina, confirmed by Hf isotopes in zircon. *GSA Bulletin*, **132**, 273–290, https://doi.org/10.1130/B35150.1

Martin, L.A.J., Ballèvre, M., Boulvais, P., Halfpenny, A., Vanderhaeghe, O., Duchêne, S. and Deloule, E. 2011. Garnet re-equilibration by coupled dissolution–reprecipitation: evidence from textural, major element and oxygen isotope zoning of 'cloudy' garnet. *Journal of Metamorphic Geology*, **29**, 213–231, https://doi.org/10.1111/j.1525-1314.2010.00912.x

Martin, L.A.J., Rubatto, D., Crépisson, C., Hermann, J., Putlitz, B. and Vitale-Brovarone, A. 2014. Garnet oxygen analysis by SHRIMP-SI: matrix corrections and application to high-pressure metasomatic rocks from Alpine Corsica. *Chemical Geology*, **374**, 25–36, https://doi.org/10.1016/j.chemgeo.2014.02.010

Massonne, H.-J. and Li, B. 2022. Eclogite with unusual atoll garnet from the southern Armorican Massif, France: pressure–temperature path and geodynamic implications. *Tectonophysics*, **823**, article 229183, https://doi.org/10.1016/j.tecto.2021.229183

Mazzucchelli, M.L., Angel, R.J. and Alvaro, M. 2021. EntraPT: an online platform for elastic geothermobarometry. *American Mineralogist*, **106**, 830–837, https://doi.org/10.2138/am-2021-7693CCBYNCND

McCubbin, F.M. and Jones, R.H. 2015. Extraterrestrial apatite: planetary geochemistry to astrobiology. *Elements*, **11**, 183–188, https://doi.org/10.2113/gselements.11.3.183

McCubbin, F.M., Boyce, J.W. *et al*. 2016. Geologic history of Martian regolith breccia Northwest Africa 7034: evidence for hydrothermal activity and lithologic diversity in the Martian crust. *Journal of Geophysical Research: Planets*, **121**, 2120–2149, https://doi.org/10.1002/2016JE005143

McFarlane, C.R. 2016. Allanite U–Pb geochronology by 193 nm LA ICP-MS using NIST610 glass for external calibration. *Chemical Geology*, **438**, 91–102, https://doi.org/10.1016/j.chemgeo.2016.05.026

McGregor, M., Erickson, T.M. *et al*. 2021. High-resolution EBSD and SIMS U–Pb geochronology of zircon, titanite, and apatite: insights from the Lac La Moinerie impact structure, Canada. *Contributions to Mineralogy and Petrology*, **176**, article 76, https://doi.org/10.1007/s00410-021-01828-y

Mearns, E.W. 1986. Sm–Nd ages for Norwegian garnet peridotite. *Lithos*, **19**, 269–278, https://doi.org/10.1016/0024-4937(86)90027-7

Méheut, M., Ibañez-Mejia, M. and Tissot, F.L. 2021. Drivers of zirconium isotope fractionation in Zr-bearing phases and melts: the roles of vibrational, nuclear field shift and diffusive effects. *Geochimica et Cosmochimica Acta*, **292**, 217–234, https://doi.org/10.1016/j.gca.2020.09.028

Meinhold, G., Anders, B., Kostopoulos, D. and Reischmann, T. 2008. Rutile chemistry and thermometry as provenance indicator: an example from Chios Island, Greece. *Sedimentary Geology*, **203**, 98–111, https://doi.org/10.1016/j.sedgeo.2007.11.004

Meyer, M., John, T., Brandt, S. and Klemd, R. 2011. Trace element composition of rutile and the application of Zr-in-rutile thermometry to UHT metamorphism (Epupa Complex, NW Namibia). *Lithos*, **126**, 388–401, https://doi.org/10.1016/j.lithos.2011.07.013

Mezger, K., Hanson, G.N. and Bohlen, S.R. 1989*a*. High-precision U–Pb ages of metamorphic rutile: application to the cooling history of high-grade terranes. *Earth and Planetary Science Letters*, **96**, 106–118, https://doi.org/10.1016/0012-821X(89)90126-X

Mezger, K., Hanson, G.N. and Bohlen, S.R. 1989*b*. U–Pb systematics of garnet: dating the growth of garnet in the Late Archean Pikwitonei granulite domain at Cauchon and Natawahunan lakes, Manitoba, Canada. *Contributions to Mineralogy and Petrology*, **101**, 136–148, https://doi.org/10.1007/BF00375301

Mezger, K., Rawnsley, C.M., Bohlen, S.R. and Hanson, G.N. 1991. U–Pb garnet, sphene, monazite, and rutile ages: implications for the duration of high-grade metamorphism and cooling histories, Adirondack Mts, New York. *The Journal of Geology*, **99**, 415–428, https://doi.org/10.1086/629503

Millonig, L.J., Albert, R., Gerdes, A., Avigad, D. and Dietsch, C. 2020. Exploring laser ablation U–Pb dating of regional metamorphic garnet – The Straits Schist, Connecticut, USA. *Earth and Planetary Science Letters*, **552**, article 116589, https://doi.org/10.1016/j.epsl.2020.116589

Millonig, L.J., Beranoaguirre, A., Albert, R., Marschall, H., Baxter, E. and Gerdes, A. 2022. Garnet U–Pb dating by LA-ICPMS: opportunities, limitations, and applications. *EGU General Assembly Abstracts*, Vienna, Austria, EUG22-7077, https://doi.org/10.5194/egusphere-egu22-7077

Mills, S.J., Hatert, F., Nickel, E.H. and Ferraris, G. 2009. The standardisation of mineral group hierarchies: application to recent nomenclature proposals. *European Journal of Mineralogy*, **21**, 1073–1080, https://doi.org/10.1127/0935-1221/2009/0021-1994

Möller, A., O'Brien, P.J., Kennedy, A. and Kröner, A. 2003. Linking growth episodes of zircon and metamorphic textures to zircon chemistry: an example from the ultrahigh-temperature granulites of Rogaland (SW Norway). *Geological Society, London, Special Publications*, **220**, 65–81, https://doi.org/10.1144/GSL.SP.2003.220.01.04

Montel, J.-M. 1993. A model for monazite/melt equilibrium and application to the generation of granitic magmas. *Chemical Geology*, **110**, 127–146, https://doi.org/10.1016/0009-2541(93)90250-M

Montel, J.-M., Foret, S., Veschambre, M., Nicollet, C. and Provost, A. 1996. Electron microprobe dating of monazite. *Chemical Geology*, **131**, 37–53, https://doi.org/10.1016/0009-2541(96)00024-1

Montel, J.-M., Kato, T., Enami, M., Cocherie, A., Finger, F., Williams, M. and Jercinovic, M. 2018. Electron-microprobe dating of monazite: the story. *Chemical Geology*, **484**, 4–15, https://doi.org/10.1016/j.chemgeo.2017.11.001

Moore, J., Beinlich, A., Piazolo, S., Austrheim, H. and Putnis, A. 2020*a*. Metamorphic differentiation via enhanced dissolution along high permeability zones. *Journal of Petrology*, **61**, article egaa096, https://doi.org/10.1093/petrology/egaa096

Moore, J., Beinlich, A. *et al*. 2020*b*. Microstructurally controlled trace element (Zr, U–Pb) concentrations in metamorphic rutile: an example from the amphibolites of the Bergen Arcs. *Journal of Metamorphic Geology*, **38**, 103–127, https://doi.org/10.1111/jmg.12514

Morrissey, L.J., Hand, M., Lane, K., Kelsey, D.E. and Dutch, R.A. 2016. Upgrading iron–ore deposits by melt loss during granulite facies metamorphism. *Ore Geology Reviews*, **74**, 101–121, https://doi.org/10.1016/j.oregeorev.2015.11.012

Moser, A.C., Hacker, B.R., Gehrels, G.E., Seward, G.G.E., Kylander-Clark, A.R.C. and Garber, J.M. 2022. Linking titanite U–Pb dates to coupled deformation and dissolution–reprecipitation. *Contributions to Mineralogy and Petrology*, **177**, article 42, https://doi.org/10.1007/s00410-022-01906-9

Mottram, C.M., Warren, C.J., Regis, D., Roberts, N.M.W., Harris, N.B.W., Argles, T.W. and Parrish, R.R. 2014. Developing an inverted Barrovian sequence; insights from monazite petrochronology. *Earth and Planetary Science Letters*, **403**, 418–431, https://doi.org/10.1016/j.epsl.2014.07.006

Mottram, C.M., Parrish, R.R., Regis, D., Warren, C.J., Argles, T.W., Harris, N.B.W. and Roberts, N.M.W. 2015. Using U–Th–Pb petrochronology to determine rates of ductile thrusting: time windows into the Main Central Thrust, Sikkim Himalaya. *Tectonics*, **34**, 1355–1374, https://doi.org/10.1002/2014TC003743

Mottram, C.M., Cottle, J.M. and Kylander-Clark, A.R.C. 2019. Campaign-style U–Pb titanite petrochronology: along-strike variations in timing of metamorphism in the Himalayan metamorphic core. *Geoscience Frontiers*, **10**, 827–847, https://doi.org/10.1016/j.gsf.2018.09.007

Moyen, J.F. and Martin, H. 2012. Forty years of TTG research. *Lithos*, **148**, 312–336.

Moyen, J.F. and Stevens, G. 2006. Experimental constraints on TTG petrogenesis: implications for Archean geodynamics. *AGU Geophysical Monograph Series*, **164**, 149–175, http://doi.org/10.1029/164GM11

Mühlberg, M., Stevens, G., Moyen, J.-F., Kisters, A.F. and Lana, C. 2021. Thermal evolution of the Stolzburg Block, Barberton granitoid–greenstone terrain, South Africa: implications for Paleoarchean tectonic processes. *Precambrian Research*, **359**, article 106082, https://doi.org/10.1016/j.precamres.2020.106082

Mulder, J.A. and Cawood, P.A. 2021. Evaluating preservation bias in the continental growth record against the monazite archive. *Geology*, **50**, 243–247, https://doi.org/10.1130/G49416.1

Mulder, J.A., Nebel, O., Gardiner, N.J., Cawood, P.A., Wainwright, A.N. and Ivanic, T.J. 2021. Crustal rejuvenation stabilised Earth's first cratons. *Nature Communications*, **12**, 1–7, https://doi.org/10.1038/s41467-021-23805-6

Muñoz-Montecinos, J., Angiboust, S., Garcia-Casco, A. and Raimondo, T. 2023. Shattered veins elucidate brittle creep processes in the deep slow slip and tremor region. *Tectonics*, **42**, e2022TC007605, https://doi.org/10.1029/2022TC007605

Næraa, T., Scherstén, A., Rosing, M.T., Kemp, A., Hoffmann, J., Kokfelt, T. and Whitehouse, M. 2012. Hafnium isotope evidence for a transition in the dynamics of continental growth 3.2 Gyr ago. *Nature*, **485**, 627–630, https://doi.org/10.1038/nature11140

Nasdala, L., Zhang, M., Kempe, U., Panczer, G., Gaft, M., Andrut, M. and Plötze, M. 2003. Spectroscopic methods applied to zircon. *Reviews in Mineralogy and Geochemistry*, **53**, 427–467, https://doi.org/10.2113/0530427

Nestola, F. 2021. How to apply elastic geobarometry in geology. *American Mineralogist*, **106**, 669–671, https://doi.org/10.2138/am-2021-7845

Newton, R. and Haselton, H. 1981. Thermodynamics of the garnet–plagioclase–Al_2SiO_5–quartz geobarometer. *In*: Newton, R.C., Navrotsky, A. and Wood, B.J. (eds) *Thermodynamics of Minerals and Melts*. Springer, 131–147.

Ning, W., Wang, J., Xiao, D., Li, F., Huang, B. and Fu, D. 2019. Electron probe microanalysis of monazite and its applications to U–Th–Pb dating of geological samples. *Journal of Earth Science*, **30**, 952–963, https://doi.org/10.1007/s12583-019-1020-8

Nishizawa, M., Takahata, N., Terada, K., Komiya, T., Ueno, Y. and Sano, Y. 2005. Rare-earth element, lead, carbon, and nitrogen geochemistry of apatite-bearing metasediments from the ~3.8 Ga Isua Supracrustal Belt, West Greenland. *International Geology Review*, **47**, 952–970, https://doi.org/10.2747/0020-6814.47.9.952

Nordsvan, A.R., Collins, W.J. *et al*. 2018. Laurentian crust in northeast Australia: implications for the assembly of the supercontinent Nuna. *Geology*, **46**, 251–254, https://doi.org/10.1130/G39980.1

Nutman, A.P. 2007. Apatite recrystallisation during prograde metamorphism, Cooma, southeast Australia: implications for using an apatite–graphite association as a biotracer in ancient metasedimentary rocks. *Australian Journal of Earth Sciences*, **54**, 1023–1032, https://doi.org/10.1080/08120090701488321

Oberli, F., Meier, M., Berger, A., Rosenberg, C.L. and Gieré, R. 2004. U–Th–Pb and $^{230}Th/^{238}U$ disequilibrium isotope systematics: precise accessory mineral chronology and melt evolution tracing in the Alpine Bergell intrusion. *Geochimica et Cosmochimica Acta*, **68**, 2543–2560, https://doi.org/10.1016/j.gca.2003.10.017

Odlum, M.L., Levy, D.A., Stockli, D.F., Stockli, L.D. and DesOrmeau, J.W. 2022. Deformation and metasomatism recorded by single-grain apatite petrochronology. *Geology*, **50**, 697–703, https://doi.org/10.1130/G49809.1

Olierook, H.K.H., Taylor, R.J.M. *et al*. 2019. Unravelling complex geologic histories using U–Pb and trace element systematics of titanite. *Chemical Geology*, **504**, 105–122, https://doi.org/10.1016/j.chemgeo.2018.11.004

Olierook, H.K.H., Rankenburg, K. *et al*. 2020. Resolving multiple geological events using *in situ* Rb–Sr geochronology: implications for metallogenesis at Tropicana, Western Australia. *Geochronology*, **2**, 283–303, https://doi.org/10.5194/gchron-2-283-2020

Olin, P.H. and Wolff, J.A. 2012. Partitioning of rare earth and high field strength elements between titanite and phonolitic liquid. *Lithos*, **128–131**, 46–54, https://doi.org/10.1016/j.lithos.2011.10.007

O'Reilly, S.Y. and Griffin, W. 2000. Apatite in the mantle: implications for metasomatic processes and high heat production in Phanerozoic mantle. *Lithos*, **53**, 217– 232, https://doi.org/10.1016/S0024-4937(00)00026-8

Ortolano, G., Visalli, R., Cirrincione, R. and Rebay, G. 2014. PT-path reconstruction via unraveling of peculiar zoning pattern in atoll shaped garnets via image assisted analysis: an example from the Santa Lucia del Mela garnet micaschists (northeastern Sicily-Italy). *Periodico di Mineralogia*, **83**, 257–297.

Ortolano, G., Visalli, R., Godard, G. and Cirrincione, R. 2018. Quantitative X-ray map analyser (Q-XRMA): a new GIS-based statistical approach to mineral image analysis. *Computers & Geosciences*, **115**, 56–65, https://doi.org/10.1016/j.cageo.2018.03.001

O'Sullivan, G.J. and Chew, D.M. 2020. The clastic record of a Wilson Cycle: evidence from detrital apatite petrochronology of the Grampian–Taconic fore-arc. *Earth and Planetary Science Letters*, **552**, article 116588, https://doi.org/10.1016/j.epsl.2020.116588

O'Sullivan, G.J., Chew, D., Morton, A., Mark, C. and Henrichs, I. 2018. An integrated apatite geochronology and geochemistry tool for sedimentary provenance analysis. *Geochemistry, Geophysics, Geosystems*, **19**, 1309–1326, https://doi.org/10.1002/2017GC007343

O'Sullivan, G., Chew, D., Kenny, G., Henrichs, I. and Mulligan, D. 2020. The trace element composition of apatite and its application to detrital provenance studies. *Earth-Science Reviews*, **201**, article 103044, https://doi.org/10.1016/j.earscirev.2019.103044

O'Sullivan, G., Hoare, B., Mark, C., Drakou, F. and Tomlinson, E. 2023. Uranium–lead geochronology applied to pyrope garnet with very low concentrations of uranium. *Geological Magazine*, **160**, 1010–1019, https://doi.org/10.1017/S0016756823000122

Page, F.Z., Kita, N.T. and Valley, J.W. 2010. Ion microprobe analysis of oxygen isotopes in garnets of complex chemistry. *Chemical Geology*, **270**, 9–19, https://doi.org/10.1016/j.chemgeo.2009.11.001

Papapavlou, K., Darling, J.R., Storey, C.D., Lightfoot, P.C., Moser, D.E. and Lasalle, S. 2017. Dating shear zones with plastically deformed titanite: new insights into the orogenic evolution of the Sudbury impact structure (Ontario, Canada). *Precambrian Research*, **291**, 220–235, https://doi.org/10.1016/j.precamres.2017.01.007

Pape, J., Mezger, K. and Robyr, M. 2016. A systematic evaluation of the Zr-in-rutile thermometer in ultra-high temperature (UHT) rocks. *Contributions to Mineralogy and Petrology*, **171**, article 44, https://doi.org/10.1007/s00410-016-1254-8

Parrish, R.R. 1990. U–Pb dating of monazite and its application to geological problems. *Canadian Journal of Earth Sciences*, **27**, 1431–1450, https://doi.org/10.1139/e90-152

Passchier, C.W. and Simpson, C. 1986. Porphyroclast systems as kinematic indicators. *Journal of Structural Geology*, **8**, 831–843, https://doi.org/10.1016/0191-8141(86)90029-5

Patchett, P.J. 1983. Importance of the Lu–Hf isotopic system in studies of planetary chronology and chemical evolution. *Geochimica et Cosmochimica Acta*, **47**, 81–91, https://doi.org/10.1016/0016-7037(83)90092-3

Paul, A.N., Spikings, R.A., Chew, D. and Daly, J.S. 2019. The effect of intra-crystal uranium zonation on apatite U–Pb thermochronology: a combined ID-TIMS and LA-MC-ICP-MS study. *Geochimica et Cosmochimica Acta*, **251**, 15–35, https://doi.org/10.1016/j.gca.2019.02.013

Paul, A.N., Spikings, R.A. and Gaynor, S.P. 2021. U–Pb ID-TIMS reference ages and initial Pb isotope compositions for Durango and Wilberforce apatites. *Chemical Geology*, **586**, article 120604, https://doi.org/10.1016/j.chemgeo.2021.120604

Peixoto, E., Alkmim, F.F., Pedrosa-Soares, A., Lana, C. and Chaves, A.O. 2018. Metamorphic record of collision and collapse in the Ediacaran–Cambrian Araçuaí orogen, SE-Brazil: insights from P–T pseudosections and monazite dating. *Journal of Metamorphic Geology*, **36**, 147–172, https://doi.org/10.1111/JMG.12287

Penniston-Dorland, S.C., Kohn, M.J. and Piccoli, P.M. 2018. A mélange of subduction temperatures: evidence from Zr-in-rutile thermometry for strengthening of the subduction interface. *Earth and Planetary Science Letters*, **482**, 525–535, https://doi.org/10.1016/j.epsl.2017.11.005

Penniston-Dorland, S.C., Baumgartner, L.P., Dragovic, B. and Bouvier, A.-S. 2020. Li isotope zoning in garnet from Franciscan eclogite and amphibolite: the role of subduction-related fluids. *Geochimica et Cosmochimica Acta*, **286**, 198–213, https://doi.org/10.1016/j.gca.2020.07.025

Pe-Piper, G., Piper, D.J. and Triantafyllidis, S. 2014. Detrital monazite geochronology, Upper Jurassic–Lower Cretaceous of the Scotian Basin: significance for tracking first-cycle sources. *Geological Society, London, Special Publications*, **386**, 293–311, https://doi.org/10.1144/SP386.13

Perchuk, L. and Lavrent'Eva, I. 1983. Experimental investigation of exchange equilibria in the system cordierite–garnet–biotite. *Advances in Physical Geochemistry*, **3**, 199–239.

Pereira, I. and Storey, C.D. 2023. Detrital rutile: records of the deep crust, ores and fluids. *Lithos*, 438–439, article 107010, https://doi.org/10.1016/j.lithos.2022.107010

Pereira, I., Storey, C., Darling, J., Lana, C. and Alkmim, A.R. 2019. Two billion years of evolution enclosed in hydrothermal rutile: recycling of the São Francisco Craton crust and constraints on gold remobilisation processes. *Gondwana Research*, **68**, 69–92, https://doi.org/10.1016/j.gr.2018.11.008

Pereira, I. *et al*. In press. A review of detrital heavy mineral contributions to furthering our understanding of continental crust formation and evolution. *Geological Society, London, Special Publications*, https://doi.org/SP537-2022-250

Petrus, J.A., Chew, D.M., Leybourne, M.I. and Kamber, B.S. 2017. A new approach to laser-ablation inductively-coupled-plasma mass-spectrometry (LA-ICP-MS) using the flexible map interrogation tool 'Monocle'. *Chemical Geology*, **463**, 76–93, https://doi.org/10.1016/j.chemgeo.2017.04.027

Peverelli, V., Berger, A., Mulch, A., Pettke, T., Piccoli, F. and Herwegh, M. 2022. Epidote U–Pb geochronology and H isotope geochemistry trace pre-orogenic hydration of midcrustal granitoids. *Geology*, **50**, 1073–1077, https://doi.org/10.1130/G50028.1

Piccoli, P.M. and Candela, P.A. 2002. Apatite in igneous systems. *Reviews in Mineralogy and Geochemistry*, **48**, 255–292, https://doi.org/10.2138/rmg.2002.48.6

Piccoli, P., Candela, P. and Rivers, M. 2000. Interpreting magmatic processes from accessory phases: titanite – a small-scale recorder of large-scale processes. *Earth and Environmental Science Transactions of the Royal Society of Edinburgh*, **91**, 257–267, https://doi.org/10.1017/S0263593300007422

Pidgeon, R.T., Chapman, P.G., Danišík, M. and Nemchin, A.A. 2017. Dry annealing of metamict zircon: a differential scanning calorimetry study. *American Mineralogist*, **102**, 1066–1072, https://doi.org/10.2138/am-2017-5901

Pidgeon, R.T., Nemchin, A., Roberts, M., Whitehouse, M.J. and Bellucci, J. 2019. The accumulation of non-formula elements in zircons during weathering: ancient zircons from the Jack Hills, Western Australia. *Chemical Geology*, **530**, article 119310, https://doi.org/10.1016/j.chemgeo.2019.119310

Piechocka, A.M., Gregory, C.J., Zi, J.-W., Sheppard, S., Wingate, M.T.D. and Rasmussen, B. 2017. Monazite trumps zircon: applying SHRIMP U–Pb geochronology to systematically evaluate emplacement ages of leucocratic, low-temperature granites in a complex Precambrian orogen. *Contributions to Mineralogy and Petrology*, **172**, article 63, https://doi.org/10.1007/s00410-017-1386-5

Plank, T., Cooper, L.B. and Manning, C.E. 2009. Emerging geothermometers for estimating slab surface temperatures. *Nature Geoscience*, **2**, 611–615, https://doi.org/10.1038/ngeo614

Plavsa, D., Reddy, S., Clark, C. and Agangi, A. 2018. *Capricorn Orogen Rutile Study: a Combined Electrons Backscatter Diffraction (EBSD) and Laser Ablation Split Stream (LASS) Analytical Approach*. Government of Western Australia.

Pochon, A., Beaudoin, G., Branquet, Y., Boulvais, P., Gloaguen, E. and Gapais, D. 2017. Metal mobility during hydrothermal breakdown of Fe–Ti oxides: insights from Sb–Au mineralizing event (Variscan Armorican Massif, France). *Ore Geology Reviews*, **91**, 66–99, https://doi.org/10.1016/j.oregeorev.2017.10.021

Poitrasson, F., Chenery, S. and Shepherd, T.J. 2000. Electron microprobe and LA-ICP-MS study of monazite hydrothermal alteration: implications for U–Th–Pb geochronology and nuclear ceramics. *Geochimica et Cosmochimica Acta*, **64**, 3283–3297, https://doi.org/10.1016/S0016-7037(00)00433-6

Pollington, A.D. and Baxter, E.F. 2010. High resolution Sm–Nd garnet geochronology reveals the uneven pace of tectonometamorphic processes. *Earth and Planetary Science Letters*, **293**, 63–71, https://doi.org/10.1016/j.epsl.2010.02.019

Pollington, A.D. and Baxter, E.F. 2011. High precision microsampling and preparation of zoned garnet porphyroblasts for Sm–Nd geochronology. *Chemical Geology*, **281**, 270–282, https://doi.org/10.1016/j.chemgeo.2010.12.014

Porter, J.K., McNaughton, N.J., Evans, N.J. and McDonald, B.J. 2020. Rutile as a pathfinder for metals exploration. *Ore Geology Reviews*, **120**, article 103406, https://doi.org/10.1016/j.oregeorev.2020.103406

Potts, N.J., Barnes, J.J., Tartèse, R., Franchi, I.A. and Anand, M. 2018. Chlorine isotopic compositions of apatite in Apollo 14 rocks: evidence for widespread vapor-phase metasomatism on the lunar nearside *c.* 4 billion years ago. *Geochimica et Cosmochimica Acta*, **230**, 46–59, https://doi.org/10.1016/j.gca.2018.03.022

Pourteau, A., Scherer, E.E., Schorn, S., Bast, R., Schmidt, A. and Ebert, L. 2019. Thermal evolution of an ancient subduction interface revealed by Lu–Hf garnet

geochronology, Halilbağı Complex (Anatolia). *Geoscience Frontiers*, **10**, 127–148, https://doi.org/10.1016/j.gsf.2018.03.004

Prent, A.M., Beinlich, A., Morrissey, L.J., Raimondo, T., Clark, C. and Putnis, A. 2019. Monazite as a monitor for melt–rock interaction during cooling and exhumation. *Journal of Metamorphic Geology*, **37**, 415–438, https://doi.org/10.1111/jmg.12471

Prent, A.M., Beinlich, A., Raimondo, T., Kirkland, C.L., Evans, N.J. and Putnis, A. 2020. Apatite and monazite: an effective duo to unravel superimposed fluid-flow and deformation events in reactivated shear zones. *Lithos*, **376–377**, article 105752, https://doi.org/10.1016/j.lithos.2020.105752

Prowatke, S. and Klemme, S. 2005. Effect of melt composition on the partitioning of trace elements between titanite and silicate melt. *Geochimica et Cosmochimica Acta*, **69**, 695–709, https://doi.org/10.1016/j.gca.2004.06.037

Pupin, J.P. 1980. Zircon and granite petrology. *Contributions to Mineralogy and Petrology*, **73**, 207–220, https://doi.org/10.1007/BF00381441

Pyle, J.M. and Spear, F.S. 1999. Yttrium zoning in garnet: coupling of major and accessory phases during metamorphic reactions. *Geological Materials Research*, **1**, 1–49.

Qin, T., Wu, F., Wu, Z. and Huang, F. 2016. First-principles calculations of equilibrium fractionation of O and Si isotopes in quartz, albite, anorthite, and zircon. *Contributions to Mineralogy and Petrology*, **171**, 1–14, https://doi.org/10.1007/s00410-015-1217-5

Radulescu, I.G., Rubatto, D., Gregory, C. and Compagnoni, R. 2009. The age of HP metamorphism in the Gran Paradiso Massif, Western Alps: a petrological and geochronological study of 'silvery micaschists'. *Lithos*, **110**, 95–108, https://doi.org/10.1016/j.lithos.2008.12.008

Raimondo, T., Clark, C., Hand, M., Cliff, J. and Harris, C. 2012. High-resolution geochemical record of fluid–rock interaction in a mid-crustal shear zone: a comparative study of major element and oxygen isotope transport in garnet. *Journal of Metamorphic Geology*, **30**, 255–280, https://doi.org/10.1111/j.1525-1314.2011.00966.x

Raimondo, T., Payne, J., Wade, B., Lanari, P., Clark, C. and Hand, M. 2017. Trace element mapping by LA-ICP-MS: assessing geochemical mobility in garnet. *Contributions to Mineralogy and Petrology*, **172**, article 17, https://doi.org/10.1007/s00410-017-1339-z

Rasmussen, B. and Muhling, J.R. 2007. Monazite begets monazite: evidence for dissolution of detrital monazite and reprecipitation of syntectonic monazite during low-grade regional metamorphism. *Contributions to Mineralogy and Petrology*, **154**, 675–689, https://doi.org/10.1007/s00410-007-0216-6

Ravindran, A., Mezger, K., Balakrishnan, S., Kooijman, E., Schmitt, M. and Berndt, J. 2020. Initial $^{87}Sr/^{86}Sr$ as a sensitive tracer of Archaean crust–mantle evolution: constraints from igneous and sedimentary rocks in the western Dharwar Craton, India. *Precambrian Research*, **337**, article 105523, https://doi.org/10.1016/j.precamres.2019.105523

Reddy, S.M., Saxey, D.W., Rickard, W.D.A., Fougerouse, D., Montalvo, S.D., Verberne, R. and van Riessen, A. 2020. Atom probe tomography: development and application to the geosciences. *Geostandards and Geoanalytical Research*, **44**, 5–50, https://doi.org/10.1111/ggr.12313

Regis, D., Rubatto, D., Darling, J., Cenki-Tok, B., Zucali, M. and Engi, M. 2014. Multiple metamorphic stages within an eclogite-facies terrane (Sesia Zone, Western Alps) revealed by Th–U–Pb petrochronology. *Journal of Petrology*, **55**, 1429–1456, https://doi.org/10.1093/petrology/egu029

Regis, D., Warren, C.J., Mottram, C.M. and Roberts, N.M.W. 2016. Using monazite and zircon petrochronology to constrain the P–T–t evolution of the middle crust in the Bhutan Himalaya. *Journal of Metamorphic Geology*, **34**, 617–639, https://doi.org/10.1111/jmg.12196

Renna, M.R., Tribuzio, R. and Tiepolo, M. 2007. Origin and timing of the post-Variscan gabbro–granite complex of Porto (Western Corsica). *Contributions to Mineralogy and Petrology*, **154**, 493–517, https://doi.org/10.1007/s00410-007-0205-9

Rezvukhina, O.V., Skublov, S.G., Rezvukhin, D.I. and Korsakov, A.V. 2021. Rutile in diamondiferous metamorphic rocks: new insights from trace-element composition, mineral/fluid inclusions, and U–Pb ID-TIMS dating. *Lithos*, **394–395**, article 106172, https://doi.org/10.1016/j.lithos.2021.106172

Ribeiro, B.V., Finch, M.A. *et al*. 2022. From microanalysis to supercontinents: insights from the Rio Apa Terrane into the Mesoproterozoic SW Amazonian Craton evolution during Rodinia assembly. *Journal of Metamorphic Geology*, **40**, 631–663, https://doi.org/10.1111/jmg.12641

Romer, R.L. and Rötzler, J. 2001. P–T–t evolution of ultrahigh-temperature granulites from the Saxon Granulite Massif, Germany. Part II: geochronology. *Journal of Petrology*, **42**, 2015–2032, https://doi.org/10.1093/petrology/42.11.2015

Romer, R.L. and Rötzler, J. 2011. The role of element distribution for the isotopic dating of metamorphic minerals. *European Journal of Mineralogy*, **23**, 17–33, https://doi.org/10.1127/0935-1221/2011/0023-2081

Romer, R.L. and Siegesmund, S. 2003. Why allanite may swindle about its true age. *Contributions to Mineralogy and Petrology*, **146**, 297–307, https://doi.org/10.1007/s00410-003-0494-6

Romer, R.L. and Xiao, Y. 2005. Initial Pb–Sr (–Nd) isotopic heterogeneity in a single allanite–epidote crystal: implications of reaction history for the dating of minerals with low parent-to-daughter ratios. *Contributions to Mineralogy and Petrology*, **148**, 662–674, https://doi.org/10.1007/s00410-004-0630-y

Rubatto, D. 2002. Zircon trace element geochemistry: partitioning with garnet and the link between U–Pb ages and metamorphism. *Chemical Geology*, **184**, 123–138, https://doi.org/10.1016/S0009-2541(01)00355-2

Rubatto, D. 2017. Zircon: the metamorphic mineral. *Reviews in Mineralogy and Geochemistry*, **83**, 261–295, https://doi.org/10.2138/rmg.2017.83.9

Rubatto, D. and Angiboust, S. 2015. Oxygen isotope record of oceanic and high-pressure metasomatism: a P–T–time–fluid path for the Monviso eclogites (Italy).

Contributions to Mineralogy and Petrology, **170**, article 44, https://doi.org/10.1007/s00410-015-1198-4

Rubatto, D. and Hermann, J. 2007. Experimental zircon/melt and zircon/garnet trace element partitioning and implications for the geochronology of crustal rocks. *Chemical Geology*, **241**, 38–61, https://doi.org/10.1016/j.chemgeo.2007.01.027

Rubatto, D., Williams, I.S. and Buick, I.S. 2001. Zircon and monazite response to prograde metamorphism in the Reynolds Range, central Australia. *Contributions to Mineralogy and Petrology*, **140**, 458–468, https://doi.org/10.1007/PL00007673

Rubatto, D., Hermann, J. and Buick, I.S. 2006. Temperature and bulk composition control on the growth of monazite and zircon during low-pressure anatexis (Mount Stafford, central Australia). *Journal of Petrology*, **47**, 1973–1996, https://doi.org/10.1093/petrology/egl033

Rubatto, D., Hermann, J., Berger, A. and Engi, M. 2009. Protracted fluid-induced melting during Barrovian metamorphism in the Central Alps. *Contributions to Mineralogy and Petrology*, **158**, 703–722, https://doi.org/10.1007/s00410-009-0406-5

Rubatto, D., Regis, D., Hermann, J., Boston, K., Engi, M., Beltrando, M. and McAlpine, S.R. 2011. Yo-yo subduction recorded by accessory minerals in the Italian Western Alps. *Nature Geoscience*, **4**, 338–342, https://doi.org/10.1038/ngeo1124

Rubatto, D., Chakraborty, S. and Dasgupta, S. 2013. Timescales of crustal melting in the Higher Himalayan Crystallines (Sikkim, Eastern Himalaya) inferred from trace element-constrained monazite and zircon chronology. *Contributions to Mineralogy and Petrology*, **165**, 349–372, https://doi.org/10.1007/s00410-012-0812-y

Rubatto, D., Burger, M. *et al*. 2020. Identification of growth mechanisms in metamorphic garnet by high-resolution trace element mapping with LA-ICP-TOFMS. *Contributions to Mineralogy and Petrology*, **175**, article 61, https://doi.org/10.1007/s00410-020-01700-5

Rudnick, R.L., Barth, M., Horn, I. and McDonough, W.F. 2000. Rutile-bearing refractory eclogites: missing link between continents and depleted mantle. *Science*, **287**, 278–281, https://doi.org/10.1126/science.287.5451.278

Russell, A.K., Kitajima, K., Strickland, A., Medaris, L.G., Schulze, D.J. and Valley, J.W. 2013. Eclogite-facies fluid infiltration: constraints from $\delta^{18}O$ zoning in garnet. *Contributions to Mineralogy and Petrology*, **165**, 103–116, https://doi.org/10.1007/s00410-012-0794-9

Salama, W., Anand, R. and Roberts, M. 2018. Cassiterite and rutile as indicator minerals for exploring the VMS system. *ASEG Extended Abstracts*, **2018**, 1–4, https://doi.org/10.1071/aseg2018abt7_2d

Salminen, P.E., Hölttä, P., Lahtinen, R. and Sayab, M. 2022. Monazite record for the Paleoproterozoic Svecofennian orogeny, SE Finland: an over 150-Ma spread of monazite dates. *Lithos*, **416–417**, article 106654, https://doi.org/10.1016/j.lithos.2022.106654

Savage, P.S., Armytage, R.M., Georg, R.B. and Halliday, A.N. 2014. High temperature silicon isotope geochemistry. *Lithos*, **190**, 500–519, https://doi.org/10.1016/j.lithos.2014.01.003

Sayab, M. 2006. Decompression through clockwise P–T path: implications for early N–S shortening orogenesis in the Mesoproterozoic Mt Isa Inlier (NE Australia). *Journal of Metamorphic Geology*, **24**, 89–105, https://doi.org/10.1111/j.1525-1314.2005.00626.x

Sayab, M., Suuronen, J.-P., Hölttä, P., Aerden, D., Lahtinen, R. and Kallonen, A.P. 2015. High-resolution X-ray computed microtomography: a holistic approach to metamorphic fabric analyses. *Geology*, **43**, 55–58, https://doi.org/10.1130/G36250.1

Sayab, M., Suuronen, J.-P. *et al*. 2016. Three-dimensional textural and quantitative analyses of orogenic gold at the nanoscale. *Geology*, **44**, 739–742, https://doi.org/10.1130/G38074.1

Schaltegger, U., Brack, P. *et al*. 2009. Zircon and titanite recording 1.5 million years of magma accretion, crystallization and initial cooling in a composite pluton (southern Adamello batholith, northern Italy). *Earth and Planetary Science Letters*, **286**, 208–218, https://doi.org/10.1016/j.epsl.2009.06.028

Schannor, M., Lana, C., Nicoli, G., Cutts, K., Buick, I., Gerdes, A. and Hecht, L. 2021. Reconstructing the metamorphic evolution of the Araçuaí orogen (SE Brazil) using *in situ* U–Pb garnet dating and P–T modelling. *Journal of Metamorphic Geology*, **39**, 1145–1171, https://doi.org/10.1111/jmg.12605

Schärer, U., Lian-Sheng, Z. and Tapponnier, P. 1994. Duration of strike-slip movements in large shear zones: the Red River belt, China. *Earth and Planetary Science Letters*, **126**, 379–397, https://doi.org/10.1016/0012-821X(94)90119-8

Scherer, E.E., Cameron, K.L. and Blichert-Toft, J. 2000. Lu–Hf garnet geochronology: closure temperature relative to the Sm–Nd system and the effects of trace mineral inclusions. *Geochimica et Cosmochimica Acta*, **64**, 3413–3432, https://doi.org/10.1016/S0016-7037(00)00440-3

Scherer, E., Münker, C. and Mezger, K. 2001. Calibration of the lutetium–hafnium clock. *Science*, **293**, 683–687, https://doi.org/10.1126/science.1061372

Scherer, E.E., Whitehouse, M.J. and Munker, C. 2007. Zircon as a monitor of crustal growth. *Elements*, **3**, 19–24, https://doi.org/10.2113/gselements.3.1.19

Schiller, D. and Finger, F. 2019. Application of Ti-in-zircon thermometry to granite studies: problems and possible solutions. *Contributions to Mineralogy and Petrology*, **174**, article 51, https://doi.org/10.1007/s00410-019-1585-3

Schirra, M. and Laurent, O. 2021. Petrochronology of hydrothermal rutile in mineralized porphyry Cu systems. *Chemical Geology*, **581**, article 120407, https://doi.org/10.1016/j.chemgeo.2021.120407

Schmidt, A., Weyer, S., John, T. and Brey, G.P. 2009. HFSE systematics of rutile-bearing eclogites: new insights into subduction zone processes and implications for the Earth's HFSE budget. *Geochimica et Cosmochimica Acta*, **73**, 455–468, https://doi.org/10.1016/j.gca.2008.10.028

Schmidt, A., Pourteau, A., Candan, O. and Oberhänsli, R. 2015. Lu–Hf geochronology on cm-sized garnets using microsampling: new constraints on garnet growth rates and duration of metamorphism during continental collision (Menderes Massif, Turkey). *Earth and*

Planetary Science Letters, **432**, 24–35, https://doi.org/10.1016/j.epsl.2015.09.015

Schmitz, M.D. and Bowring, S.A. 2003. Ultrahigh-temperature metamorphism in the lower crust during Neoarchean Ventersdorp rifting and magmatism, Kaapvaal Craton, southern Africa. *GSA Bulletin*, **115**, 533–548, https://doi.org/10.1130/0016-7606(2003)115<0533:UMITLC>2.0.CO;2

Schoene, B. 2014. U–Th–Pb geochronology. *In*: Holland, H.D. and Turekian, K.K. (eds) *Treatise on Geochemistry*, 2nd edn, 341–378, https://doi.org/10.1016/B978-0-08-095975-7.00310-7

Schoene, B. and Bowring, S.A. 2007. Determining accurate temperature–time paths from U–Pb thermochronology: an example from the Kaapvaal Craton, southern Africa. *Geochimica et Cosmochimica Acta*, **71**, 165–185, https://doi.org/10.1016/j.gca.2006.08.029

Schönig, J., von Eynatten, H., Meinhold, G. and Lünsdorf, N.K. 2019. Diamond and coesite inclusions in detrital garnet of the Saxonian Erzgebirge, Germany. *Geology*, **47**, 715–718, https://doi.org/10.1130/G46253.1

Schulz, B. 2021. Monazite microstructures and their interpretation in petrochronology. *Frontiers in Earth Science*, **9**, https://doi.org/10.3389/feart.2021.668566

Schwandt, C.S., Papike, J.J. and Shearer, C.K. 1996. Trace element zoning in pelitic garnet of the Black Hills, South Dakota. *American Mineralogist*, **81**, 1195–1207, https://doi.org/10.2138/am-1996-9-1018

Scibiorski, E.A. and Cawood, P.A. 2022. Titanite as a petrogenetic indicator. *Terra Nova*, **34**, 177–183, https://doi.org/10.1111/ter.12574

Scicchitano, M.R., Spicuzza, M.J., Ellison, E.T., Tuschel, D., Templeton, A.S. and Valley, J.W. 2021. *In situ* oxygen isotope determination in serpentine minerals by SIMS: addressing matrix effects and providing new insights on serpentinisation at Hole BA1B (Samail ophiolite, Oman). *Geostandards and Geoanalytical Research*, **45**, 161–187, https://doi.org/10.1111/ggr.12359

Sciuba, M. and Beaudoin, G. 2021. Texture and trace element composition of rutile in orogenic gold deposits. *Economic Geology*, **116**, 1865–1892, https://doi.org/10.5382/econgeo.4857

Scott, D.J. and St-Onge, M.R. 1995. Constraints on Pb closure temperature in titanite based on rocks from the Ungava orogen, Canada: implications for U–Pb geochronology and P–T–t path determinations. *Geology*, **23**, 1123–1126, https://doi.org/10.1130/0091-7613(1995)023<1123:COPCTI>2.3.CO;2

Scott, K.M. and Radford, N.W. 2007. Rutile compositions at the Big Bell Au deposit as a guide for exploration. *Geochemistry: Exploration, Environment, Analysis*, **7**, 353–361, https://doi.org/10.1144/1467-7873/07-135

Seman, S., Stockli, D.F. and McLean, N.M. 2017. U–Pb geochronology of grossular-andradite garnet. *Chemical Geology*, **460**, 106–116, https://doi.org/10.1016/j.chemgeo.2017.04.020

Seydoux-Guillaume, A.-M., Paquette, J.-L., Wiedenbeck, M., Montel, J.-M. and Heinrich, W. 2002. Experimental resetting of the U–Th–Pb systems in monazite. *Chemical Geology*, **191**, 165–181, https://doi.org/10.1016/S0009-2541(02)00155-9

Seydoux-Guillaume, A.-M., Montel, J.-M. *et al*. 2012. Low-temperature alteration of monazite: fluid mediated coupled dissolution–precipitation, irradiation damage, and disturbance of the U–Pb and Th–Pb chronometers. *Chemical Geology*, **330–331**, 140–158, https://doi.org/10.1016/j.chemgeo.2012.07.031

Sha, L.-K. and Chappell, B.W. 1999. Apatite chemical composition, determined by electron microprobe and laser-ablation inductively coupled plasma mass spectrometry, as a probe into granite petrogenesis. *Geochimica et Cosmochimica Acta*, **63**, 3861–3881, https://doi.org/10.1016/S0016-7037(99)00210-0

Shrestha, S., Larson, K.P., Duesterhoeft, E., Soret, M. and Cottle, J.M. 2019. Thermodynamic modelling of phosphate minerals and its implications for the development of P–T–t histories: a case study in garnet-monazite bearing metapelites. *Lithos*, **334–335**, 141–160, https://doi.org/10.1016/j.lithos.2019.03.021

Shrestha, S., Larson, K.P., Martin, A.J., Guilmette, C., Smit, M.A. and Cottle, J.M. 2020. The Greater Himalayan thrust belt: insight into the assembly of the exhumed Himalayan metamorphic core, Modi Khola Valley, Central Nepal. *Tectonics*, **39**, article e2020TC006252, https://doi.org/10.1029/2020TC006252

Simpson, A., Gilbert, S. *et al*. 2021. *In-situ* Lu–Hf geochronology of garnet, apatite and xenotime by LA ICP MS/MS. *Chemical Geology*, **577**, article 120299, https://doi.org/10.1016/j.chemgeo.2021.120299

Simpson, A., Glorie, S., Hand, M., Spandler, C., Gilbert, S. and Cave, B. 2022. *In-situ* Lu–Hf geochronology of calcite. *GChron*, **4**, 353–372, https://doi.org/10.5194/gchron-4-353-2022

Simpson, A., Glorie, S., Hand, M., Spandler, C. and Gilbert, S. 2023. Garnet Lu-Hf speed dating: A novel method to rapidly resolve polymetamorphic histories. *Gondwana Research*, https://doi.org/10.1016/j.gr.2023.04.011

Sláma, J., Košler, J. and Pedersen, R. 2007. Behaviour of zircon in high-grade metamorphic rocks: evidence from Hf isotopes, trace elements and textural studies. *Contributions to Mineralogy and Petrology*, **154**, 335–356, https://doi.org/10.1007/s00410-007-0196-6

Sliwinski, J.T. and Stoll, H.M. 2021. Combined fluorescence imaging and LA-ICP-MS trace element mapping of stalagmites: microfabric identification and interpretation. *Chemical Geology*, **581**, article 120397, https://doi.org/10.1016/j.chemgeo.2021.120397

Smit, M.A., Scherer, E.E., Bröcker, M. and van Roermund, H.L.M. 2010. Timing of eclogite facies metamorphism in the southernmost Scandinavian Caledonides by Lu–Hf and Sm–Nd geochronology. *Contributions to Mineralogy and Petrology*, **159**, 521–539, https://doi.org/10.1007/s00410-009-0440-3

Smit, M.A., Scherer, E.E. and Mezger, K. 2013. Lu–Hf and Sm–Nd garnet geochronology: chronometric closure and implications for dating petrological processes. *Earth and Planetary Science Letters*, **381**, 222–233, https://doi.org/10.1016/J.EPSL.2013.08.046

Smith, H.A. and Barreiro, B. 1990. Monazite U–Pb dating of staurolite grade metamorphism in pelitic schists. *Contributions to Mineralogy and Petrology*, **105**, 602–615, https://doi.org/10.1007/BF00302498

Smith, H.A. and Giletti, B.J. 1997. Lead diffusion in monazite. *Geochimica et Cosmochimica Acta*, **61**, 1047–1055, https://doi.org/10.1016/S0016-7037(96)00396-1

Smith, M., Storey, C., Jeffries, T. and Ryan, C. 2009. *In situ* U–Pb and trace element analysis of accessory minerals in the Kiruna district, Norrbotten, Sweden: new constraints on the timing and origin of mineralization. *Journal of Petrology*, **50**, 2063–2094, https://doi.org/10.1093/petrology/egp069

Smithies, R.H., Lu, Y. *et al*. 2021. Oxygen isotopes trace the origins of Earth's earliest continental crust. *Nature*, **592**, 70–75, https://doi.org/10.1038/s41586-021-03337-1

Smye, A.J., Roberts, N.M., Condon, D.J., Horstwood, M.S. and Parrish, R.R. 2014. Characterising the U–Th–Pb systematics of allanite by ID and LA-ICPMS: implications for geochronology. *Geochimica et Cosmochimica Acta*, **135**, 1–28, https://doi.org/10.1016/j.gca.2014.03.021

Smye, A.J., Marsh, J., Vermeesch, P., Garber, J. and Stockli, D. 2018. Applications and limitations of U–Pb thermochronology to middle and lower crustal thermal histories. *Chemical Geology*, **494**, 1–18, https://doi.org/10.1016/j.chemgeo.2018.07.003

Smythe, D.J. and Brenan, J.M. 2016. Magmatic oxygen fugacity estimated using zircon–melt partitioning of cerium. *Earth and Planetary Science Letters*, **453**, 260–266, https://doi.org/10.1016/j.epsl.2016.08.013

Smythe, D., Schulze, D. and Brenan, J. 2008. Rutile as a kimberlite indicator mineral: minor and trace element geochemistry. *International Kimberlite Conference: Extended Abstracts*, Frankfurt, Germany, **9**. https://doi.org/10.29173/ikc3434

Söderlund, U., Patchett, P.J., Vervoort, J.D. and Isachsen, C.E. 2004. The ^{176}Lu decay constant determined by Lu–Hf and U–Pb isotope systematics of Precambrian mafic intrusions. *Earth and Planetary Science Letters*, **219**, 311–324, https://doi.org/10.1016/S0012-821X(04)00012-3

Spandler, C., Hammerli, J., Sha, P., Hilbert-Wolf, H., Hu, Y., Roberts, E. and Schmitz, M. 2016. MKED1: a new titanite standard for *in situ* analysis of Sm–Nd isotopes and U–Pb geochronology. *Chemical Geology*, **425**, 110–126, https://doi.org/10.1016/j.chemgeo.2016.01.002

Spear, F.S. 2010. Monazite–allanite phase relations in metapelites. *Chemical Geology*, **279**, 55–62, https://doi.org/10.1016/j.chemgeo.2010.10.004

Spear, F.S. 2017. Garnet growth after overstepping. *Chemical Geology*, **466**, 491–499, https://doi.org/10.1016/j.chemgeo.2017.06.038

Spear, F.S. and Parrish, R.R. 1996. Petrology and cooling rates of the Valhalla complex, British Columbia, Canada. *Journal of Petrology*, **37**, 733–765, https://doi.org/10.1093/petrology/37.4.733

Spear, F.S. and Pyle, J.M. 2002. Apatite, monazite, and xenotime in metamorphic rocks. *Reviews in Mineralogy and Geochemistry*, **48**, 293–335, https://doi.org/10.2138/rmg.2002.48.7

Spear, F.S. and Pyle, J.M. 2010. Theoretical modeling of monazite growth in a low-Ca metapelite. *Chemical Geology*, **273**, 111–119, https://doi.org/10.1016/j.chemgeo.2010.02.016

Spear, F.S. and Wolfe, O.M. 2020. Revaluation of 'equilibrium' P–T paths from zoned garnet in light of quartz inclusion in garnet (QuiG) barometry. *Lithos*, **372–373**, article 105650, https://doi.org/10.1016/j.lithos.2020.105650

Spear, F.S., Selverstone, J., Hickmott, D., Crowley, P. and Hodges, K.V. 1984. P–T paths from garnet zoning: a new technique for deciphering tectonic processes in crystalline terranes. *Geology*, **12**, 87–90, https://doi.org/10.1130/0091-7613(1984)12<87:PPFGZA>2.0.CO;2

Spencer, C.J., Kirkland, C.L. and Taylor, R.J.M. 2016. Strategies towards statistically robust interpretations of *in situ* U–Pb zircon geochronology. *Geoscience Frontiers*, **7**, 581–589, https://doi.org/10.1016/j.gsf.2015.11.006

Spencer, C.J., Kirkland, C., Roberts, N., Evans, N. and Liebmann, J. 2020. Strategies towards robust interpretations of *in situ* zircon Lu–Hf isotope analyses. *Geoscience Frontiers*, **11**, 843–853, https://doi.org/10.1016/j.gsf.2019.09.004

Spencer, K.J., Hacker, B.R. *et al*. 2013. Campaign-style titanite U–Pb dating by laser-ablation ICP: implications for crustal flow, phase transformations and titanite closure. *Chemical Geology*, **341**, 84–101, https://doi.org/10.1016/j.chemgeo.2012.11.012

Stearns, M.A., Hacker, B.R., Ratschbacher, L., Rutte, D. and Kylander-Clark, A.R.C. 2015. Titanite petrochronology of the Pamir gneiss domes: implications for middle to deep crust exhumation and titanite closure to Pb and Zr diffusion. *Tectonics*, **34**, 784–802, https://doi.org/10.1002/2014TC003774

Stepanov, A.S., Hermann, J., Rubatto, D. and Rapp, R.P. 2012. Experimental study of monazite/melt partitioning with implications for the REE, Th and U geochemistry of crustal rocks. *Chemical Geology*, **300**, 200–220, https://doi.org/10.1016/j.chemgeo.2012.01.007

Stern, R.A. and Rayner, N.M. 2003. *Ages of Several Xenotime Megacrysts by ID-TIMS. Potential Reference Materials for Ion Microprobe U–Pb Geochronology*. Geological Survey of Canada.

Štípská, P., Hacker, B.R., Racek, M., Holder, R., Kylander-Clark, A.R.C., Schulmann, K. and Hasalová, P. 2015. Monazite dating of prograde and retrograde P–T–d paths in the Barrovian terrane of the Thaya window, Bohemian Massif. *Journal of Petrology*, **56**, 1007–1035, https://doi.org/10.1093/petrology/egv026

St-Onge, M.R. 1987. Zoned poikiloblastic garnets: P–T paths and syn-metamorphic uplift through 30 km of structural depth, Wopmay Orogen, Canada. *Journal of Petrology*, **28**, 1–21, https://doi.org/10.1093/petrology/28.1.1

Storey, C.D., Jeffries, T.E. and Smith, M. 2006. Common lead-corrected laser ablation ICP-MS U–Pb systematics and geochronology of titanite. *Chemical Geology*, **227**, 37–52, https://doi.org/10.1016/j.chemgeo.2005.09.003

Strzelecki, A.C., Reece, M. *et al*. 2022. Crystal chemistry and thermodynamics of HREE (Er, Yb) mixing in a xenotime solid solution. *ACS Earth and Space Chemistry*, **6**, 1375–1389, https://doi.org/10.1021/acsearthspacechem.2c00052

Stünitz, H. and Tullis, J. 2001. Weakening and strain localization produced by syn-deformational reaction of plagioclase. *International Journal of Earth Sciences*, **90**, 136–148, https://doi.org/10.1007/s005310000148

Su, J.-H., Zhao, X.-F., Li, X.-C., Su, Z.-K., Liu, R., Qin, Z.-J. and Chen, M. 2021. Fingerprinting REE mineralization and hydrothermal remobilization history of the carbonatite-alkaline complexes, Central China: constraints from *in situ* elemental and isotopic analyses of phosphate minerals. *American Mineralogist: Journal of Earth and Planetary Materials*, **106**, 1545–1558, https://doi.org/10.2138/am-2021-7746

Sun, J.-F., Yang, J.-H., Wu, F.-Y., Li, X.-H., Yang, Y.-H., Xie, L.-W. and Wilde, S.A. 2010. Magma mixing controlling the origin of the Early Cretaceous Fangshan granitic pluton, North China Craton: *in situ* U–Pb age and Sr-, Nd-, Hf- and O-isotope evidence. *Lithos*, **120**, 421–438, https://doi.org/10.1016/j.lithos.2010.09.002

Suzuki, K. and Adachi, M. 1994. Middle Precambrian detrital monazite and zircon from the Hida gneiss on Oki-Dogo Island, Japan: their origin and implications for the correlation of basement gneiss of southwest Japan and Korea. *Tectonophysics*, **235**, 277–292, https://doi.org/10.1016/0040-1951(94)90198-8

Suzuki, K. and Kato, T. 2008. CHIME dating of monazite, xenotime, zircon and polycrase: protocol, pitfalls and chemical criterion of possibly discordant age data. *Gondwana Research*, **14**, 569–586, https://doi.org/10.1016/j.gr.2008.01.005

Suzuki, K., Adachi, M. and Kajizuka, I. 1994. Electron microprobe observations of Pb diffusion in metamorphosed detrital monazites. *Earth and Planetary Science Letters*, **128**, 391–405, https://doi.org/10.1016/0012-821X(94)90158-9

Tacchetto, T., Reddy, S.M., Saxey, D.W., Fougerouse, D., Rickard, W.D.A. and Clark, C. 2021. Disorientation control on trace element segregation in fluid-affected low-angle boundaries in olivine. *Contributions to Mineralogy and Petrology*, **176**, article 59, https://doi.org/10.1007/s00410-021-01815-3

Tacchetto, T., Clark, C., Erickson, T., Reddy, S.M., Bhowany, K. and Hand, M. 2022. Weakening the lower crust: conditions, reactions and deformation. *Lithos*, **422–423**, article 106738, https://doi.org/10.1016/j.lithos.2022.106738

Tamblyn, R., Hand, M., Simpson, A., Gilbert, S., Wade, B. and Glorie, S. 2022. *In situ* laser ablation Lu–Hf geochronology of garnet across the Western Gneiss Region: campaign-style dating of metamorphism. *Journal of the Geological Society, London*, **179**, article jgs2021-094, https://doi.org/10.1144/jgs2021-094

Taylor, R.J.M., Clark, C., Fitzsimons, I.C.W., Santosh, M., Hand, M., Evans, N. and McDonald, B. 2014. Post-peak, fluid-mediated modification of granulite facies zircon and monazite in the Trivandrum Block, southern India. *Contributions to Mineralogy and Petrology*, **168**, article 1044, https://doi.org/10.1007/s00410-014-1044-0

Taylor, R.J.M., Harley, S.L., Hinton, R.W., Elphick, S., Clark, C. and Kelly, N.M. 2015. Experimental determination of REE partition coefficients between zircon, garnet and melt: a key to understanding high-T crustal processes. *Journal of Metamorphic Geology*, **33**, 231–248, https://doi.org/10.1111/jmg.12118

Taylor, R.J.M., Kirkland, C.L. and Clark, C. 2016. Accessories after the facts: constraining the timing, duration and conditions of high-temperature metamorphic processes. *Lithos*, **264**, 239–257, https://doi.org/10.1016/j.lithos.2016.09.004

Taylor, R.J.M., Clark, C., Harley, S.L., Kylander-Clark, A.R.C., Hacker, B.R. and Kinny, P.D. 2017. Interpreting granulite facies events through rare earth element partitioning arrays. *Journal of Metamorphic Geology*, **35**, 759–775, https://doi.org/10.1111/jmg.12254

Taylor, R.J.M., Johnson, T.E., Clark, C. and Harrison, R.J. 2020. Persistence of melt-bearing Archean lower crust for >200 my – an example from the Lewisian Complex, northwest Scotland. *Geology*, **48**, 221–225, https://doi.org/10.1130/G46834.1

Taylor-Jones, K. and Powell, R. 2015. Interpreting zirconium-in-rutile thermometric results. *Journal of Metamorphic Geology*, **33**, 115–122, https://doi.org/10.1111/jmg.12109

Tedeschi, M., Rossi Vieira, P.L. *et al*. 2023. Unravelling the protracted U–Pb zircon geochronological record of high to ultrahigh temperature metamorphic rocks: implications for provenance investigations. *Geoscience Frontiers*, **14**, article 101515, https://doi.org/10.1016/j.gsf.2022.101515

Tera, F. and Wasserburg, G.J. 1972. U–Th–Pb systematics in lunar highland samples from the Luna 20 and Apollo 16 missions. *Earth and Planetary Science Letters*, **17**, 36–51, https://doi.org/10.1016/0012-821X(72)90257-9

Thomas, J.B., Bodnar, R.J., Shimizu, N. and Chesner, C.A. 2003. Melt inclusions in zircon. *Reviews in Mineralogy and Geochemistry*, **53**, 63–87, https://doi.org/10.2113/0530063

Thomas, R. and Davidson, P. 2012. Water in granite and pegmatite-forming melts. *Ore Geology Reviews*, **46**, 32–46, https://doi.org/10.1016/j.oregeorev.2012.02.006

Thompson, J.M., Goemann, K., Belousov, I., Jenkins, K., Kobussen, A., Powell, W. and Danyushevsky, L. 2021. Assessment of the mineral ilmenite for U–Pb dating by LA-ICP-MS. *Journal of Analytical Atomic Spectrometry*, **36**, 1244–1260, https://doi.org/10.1039/D1JA00069A

Thomson, S.N., Gehrels, G.E., Ruiz, J. and Buchwaldt, R. 2012. Routine low-damage apatite U–Pb dating using laser ablation–multicollector–ICPMS. *Geochemistry, Geophysics, Geosystems*, **13**, https://doi.org/10.1029/2011GC003928

Tian, S., Inglis, E.C. *et al*. 2020. The zirconium stable isotope compositions of 22 geological reference materials, 4 zircons and 3 standard solutions. *Chemical Geology*, **555**, article 119791, https://doi.org/10.1016/j.chemgeo.2020.119791

Tiepolo, M., Oberti, R. and Vannucci, R. 2002. Trace-element incorporation in titanite: constraints from experimentally determined solid/liquid partition coefficients. *Chemical Geology*, **191**, 105–119, https://doi.org/10.1016/S0009-2541(02)00151-1

Timms, N.E., Kirkland, C.L. *et al*. 2020. Shocked titanite records Chicxulub hydrothermal alteration and impact age. *Geochimica et Cosmochimica Acta*, **281**, 12–30, https://doi.org/10.1016/j.gca.2020.04.031

Tinkham, D.K. and Ghent, E.D. 2005. Estimating PT conditions of garnet growth with isochemical phase-diagram sections and the problem of effective bulk-

composition. *The Canadian Mineralogist*, **43**, 35–50, https://doi.org/10.2113/gscanmin.43.1.35

Tolometti, G.D., Erickson, T.M., Osinski, G.R., Cayron, C. and Neish, C.D. 2022. Hot rocks: constraining the thermal conditions of the Mistastin Lake impact melt deposits using zircon grain microstructures. *Earth and Planetary Science Letters*, **584**, article 117523, https://doi.org/10.1016/j.epsl.2022.117523

Tomkins, H.S., Powell, R. and Ellis, D.J. 2007. The pressure dependence of the zirconium-in-rutile thermometer. *Journal of Metamorphic Geology*, **25**, 703–713, https://doi.org/10.1111/j.1525-1314.2007.00724.x

Tompkins, H.G., Zieman, L.J., Ibanez-Mejia, M. and Tissot, F.L. 2020. Zirconium stable isotope analysis of zircon by MC-ICP-MS: methods and application to evaluating intra-crystalline zonation in a zircon megacryst. *Journal of Analytical Atomic Spectrometry*, **35**, 1167–1186, https://doi.org/10.1039/C9JA00315K

Trail, D., Watson, E.B. and Tailby, N.D. 2012. Ce and Eu anomalies in zircon as proxies for the oxidation state of magmas. *Geochimica et Cosmochimica Acta*, **97**, 70–87, https://doi.org/10.1016/j.gca.2012.08.032

Trail, D., Boehnke, P., Savage, P.S., Liu, M.-C., Miller, M.L. and Bindeman, I. 2018. Origin and significance of Si and O isotope heterogeneities in Phanerozoic, Archean, and Hadean zircon. *Proceedings of the National Academy of Sciences of the USA*, **115**, 10287–10292, https://doi.org/10.1073/pnas.1808335115

Trail, D., Savage, P.S. and Moynier, F. 2019. Experimentally determined Si isotope fractionation between zircon and quartz. *Geochimica et Cosmochimica Acta*, **260**, 257–274, https://doi.org/10.1016/j.gca.2019.06.035

Triebold, S., von Eynatten, H. and Zack, T. 2012. A recipe for the use of rutile in sedimentary provenance analysis. *Sedimentary Geology*, **282**, 268–275, https://doi.org/10.1016/j.sedgeo.2012.09.008

Tual, L., Smit, M.A., Cutts, J., Kooijman, E., Kielman-Schmitt, M., Majka, J. and Foulds, I. 2022. Rapid, paced metamorphism of blueschists (Syros, Greece) from laser-based zoned Lu–Hf garnet chronology and LA-ICPMS trace element mapping. *Chemical Geology*, **607**, article 121003, https://doi.org/10.1016/j.chemgeo.2022.121003

Ushikubo, T., Williford, K.H., Farquhar, J., Johnston, D.T., van Kranendonk, M.J. and Valley, J.W. 2014. Development of *in situ* sulfur four-isotope analysis with multiple Faraday cup detectors by SIMS and application to pyrite grains in a Paleoproterozoic glaciogenic sandstone. *Chemical Geology*, **383**, 86–99, https://doi.org/10.1016/j.chemgeo.2014.06.006

Valley, J.W. 2003. Oxygen isotopes in zircon. *Reviews in Mineralogy and Geochemistry*, **53**, 343–385, https://doi.org/10.2113/0530343

Valley, J.W., Lackey, J.S. *et al*. 2005. 4.4 billion years of crustal maturation: oxygen isotope ratios of magmatic zircon. *Contributions to Mineralogy and Petrology*, **150**, 561–580, https://doi.org/10.1007/s00410-005-0025-8

Valley, J.W., Cavosie, A.J. *et al*. 2014. Hadean age for a post-magma-ocean zircon confirmed by atom-probe tomography. *Nature Geoscience*, **7**, 219–223, https://doi.org/10.1038/ngeo2075

Vanardois, J., Roger, F. *et al*. 2022. Exhumation of deep continental crust in a transpressive regime: The example of Variscan eclogites from the Aiguilles-Rouges massif (Western Alps). *Journal of Metamorphic Geology*, **40**, 1087–1120, https://doi.org/10.1111/jmg.12659.

Vance, D. and Mahar, E. 1998. Pressure–temperature paths from P–T pseudosections and zoned garnets: potential, limitations and examples from the Zanskar Himalaya, NW India. *Contributions to Mineralogy and Petrology*, **132**, 225–245, https://doi.org/10.1007/s004100050419

Vance, D., Strachan, R.A. and Jones, K.A. 1998. Extensional v. compressional settings for metamorphism: garnet chronometry and pressure–temperature–time histories in the Moine Supergroup, northwest Scotland. *Geology*, **26**, 927–930, https://doi.org/10.1130/0091-7613(1998)026<0927:EVCSFM>2.3.CO;2

van Schijndel, V., Stevens, G., Lana, C., Zack, T. and Frei, D. 2021. De Kraalen and Witrivier greenstone belts, Kaapvaal Craton, South Africa: characterisation of the Palaeo–Mesoarchaean evolution by rutile and zircon U–Pb geochronology combined with Hf isotopes. *South African Journal of Geology*, **124**, 17–36, https://doi.org/10.25131/sajg.124.0011

Vavra, G. 1990. On the kinematics of zircon growth and its petrogenetic significance: a cathodoluminescence study. *Contributions to Mineralogy and Petrology*, **106**, 90–99, https://doi.org/10.1007/BF00306410

Vavra, G. 1993. A guide to quantitative morphology of accessory zircon. *Chemical Geology*, **110**, 15–28, https://doi.org/10.1016/0009-2541(93)90245-E

Vavra, G. and Schaltegger, U. 1999. Post-granulite facies monazite growth and rejuvenation during Permian to Lower Jurassic thermal and fluid events in the Ivrea Zone (Southern Alps). *Contributions to Mineralogy and Petrology*, **134**, 405–414, https://doi.org/10.1007/s004100050493

Vavra, G., Schmid, R. and Gebauer, D. 1999. Internal morphology, habit and U–Th–Pb microanalysis of amphibolite-to-granulite facies zircons: geochronology of the Ivrea Zone (Southern Alps). *Contributions to Mineralogy and Petrology*, **134**, 380–404, https://doi.org/10.1007/s004100050492

Verberne, R., Saxey, D.W., Reddy, S.M., Rickard, W.D.A., Fougerouse, D. and Clark, C. 2019. Analysis of natural rutile (TiO_2) by laser-assisted atom probe tomography. *Microscopy and Microanalysis*, **25**, 539–546, https://doi.org/10.1017/S1431927618015477

Verberne, R., Reddy, S.M. *et al*. 2020. The geochemical and geochronological implications of nanoscale trace-element clusters in rutile. *Geology*, **48**, 1126–1130, https://doi.org/10.1130/G48017.1

Verberne, R., Reddy, S.M. *et al*. 2022*a*. Dislocations in minerals: fast-diffusion pathways or trace-element traps? *Earth and Planetary Science Letters*, **584**, article 117517, https://doi.org/10.1016/j.epsl.2022.117517

Verberne, R., van Schrojenstein Lantman, H.W. *et al*. 2022*b*. Trace-element heterogeneity in rutile linked to dislocation structures: implications for Zr-in-rutile geothermometry. *Journal of Metamorphic Geology*, **41**, 3–24, https://doi.org/10.1111/jmg.12686

Vervoort, J. 2013. Lu–Hf dating: the Lu–Hf isotope system. *In*: Rink, W.J. and Thompson, J. (eds) *Encyclopedia of Scientific Dating Methods*. Springer, 1–20.

Vho, A., Rubatto, D., Putlitz, B. and Bouvier, A.-S. 2020. New reference materials and assessment of matrix effects for SIMS measurements of oxygen isotopes in garnet. *Geostandards and Geoanalytical Research*, **44**, 459–471, https://doi.org/10.1111/ggr.12324

Villaros, A., Stevens, G. and Buick, I.S. 2009. Tracking S-type granite from source to emplacement: clues from garnet in the Cape Granite Suite. *Lithos*, **112**, 217–235, https://doi.org/10.1016/j.lithos.2009.02.011

Villaros, A., Buick, I. and Stevens, G. 2012. Isotopic variations in S-type granites: an inheritance from a heterogeneous source? *Contributions to Mineralogy and Petrology*, **163**, 243–257, https://doi.org/10.1007/s00410-011-0673-9

Villaseca, C., Romera, C.M., De la Rosa, J. and Barbero, L. 2003. Residence and redistribution of REE, Y, Zr, Th and U during granulite-facies metamorphism: behaviour of accessory and major phases in peraluminous granulites of central Spain. *Chemical Geology*, **200**, 293–323, https://doi.org/10.1016/S0009-2541(03)00200-6

Viskupic, K. and Hodges, K.V. 2001. Monazite–xenotime thermochronometry: methodology and an example from the Nepalese Himalaya. *Contributions to Mineralogy and Petrology*, **141**, 233–247, https://doi.org/10.1007/s004100100239

Volante, S., Collins, W.J. *et al*. 2020*a*. Reassessing zircon–monazite thermometry with thermodynamic modelling: insights from the Georgetown igneous complex, NE Australia. *Contributions to Mineralogy and Petrology*, **175**, article 110, https://doi.org/10.1007/s00410-020-01752-7

Volante, S., Collins, W.J., Pourteau, A., Li, Z.X., Li, J. and Nordsvan, A.R. 2020*b*. Structural evolution of a 1.6 Ga orogeny related to the final assembly of the supercontinent Nuna: coupling of episodic and progressive deformation. *Tectonics*, **39**, article e2020TC006162, https://doi.org/10.1029/2020TC006162

Volante, S., Pourteau, A. *et al*. 2020*c*. Multiple P–T–d–t paths reveal the evolution of the final Nuna assembly in northeast Australia. *Journal of Metamorphic Geology*, **38**, 593–627, https://doi.org/10.1111/jmg.12532

Volante, S., Collins, W.J. *et al*. 2022. Spatio-temporal evolution of Mesoproterozoic magmatism in NE Australia: a hybrid tectonic model for final Nuna assembly. *Precambrian Research*, **372**, article 106602, https://doi.org/10.1016/j.precamres.2022.106602

von Blackenburg, F. 1992. Combined high-precision chronometry and geochemical tracing using accessory minerals: applied to the Central-Alpine Bergell intrusion (central Europe). *Chemical Geology*, **100**, 19–40, https://doi.org/10.1016/0009-2541(92)90100-J

Vry, J.K. and Baker, J.A. 2006. LA-MC-ICPMS Pb–Pb dating of rutile from slowly cooled granulites: confirmation of the high closure temperature for Pb diffusion in rutile. *Geochimica et Cosmochimica Acta*, **70**, 1807–1820, https://doi.org/10.1016/j.gca.2005.12.006

Vry, J., Compston, W. and Cartwright, I. 1996. SHRIMP II dating of zircons and monazites: reassessing the timing of high-grade metamorphism and fluid flow in the Reynolds Range, northern Arunta Block, Australia. *Journal of Metamorphic Geology*, **14**, 335–350, https://doi.org/10.1111/j.1525-1314.1996.00335.x

Wafforn, S., Seman, S., Kyle, J.R., Stockli, D., Leys, C., Sonbait, D. and Cloos, M. 2018. Andradite garnet U–Pb geochronology of the Big Gossan skarn, Ertsberg–Grasberg mining district, Indonesia. *Economic Geology*, **113**, 769–778, https://doi.org/10.5382/econgeo.2018.4569

Walter, B.F., Giebel, R.J., Steele-MacInnis, M., Marks, M.A., Kolb, J. and Markl, G. 2021. Fluids associated with carbonatitic magmatism: a critical review and implications for carbonatite magma ascent. *Earth-Science Reviews*, **215**, article 103509, https://doi.org/10.1016/j.earscirev.2021.103509

Walters, J.B. and Kohn, M.J. 2017. Protracted thrusting followed by late rapid cooling of the Greater Himalayan Sequence, Annapurna Himalaya, Central Nepal: insights from titanite petrochronology. *Journal of Metamorphic Geology*, **35**, 897–917, https://doi.org/10.1111/jmg.12260

Walters, J.B., Cruz-Uribe, A.M., Song, W.J., Gerbi, C. and Biela, K. 2022. Strengths and limitations of *in situ* U–Pb titanite petrochronology in polymetamorphic rocks: an example from western Maine, USA. *Journal of Metamorphic Geology*, **40**, 1043–1066, https://doi.org/10.1111/jmg.12657

Ward, C., McArthur, J. and Walsh, J. 1992. Rare earth element behaviour during evolution and alteration of the Dartmoor granite, SW England. *Journal of Petrology*, **33**, 785–815, https://doi.org/10.1093/petrology/33.4.785

Warren, C.J., Greenwood, L.V., Argles, T.W., Roberts, N.M.W., Parrish, R.R. and Harris, N.B.W. 2019. Garnet-monazite rare earth element relationships in sub-solidus metapelites: a case study from Bhutan. *Geological Society, London, Special Publications*, **478**, 145–166, https://doi.org/10.1144/SP478.1

Watson, E.B. 1979. Zircon saturation in felsic liquids: experimental results and applications to trace element geochemistry. *Contributions to Mineralogy and Petrology*, **70**, 407–419, https://doi.org/10.1007/BF00371047

Watson, E.B. 1996. Dissolution, growth and survival of zircons during crustal fusion: kinetic principals, geological models and implications for isotopic inheritance. *Earth and Environmental Science Transactions of the Royal Society of Edinburgh*, **87**, 43–56, https://doi.org/10.1017/S0263593300006465

Watson, E.B. and Harrison, T.M. 1984. Accessory minerals and the geochemical evolution of crustal magmatic systems: a summary and prospectus of experimental approaches. *Physics of the Earth and Planetary Interiors*, **35**, 19–30, https://doi.org/10.1016/0031-9201(84)90031-1

Watson, E.B. and Harrison, T.M. 2005. Zircon thermometer reveals minimum melting conditions on earliest Earth. *Science (New York, NY)*, **308**, 841–844, https://doi.org/10.1126/science.1110873

Watson, E.B., Wark, D.A. and Thomas, J.B. 2006. Crystallization thermometers for zircon and rutile. *Contributions to Mineralogy and Petrology*, **151**, 413–433, https://doi.org/10.1007/s00410-006-0068-5

Wawrzenitz, N., Krohe, A., Baziotis, I., Mposkos, E., Kylander-Clark, A.R.C. and Romer, R.L. 2015. LASS

U–Th–Pb monazite and rutile geochronology of felsic high-pressure granulites (Rhodope, N Greece): effects of fluid, deformation and metamorphic reactions in local subsystems. *Lithos*, **232**, 266–285, https://doi.org/10.1016/j.lithos.2015.06.029

Webster, J.D. and Piccoli, P.M. 2015. Magmatic apatite: a powerful, yet deceptive, mineral. *Elements*, **11**, 177–182, https://doi.org/10.2113/gselements.11.3.177

Weinberg, R.F., Wolfram, L.C., Nebel, O., Hasalová, P., Závada, P., Kylander-Clark, A.R.C. and Becchio, R. 2020. Decoupled U–Pb date and chemical zonation of monazite in migmatites: the case for disturbance of isotopic systematics by coupled dissolution–reprecipitation. *Geochimica et Cosmochimica Acta*, **269**, 398–412, https://doi.org/10.1016/j.gca.2019.10.024

Wetherill, G.W. 1956. Discordant uranium–lead ages, I. *Eos, Transactions American Geophysical Union*, **37**, 320–326, https://doi.org/10.1029/TR037i003p00320

Wetherill, G.W. 1963. Discordant uranium–lead ages: 2. Discordant ages resulting from diffusion of lead and uranium. *Journal of Geophysical Research (1896–1977)*, **68**, 2957–2965, https://doi.org/10.1029/JZ068i010p02957

White, R.W. and Powell, R. 2002. Melt loss and the preservation of granulite facies mineral assemblages. *Journal of Metamorphic Geology*, **20**, 621–632, https://doi.org/10.1046/j.1525-1314.2002.00206_20_7.x

White, R.W., Powell, R. and Johnson, T.E. 2014. The effect of Mn on mineral stability in metapelites revisited: new a–x relations for manganese-bearing minerals. *Journal of Metamorphic Geology*, **32**, 809–828, https://doi.org/10.1111/jmg.12095

Whitehouse, M.J. and Kemp, A.I.S. 2010. On the difficulty of assigning crustal residence, magmatic protolith and metamorphic ages to Lewisian granulites: constraints from combined *in situ* U–Pb and Lu–Hf isotopes. *Geological Society, London, Special Publications*, **335**, 81–101, https://doi.org/10.1144/SP335.5

Whitehouse, M.J. and Platt, J.P. 2003. Dating high-grade metamorphism – constraints from rare-earth elements in zircon and garnet. *Contributions to Mineralogy and Petrology*, **145**, 61–74, https://doi.org/10.1007/s00410-002-0432-z

Whitehouse, M.J., Kemp, A.I.S. and Petersson, A. 2022. Persistent mildly supra-chondritic initial Hf in the Lewisian Complex, NW Scotland: implications for Neoarchean crust–mantle differentiation. *Chemical Geology*, **606**, article 121001, https://doi.org/10.1016/j.chemgeo.2022.121001

Williams, I.S., Compston, W., Black, L., Ireland, T. and Foster, J. 1984. Unsupported radiogenic Pb in zircon: a cause of anomalously high Pb–Pb, U–Pb and Th–Pb ages. *Contributions to Mineralogy and Petrology*, **88**, 322–327, https://doi.org/10.1007/BF00376756

Williams, M.A., Kelsey, D.E. and Rubatto, D. 2022. Thorium zoning in monazite: a case study from the Ivrea–Verbano Zone, NW Italy. *Journal of Metamorphic Geology*, **40**, 1015–1042, https://doi.org/10.1111/jmg.12656

Williams, M.L. and Jercinovic, M.J. 2002. Microprobe monazite geochronology: putting absolute time into microstructural analysis. *Journal of Structural Geology*, **24**, 1013–1028, https://doi.org/10.1016/S0191-8141(01)00088-8

Williams, M.L., Jercinovic, M.J. and Hetherington, C.J. 2007. Microprobe monazite geochronology: understanding geologic processes by integrating composition and chronology. *Annual Review of Earth and Planetary Sciences*, **35**, 137–175, https://doi.org/10.1146/annurev.earth.35.031306.140228

Williams, M.L., Jercinovic, M., Harlov, D., Budzyń, B. and Hetherington, C. 2011. Resetting monazite ages during fluid-related alteration. *Chemical Geology*, **283**, 218–225, https://doi.org/10.1016/j.chemgeo.2011.01.019

Williams, M.L., Jercinovic, M.J., Mahan, K.H. and Dumond, G. 2017. Electron microprobe petrochronology. *Reviews in Mineralogy and Geochemistry*, **83**, 153–182, https://doi.org/10.2138/rmg.2017.83.5

Wing, B.A., Ferry, J.M. and Harrison, T.M. 2003. Prograde destruction and formation of monazite and allanite during contact and regional metamorphism of pelites: petrology and geochronology. *Contributions to Mineralogy and Petrology*, **145**, 228–250, https://doi.org/10.1007/s00410-003-0446-1

Wu, Y.-B., Zheng, Y., Zhang, S., Zhao, Z., Wu, F. and Liu, X. 2007. Zircon U–Pb ages and Hf isotope compositions of migmatite from the North Dabie terrane in China: constraints on partial melting. *Journal of Metamorphic Geology*, **25**, 991–1009, https://doi.org/10.1111/j.1525-1314.2007.00738.x

Wu, Y.-B., Gao, S., Zhang, H.-F., Yang, S.-H., Jiao, W.-F., Liu, Y.-S. and Yuan, H.-L. 2008*a*. Timing of UHP metamorphism in the Hong'an area, western Dabie Mountains, China: evidence from zircon U–Pb age, trace element and Hf isotope composition. *Contributions to Mineralogy and Petrology*, **155**, 123–133, https://doi.org/10.1007/s00410-007-0231-7

Wu, Y.-B., Zheng, Y.-F., Gao, S., Jiao, W.-F. and Liu, Y.-S. 2008*b*. Zircon U–Pb age and trace element evidence for Paleoproterozoic granulite-facies metamorphism and Archean crustal rocks in the Dabie Orogen. *Lithos*, **101**, 308–322, https://doi.org/10.1016/j.lithos.2007.07.008

Wudarska, A., Wiedenbeck, M. *et al*. 2020. SIMS- and IRMS-based study of apatite reference materials reveals new analytical challenges for oxygen isotope analysis. *22nd EGU General Assembly Conference,* 4–8 May 2020, online event, Abstracts, 18841.

Yakymchuk, C. 2017. Behaviour of apatite during partial melting of metapelites and consequences for prograde suprasolidus monazite growth. *Lithos*, **274**, 412–426.

Yakymchuk, C. and Brown, M. 2014. Behaviour of zircon and monazite during crustal melting. *Journal of the Geological Society*, **171**, 465–479.

Yakymchuk, C., Kirkland, C.L. and Clark, C. 2018. Th/U ratios in metamorphic zircon. *Journal of Metamorphic Geology*, **36**, 715–737, https://doi.org/10.1111/jmg.12307

Yang, M., Yang, Y.-H. *et al*. 2022. Natural allanite reference materials for *in situ* U–Th–Pb and Sm–Nd isotopic measurements by LA-(MC)-ICP-MS. *Geostandards and Geoanalytical Research*, **46**, 169–203, https://doi.org/10.1111/ggr.12417

Yang, Y., Sun, J., Xie, L., Fan, H. and Wu, F. 2008. *In situ* Nd isotopic measurement of natural geological

materials by LA-MC-ICPMS. *Chinese Science Bulletin*, **53**, 1062–1070, https://doi.org/10.1007/s11434-008-0166-z

Yang, Z., Wang, B., Cui, H., An, H., Pan, Y. and Zhai, J. 2015. Synthesis of crystal-controlled TiO_2 nanorods by a hydrothermal method: rutile and brookite as highly active photocatalysts. *The Journal of Physical Chemistry C*, **119**, 16905–16912, https://doi.org/10.1021/acs.jpcc.5b02485

Yurimoto, H., Duke, E., Papike, J. and Shearer, C. 1990. Are discontinuous chondrite-normalized REE patterns in pegmatitic granite systems the results of monazite fractionation? *Geochimica et Cosmochimica Acta*, **54**, 2141–2145, https://doi.org/10.1016/0016-7037(90)90277-R

Zack, T. and Kooijman, E. 2017. Petrology and geochronology of rutile. *Reviews in Mineralogy and Geochemistry*, **83**, 443–467, https://doi.org/10.2138/rmg.2017.83.14

Zack, T., Kronz, A., Foley, S.F. and Rivers, T. 2002. Trace element abundances in rutiles from eclogites and associated garnet mica schists. *Chemical Geology*, **184**, 97–122, https://doi.org/10.1016/S0009-2541(01)00357-6

Zack, T., Moraes, R. and Kronz, A. 2004*a*. Temperature dependence of Zr in rutile: empirical calibration of a rutile thermometer. *Contributions to Mineralogy and Petrology*, **148**, 471–488, https://doi.org/10.1007/s00410-004-0617-8

Zack, T., von Eynatten, H. and Kronz, A. 2004*b*. Rutile geochemistry and its potential use in quantitative provenance studies. *Sedimentary Geology*, **171**, 37–58, https://doi.org/10.1016/j.sedgeo.2004.05.009

Zack, T., Stockli, D.F., Luvizotto, G.L., Barth, M.G., Belousova, E., Wolfe, M.R. and Hinton, R.W. 2011. *In situ* U–Pb rutile dating by LA-ICP-MS: ^{208}Pb correction and prospects for geological applications. *Contributions to Mineralogy and Petrology*, **162**, 515–530, https://doi.org/10.1007/s00410-011-0609-4

Zhang, H.-X., Jiang, S.-Y., Yuan, F. and Liu, S.-Q. 2022. LA-(MC)-ICP-MS U–Th–Pb dating and Nd isotopes of allanite in NYF pegmatite from lesser Qingling orogenic belt, central China. *Ore Geology Reviews*, **145**, article 104893, https://doi.org/10.1016/j.oregeorev.2022.104893

Zhang, L., Wu, J.-L., Zhang, Y.-Q., Yang, Y.-N., He, P.-L., Xia, X.-P. and Ren, Z.-Y. 2021. Simultaneous determination of Sm–Nd isotopes, trace-element compositions and U–Pb ages of titanite using a laser-ablation split-stream technique with the addition of water vapor. *Journal of Analytical Atomic Spectrometry*, **36**, 2312–2321, https://doi.org/10.1039/D1JA00246E

Zhang, L.-S. and Schärer, U. 1996. Inherited Pb components in magmatic titanite and their consequence for the interpretation of U–Pb ages. *Earth and Planetary Science Letters*, **138**, 57–65, https://doi.org/10.1016/0012-821X(95)00237-7

Zhang, W., Wang, Z. *et al*. 2019. Determination of Zr isotopic ratios in zircons using laser-ablation multiple-collector inductively coupled-plasma mass-spectrometry. *Journal of Analytical Atomic Spectrometry*, **34**, 1800–1809, https://doi.org/10.1039/C9JA00192A

Zhong, X., Andersen, N.H., Dabrowski, M. and Jamtveit, B. 2019. Zircon and quartz inclusions in garnet used for complementary Raman thermobarometry: application to the Holsnøy eclogite, Bergen Arcs, western Norway. *Contributions to Mineralogy and Petrology*, **174**, article 50, https://doi.org/10.1007/s00410-019-1584-4

Zhong, X., Moulas, E. and Tajčmanová, L. 2020. Post-entrapment modification of residual inclusion pressure and its implications for Raman elastic thermobarometry. *Solid Earth*, **11**, 223–240, https://doi.org/10.5194/se-11-223-2020

Zhou, Y., Yao, J. *et al*. 2016. Improving the molecular ion signal intensity for *in situ* liquid SIMS analysis. *Journal of the American Society for Mass Spectrometry*, **27**, 2006–2013, https://doi.org/10.1007/s13361-016-1478-x

Zhu, X.K. and O'Nions, R.K. 1999. Monazite chemical composition: some implications for monazite geochronology. *Contributions to Mineralogy and Petrology*, **137**, 351–363, https://doi.org/10.1007/s004100050555

Zirner, A.L., Marks, M.A., Wenzel, T., Jacob, D.E. and Markl, G. 2015. Rare earth elements in apatite as a monitor of magmatic and metasomatic processes: the Ilímaussaq complex, South Greenland. *Lithos*, **228**, 12–22, https://doi.org/10.1016/j.lithos.2015.04.013

Zucali, M., Corti, L., Roda, M., Ortolano, G., Visalli, R. and Zanoni, D. 2021. Quantitative X-ray maps analysis of composition and microstructure of Permian high-temperature relicts in acidic rocks from the Sesia–Lanzo Zone eclogitic continental crust, Western Alps. *Minerals*, **11**, article 1421, https://doi.org/10.3390/min11121421